MEASUREMENT OF THE TOP QUARK MASS AT CDF II

Andrew N. Kovalev

A DISSERTATION

in

Physics and Astronomy

Presented to the Faculties of the University of Pennsylvania in Partial Fulfillment of the Requirements for the Degree of Doctor of Philosophy

2005

Hugh H. Williams

Supervisor of Dissertation

Andrea J. Liu

Graduate Group Chairperson

To my Mom

Acknowledgments

First and foremost, I would like to thank my adviser, Brig Williams, for gentle guidance, patience and wisdom. And chocolates!

I would like to thank Daniel Whiteson for being such a terrific person to work with, in all respects, Bo Jayatilaka, without whose hard work this analysis might not have happened, Monica Tecchio and David Gerdes who also played a big role in making the measurement described in this dissertation.

Joel Heinrich, for sharing his expertise in statistics and computation.

The rest of the University of Pennsylvania Experimental High Energy Physics Group for being the best group a graduate student can possibly join.

The Top and Top Mass working groups of the CDF collaboration for constructive and relatively painless review process.

Florencia Canelli, Brian Mohr, Eva Halkiadakis and Adam Gibson for fruitful discussions.

Edward McKigney, for showing me around Fermilab and teaching me how to drive.

Chicago weather, for keeping me motivated throughout the winter by not letting me get too comfortable.

Family and friends for support, encouragement, tea and cookies under THE pine tree.

Blizzard Entertainment and AMC Theaters for various distractions.

Panera Bread for providing snacks and free wireless Internet access.

And finally, my ex, Anna, for breaking up with me at the right moment and thus prompting me to make the fastest research progress so far. (I wish you the best, baby, wherever you are.)

ABSTRACT

MEASUREMENT OF THE TOP QUARK MASS AT CDF II

Andrew N. Kovalev

Hugh H. Williams

We describe a measurement of the top quark mass using events with two charged leptons collected by the CDF II Detector from $p\bar{p}$ collisions with $\sqrt{s} = 1.96$ TeV at the Fermilab Tevatron. The posterior probability distribution of the top quark pole mass is calculated using the differential cross-section for the $t\bar{t}$ production and decay expressed with respect to observed leptons and jets momenta. The presence of background events in the collected sample is modeled using calculations of the differential cross-sections for major background processes. This measurement represents the first application of this method to events with two charged leptons. In a data sample with integrated luminosity of $340pb^{-1}$, we observe 33 candidate events and measure

$$M_{top} = 165.2 \pm 6.1_{stat} \pm 3.4_{syst} \text{ GeV}/c^2$$

.

Contents

1 Introduction **1**

2 Top quark physics **4**

2.1 The place of the top quark in the Standard Model 5

2.2 Production of top quarks 6

2.3 Decay of the top quark 8

2.4 Top quark properties 11

3 Apparatus **13**

3.1 The Collider 13

3.1.1 Proton source 14

3.1.2 Anti-proton source 15

3.1.3 Tevatron 16

3.2 The CDF II Detector 17

3.2.1 Tracking 19

3.2.2 Calorimetry 23

3.2.3 Muon detection 25

3.2.4 Event reconstruction 27

4 Event Selection **34**

4.1 Trigger System 34
4.2 DIL dataset 36

5 Matrix Element and the measurement of mass 41

5.1 Construction of the posterior probability 42
5.2 Treatment of the backgrounds 44

6 Transfer functions 48

6.1 Parameterization of $f(E_{parton}, E_{jet})$ 49
6.2 Tests of $f(E_{parton}, E_{jet})$ 50

7 Signal Matrix Element 56

7.1 The Calculation 56
7.1.1 Introducing the notation 59
7.1.2 Phase space transformation and Integration 60
7.1.3 Neutrino solutions 65
7.1.4 Jacobian factor 68
7.1.5 Integral: final 71
7.1.6 Observed missing transverse energy — another constraint . . . 71
7.2 Tests of the signal differential cross-section 74
7.2.1 Parton-level tests 74
7.2.2 Smeared parton-level tests 75
7.2.3 Tests with simulated events 79

8 Backgrounds 89

8.1 Matrix Element calculation with Alpgen 90
8.2 Interface to Alpgen 91
8.3 Drell-Yan : Differential cross-section 96

8.3.1 Performance 100
8.4 Cross section for W pair production 101
8.4.1 Differential cross section and notation 101
8.4.2 Phase space transformation and integration 102
8.4.3 Neutrino solutions 103
8.4.4 Jacobian factor 104
8.4.5 Final integral 106
8.4.6 Performance 107
8.5 Modeling of backgrounds with fake leptons 109
8.5.1 Wjjj: differential cross section 109
8.5.2 Performance 111

9 Calibration of Response and Error Estimate 115
9.1 Signal only tests with P_s 116
9.2 Signal and background tests with P_s 117
9.3 Signal and background tests with P_s and P_b 117
9.4 Derivation of response correction 118
9.5 Derivation of error correction 119

10 Systematics 127
10.1 Jet response 128
10.2 Generator 129
10.3 Response calibration 129
10.4 Sample composition 130
10.5 PDF uncertainties and α_s 131
10.6 Radiation of additional gluons 133
10.7 Gluon fusion contribution to $t\bar{t}$ production 133

10.8 Background statistics 134
10.9 Background modeling 135
10.9.1 Drell-Yan 135
10.9.2 Fake background 137
10.10 Summary 138

11 Data **144**
11.1 Kinematic properties of observed events 144
11.2 Result 149

A Datasets **155**
A.1 Inclusive electron sample 155
A.2 Inclusive muon sample 156
A.3 Plug data sample 157
A.4 Dilepton categories 157

B Invariant mass **159**

C Computation **161**

D Analytic neutrino solutions **163**

E Kinematic details of data events **166**

List of Figures

2.1 Production of a single top 7

2.2 Top pair production 8

2.3 NLO and NNLO pair production cross-section 9

2.4 Top-antitop pair production and decay process 10

2.5 The mass measurement at Tevatron Run I 12

3.1 Schematic view of the Tevatron accelerator complex 14

3.2 CDF II detector 19

3.3 The CDF tracking system 20

3.4 Muon subsystem coverage 26

4.1 CDF Data Acquisition system 37

4.2 Acceptance of the DIL selection as a function of top pole mass, parametrized by $p_0 + p_1 M_t + p_2 M_t^2$. 39

6.1 Joint distribution of E_{parton} and E_{jet}. This histogram shows (in color) the density (blue – low to red – high) of simulated partons with energies E_{parton} which are matched to jets with energies E_{jet}. 51

6.2 A simple test of $f(E_{parton}, E_{jet})$: the histograms show the simulated E_{jet} and $E_{parton} - E_{jet}$ distributions from a known distribution of E_{parton}. The lines show the predicted distributions for E_{jet} and $E_{parton} - E_{jet}$ as derived from E_{parton} using $f(E_{parton}, E_{jet})$. The bottom plot shows a distribution of parton energies that the predictions are based upon. 53

6.3 A simple test of $f(E_{parton}, E_{jet})$ over smaller ranges of E_{parton}: simulated E_{jet} from a known distribution of E_{parton} over small sub-ranges of that E_{parton} distribution. The lines shows the predicted distributions for E_{jet} as derived from E_{parton} using $f(E_{parton}, E_{jet})$. 54

6.4 Tests of $f(E_{parton}, E_{jet})$ stability. The jet energy distributions shown are from detector simulation of b-quarks from MC $t\bar{t}$ decay of $M_t = 150$, 160, 170, 180, 190, and 200 GeV/c^2. The line shows the predicted jet energy distribution for each case using the parton energy distribution (not shown) and $f(E_{parton}, E_{jet})$ derived from b-quarks from MC $t\bar{t}$ decay of $M_t = 178$ GeV/c^2 55

7.1 Residual in M_W, M_t and E_ν for numerical solutions to the equations required for a change of variables. 68

7.2 $|M|^2$ as a function of pole mass for four parton-level top quark pair events with $M_t = 175$ GeV. 75

7.3 An ensemble of pseudo-experiments using perfect information for parton-level top quark pair events with $M_t = 175$ GeV. The extracted mass is the peak of the joint probability. As these shapes are not necessarily Gaussian, the positive and negative errors $\Delta M_t^{\pm}$ are defined such that $\int_{M_t - \Delta M_t^-}^{M_t + \Delta M_t^+} P(x|M_t) = 0.68$. 76

7.4 Posterior probability as a function of pole mass for four parton-level top quark pair events where the quark energies are smeared by 10% with $M_t = 175$ GeV and the four-momentum information of two neutrinos is ignored. 77

7.5 Distributions of reconstructed top-quark mass, predicted error on mass determination and pull in an ensemble of pseudo-experiments of 10 parton-level top quark pair events where the quark energies are smeared by 10% with $M_t = 175$ GeV 78

7.6 Angular matching between jets and b-quarks from top decay. The width of distribution demonstrates the angular resolution. Overflow bin at $\Delta R = 0.7$ illustrates the number of jets with no corresponding b-quark. 80

7.7 Variation of pull-width from pseudo-experiments as a function of the angular matching requirement between jets and partons. 81

7.8 Angular resolution of jets after artificial smearing of the parton-level events. 82

7.9 Left, $\Delta P_T \equiv P_T^{hepg} - P_T^{reco}$ for events with $20 < P_T < 60$ GeV. Right, ΔP_T for events with $P_T > 60$ GeV. 83

7.10 Lepton momentum are smeared by introducing a random term to the inverse P_T according to a Gaussian. Left, ΔP_T for events with $P_T < 60$ GeV. Right, ΔP_T for events with $P_T > 60$ GeV. 84

7.11 Correlation between the P_T of the $t\bar{t}$ system and the number of reconstructed jets. Top, distribution of P_T for events with varying jets. Bottom, average P_T for varying jet multiplicity. 88

8.1 Variation in $\log(|M|^2)$ with increasing number of terms in the spin and color sum. From top, moving downwards, the number of spin terms sampled increases by powers of 2 from 1 to 32. From left, moving right, the number of color terms sampled increases by powers of 2 from 1 to 32. The x axis range is from -10 to $+10$ in $\Delta \ln |M|^2$. 93

8.2 Variation of the squared matrix element for $pp \to Z(\to ll) + 2jets$ as a function of the leptonic pair invariant mass. 94

8.3 Evaluation of the squared matrix element for $pp \to Z(\to ll) + 2jets$ for parton-level $t\bar{t}$ and $Z + 2p$ events. The top plot shows a histogram of $\ln |M_{Zjj}|^2$, the bottom shows a two-dimensional histogram of $\ln |M_{Zjj}|^2$ (on x axis) versus $M_{\ell\ell}$ (on y axis). 95

8.4 Evaluation of the Zjj probability for fully reconstructed Z and $t\bar{t}$ events, after selection is applied. 99

8.5 Evaluation of the squared matrix element for $pp \to WW(\to l\nu l\nu) + 2jets$ for parton-level $t\bar{t}$ and $WW + 2p$ events. 107

8.6 Evaluation of the $WWjj$ probability for WW and $t\bar{t}$ events in fully simulated events, after the signal selection cuts have been applied. . 108

8.7 Evaluation of the squared matrix element for $pp \to W(\to l\nu) + 3jets$ for parton-level $t\bar{t}$ and $W + 3p$ events. 112

8.8 Evaluation of the $Wjjj$ probability for Gaussian smeared $Wjjj$ and $t\bar{t}$ events, neutrino information discarded. 113

8.9 Evaluation of the $Wjjj$ probability for fully simulated $t\bar{t}$ and events from the data which are candidates to produce a fake lepton. 114

9.1 Top, response for pseudo-experiments of signal events, using only P_s to extract the mass. Bottom, width of pull distributions. 121

9.2 Residual in top mass, and mean of pull distribution for varying simulated M_t, in signal-only pseudo-experiments. 122
9.3 Response curve for pseudo-experiments of signal and background events, using only P_s to extract the mass. 122
9.4 Top, response for pseudo-experiments of signal and background events, using P_s and P_b to extract the mass. Bottom, width of pull distributions. 123
9.5 RMS of mass distribution, mean estimated statistical uncertainty and fitted pull width as a function of the number of expected Z background events with (*top*) and without (*bottom*) background probability. Expected number of signal events is kept constant. The statistical uncertainty is estimated from a width of the probability distribution for a given pseudo-experiment. The mean is taken over all generated pseudo-experiments. 124
9.6 Pull widths before (*top*) and after (*bottom*) error scaling, for samples of different top mass using the DIL selection. 125
9.7 Extracted mass, error and pull for DIL selection and $M_t = 178$ GeV, all corrections applied. 126

10.1 Difference in extracted mass between the positive and negative PDF eigenvectors for a Pythia sample. 132
10.2 Variation in measured mass when background samples are split into disjoint sets. Top left, $Z \to e\bar{e}, \mu\bar{\mu}$; Top right, Fakes. Middle left, WW; Middle right, WZ. Bottom, $Z \to \tau\tau$. 140
10.3 Missing transverse energy in Z+0jet events, where the Z decays to electrons (*top*) or muons (*bottom*). 141

10.4 Missing transverse energy in Z+1jet events, where the Z decays to electrons (*top*) or muons (*bottom*). 142
10.5 Missing transverse energy in Z+2jet events, where the Z decays to electrons (*top*) or muons (*bottom*). 143

11.1 Comparison of the $t\bar{t}$ probability distribution for simulated events, scaled by expected contribution to the sample composition, to that for observed events. 145
11.2 Comparison of the Zjj probability distribution for simulated events, scaled by expected contribution to the sample composition, to that for observed events. 146
11.3 Comparison of the $WWjj$ probability distribution for simulated events, scaled by expected contribution to the sample composition, to that for observed events. 147
11.4 Comparison of the "Fakes" probability distribution for simulated events, scaled by expected contribution to the sample composition, to that for observed events. 148
11.5 Posterior probabilities for each of the 33 candidate events. Each includes the normalized signal and background probabilities. 151
11.6 Posterior probability density as a function of the top pole mass, for the 33 candidate events, with additional granularity in the evaluation of the probability. 152
11.7 Posterior probability density as a function of the top pole mass with a Gaussian fit overlaid, for the 33 candidate events, with additional granularity in the evaluation of the probability. 153

11.8 Distribution of expected errors for $M_t = 165$ GeV. The measured error is shows as the line; 17% of pseudo-experiments yield a smaller error. 154

E.1 Transverse momentum (P_T), azimuthal angle (ϕ) and pseudo-rapidity (η) of the leading jet. 168

E.2 Transverse momentum (P_T), azimuthal angle (ϕ) and pseudo-rapidity (η) of the second jet. 168

E.3 Transverse momentum (P_T), azimuthal angle (ϕ) and pseudo-rapidity (η) of the leading lepton. 168

E.4 Transverse momentum (P_T), azimuthal angle (ϕ) and pseudo-rapidity (η) of the second lepton. 169

E.5 Transverse momentum (P_T), azimuthal angle (ϕ) and pseudo-rapidity (η) of the missing transverse energy. 169

E.6 Transverse momentum (P_T), azimuthal angle (ϕ) and pseudo-rapidity (η) of the vector sum of the leptons. 169

E.7 Difference in transverse momentum (P_T), azimuthal angle (ϕ) and pseudo-rapidity (η) of the two leptons. 170

E.8 Transverse momentum (P_T), azimuthal angle (ϕ) and pseudo-rapidity (η) of the vector sum of the jets. 170

E.9 Transverse momentum (P_T), azimuthal angle (ϕ) and pseudo-rapidity (η) of the vector sum of both jets and leptons. 170

E.10 Distribution of H_T. 171

E.11 Transverse momentum (P_T), azimuthal angle (ϕ) and pseudo-rapidity (η) of the difference between the leading jets. 172

E.12 Transverse momentum (P_T), azimuthal angle (ϕ) and pseudo-rapidity (η) of the difference between the leading lepton and the leading jet. . 172

E.13 Transverse momentum (P_T), azimuthal angle (ϕ) and pseudo-rapidity (η) of the difference between the missing energy and the leading jet. . 172

List of Tables

4.1 Expected sample composition in $\int L = 340pb^{-1}$. The number of expected $t\bar{t}$ events assumes $\sigma_{t\bar{t}} = 6.7$ pb and $M_t = 175$ GeV. 40

6.1 Parameters for $f(E_{parton}, E_{jet})$ extracted using matched b-jet and quarks from HERWIG $t\bar{t}$ MC. 50

7.1 Demonstration of well-behaved pull distributions in pseudo-experiments drawn from events which obey assumptions regarding jet and lepton resolution. 77

7.2 Pull width affected by the jet angle resolution, in fully reconstructed events and in artificially smeared parton-level events. 81

7.3 Effect of muon momentum resolution on pull widths, for a variety of jet requirements. The effect of taus is also described. The "jets = 2" denotes the selection where only the events with exactly two jets are accepted. 84

7.4 Effect on the pull width of smearing lepton energies. The parameters of "less" and "more" smearing are shown in Figure 7.10 84

7.5 Increase in pull width due to jets which are unmatched to b-quarks. A $\approx 20\%$ effect is seen across lepton types. 85

7.6 Correlation between increased P_T of the $t\bar{t}$ system, the pull width from pseudo-experiments, and the fraction of events with 2 jets from b-quarks. 86

9.1 Degradation of the error as background events are added to the simulated sample, and recovery of the sensitivity as the background probability is included. These estimates are obtained for the expected sample composition given by Table 4.1 118

9.2 Effect on the fitted pull of modeled and unmodeled backgrounds. . . 119

9.3 Effect on the fitted pull variation of the signal sample 119

10.1 Summary of systematic errors 139

A.1 Additional electron cuts. 156

A.2 Additional muon identification requirements 157

A.3 The dilepton event categories 158

E.1 Run and event numbers and selected kinematic quantities for candidate dilepton events. 167

Chapter 1

Introduction

Since the early days of western civilization people invariably tried to answer the two most fundamental questions of all: "What are the things made of and why do they behave the way they do?", and "What's the purpose of it all". The second one of these questions became a foundation of various philosophical and literary endeavors. The first question is the core and essence of what our contemporaries call "Hard Science". The term is quite appropriate, both in terms of the intellectual effort involved and the amount of physical labor required to build and operate experimental equipment. Science, hard and less so, has come a long way since the early days. Scientists have acquired a lot of expertise in breaking things and have perfected the skills of rummaging through the rubble. Molecules, atoms, nuclei and now elementary particles — things well beyond the sensory abilities of a man were discovered and studied in much detail. What we now call "elementary" particles are believed to be just that — elementary in the sense of being unbreakable. That would have been the end of it all if not for a relatively novel idea that most of the smallest things are in constant transmutations and interactions with each other. Thus, the "What" part of the most fundamental question was mostly exhausted after 1995 when the last one of

the quarks, widely believed to be there even before that, was finally discovered, [1,2]. Scientific focus shifted towards "Why". Why do these elementary particles behave the way they do? To answer it we need to know as much as possible about them: how massive they are, how they interact with each other, how short-lived they are, are they charged and more.

The top quark is special, and it is not just because it is the youngest child in the family. Top is the heaviest of quarks and the heaviest observed elementary particle to date, as well as the most short-lived of all quarks. Such a short life-time is both a gift and a curse. It means that the top decays so fast that it never forms bound states, which makes it possible to study in detail different polarization effects — very hard with other quarks as they depolarize via interactions in hadrons. It also means that the top hadrons will never be observed directly.

The mass of the top quark, after it was first measured by CDF and D0 experiments at Fermilab Tevatron collider [1], [2], created a lot of excitement and curiosity. The main reason is that it happened to be so large and thus close to Electro-Weak Symmetry Breaking energy-scale that it suggested a possibility for a special role the top quark might play in how the elementary particles acquire their masses.

The Standard Model, which had been extremely successful in explaining and predicting many aspects of particle interactions, is not quite complete. Why do the 21 free parameters of the Standard Model have the values they do? There seems to be a general consensus that 21 is too many. The search for the ultimate answer produced several alternatives of various degrees of plausibility. Most of these predict other wild and exotic things, yet unobserved. Thus, in the next round of experiments the top quark becomes a known entity, a background in a series of searches for "new physics". This is just another reason for the detailed studies of the properties of the heaviest of quarks. One of the most important is, of course, the mass.

The goal of the research that forms the foundation of this dissertation was to measure the mass of the top quark in a particular decay scheme, in which both top and anti-top decays results in an electron or muon being produced, and the final state consequently contains at least two leptons. Appropriately named "dilepton channel", these events can be identified and collected into a very clean, albeit a relatively small, dataset. The following chapters document the challenges that were faced and overcome on our quest to measure the top quark mass as well as possible.

Chapter 2

Top quark physics

Even before the discovery of the top quark, most particle physicists believed in its existence. The faith was not blind, of course, and was grounded on several theoretical and experimental observations. First of all, for the Standard Model, which still is the most respected theory of particles and fields, to be renormalizable, the sum of electric charges of all left-handed fermions must sum to zero. The charge that would be missing if the top quark did not exist is exactly 2/3. Secondly, the experimental limits on flavor changing neutral current decays of the b-quark suggest that b-quark cannot be an isospin singlet and should be a member of a doublet, [3]. The last bit of evidence came from the precision measurements of the Z resonance at the e^+e^- colliders that allowed researched to once again confirm that the b-quark should have a weak isospin partner. It is possible to get an impression that particle scientists knew all there is to know about the top-quark back then. Is there anything else to learn?

2.1 The place of the top quark in the Standard Model

At the time of this writing the Standard Model is *the* theory of the particles of matter and their interactions. It has been put through scores of experimental tests and a lot of evidence has been accumulated that it provides a precise description of Nature on the microscopic scale that is accessible by modern experimental equipment.

According to the Standard Model, the matter is built of quarks and leptons. All of them are fermions and as such have spin of $\frac{1}{2}$. There are six flavors of quarks, grouped into three generations of two quarks each. Leptons are similarly divided, with each of charged leptons, e, μ or τ accompanied by a corresponding neutrino. The particles of matter interact by exchanging spin-1 gauge bosons, with strong interaction being mediated by eight types of massless gluons, weak by the massive $W^{\pm}$ and Z-bosons and electromagnetic by the massless photon.

The Standard Model is a gauge theory, at the heart of which lies $SU(3)_C \times SU(2)_L \times U(1)_Y$ gauge group. For the symmetry described by this group to be exact the fermions and weak-force bosons would have to be massless. Thus the symmetry has to be spontaneously broken. Electro-weak symmetry breaking is needed to give masses to $W^{\pm}$ and Z bosons, flavor symmetry breaking — to generate the mass hierarchy of the fermion sector. Both are achieved by the introduction of a Higgs scalar field that is both coupled to the particles of matter and has a potential term that makes spontaneous symmetry breaking possible. The Higgs boson is yet unobserved although several experimental constraints have been placed on its properties. The precise top quark mass measurement when combined with W-boson mass measurement and calculations of radiative corrections to W mass from virtual t-quark and Higgs loops enables researchers to set indirect limits on Higgs mass.

Although the Standard Model has proven to be a powerful and consistent theory it has several deficiencies that stimulate the imagination of the physics community and taunt with possibilities of various "new physics". Quite a few observable quantities are simply postulated by the SM rather than derived from more general principles. Various extensions to the Standard Model, including supersymmetry (MSSM and friends) strive to provide us with a better answer. The top quark plays a prominent role in many of the "beyond Standard Model" theories. Many of these rely on the large mass of the top quark and hint at the possibilities of major discoveries at the next generation of particle experiments.

For a more detailed theoretical overview of the Standard Model refer to [4]. Excellent reviews of the Standard Model top quark can be found in [5], [6], [3] and [7]. Several top quark properties outside of the scope of SM are well-presented in [8] and [9].

2.2 Production of top quarks

The top quark at present can only be produced at colliding beam facilities, where center-of-mass frame of reference is the laboratory frame as well. Single top quarks can only be produced in charge-current weak interactions. The amplitudes are dependent on the CKM matrix elements $V_{tq} \quad (q = d, s, b)$. Top quarks are also produced in pairs via the strong interactions $q\bar{q} \rightarrow t\bar{t}$, $gg \rightarrow t\bar{t}$. Not surprisingly, the single top production cross-section is smaller than the cross-section for pair-production. In addition, the experimental signatures of the single top are harder to identify and separate from similar background signatures. The Feynman diagrams for the single top production are shown in Figure 2.1. At the time of this writing the single top production is yet to be observed. Consequently, most of the studies of top quark properties

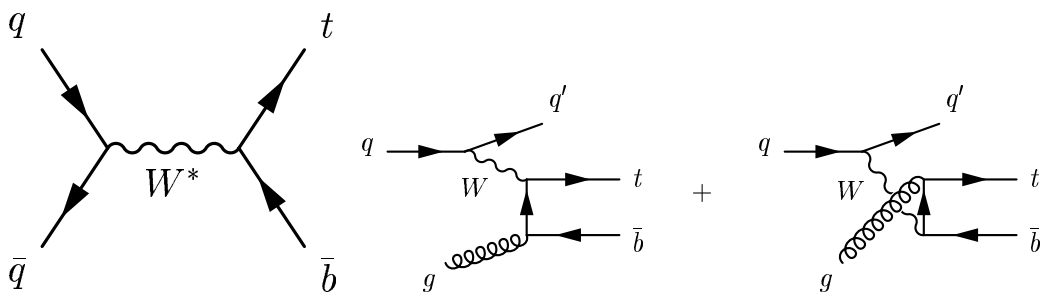

Figure 2.1: Production of a single top

are based on the events where a pair of top and anti-top quarks are produced.

Top quark pairs are can be created either via quark anti-quark annihilation or via gluon fusion, Figure 2.2. At 1.96 TeV, gluon fusion is responsible for about 15% of the $t\bar{t}$ pairs being produced.

The theoretical calculation of the Leading Order(LO) top quark pair production cross-section $\sigma_{t\bar{t}}^{LO}$ has a fairly large uncertainty, around 50% — mainly due to different possible scale choices[1]. The Next-to-Leading Order(NLO) calculation increases the cross-section by about 30% and reduces the uncertainty to approximately 12%. The pair production cross section is a function of the assumed top-quark mass and the dependence can be seen in Figure 2.3 which shows NLO cross section calculation as well as several NNLO refinements at $\sqrt{s} = 1.96$ TeV. The current theoretical prediction for assumed mass of $m_t = 175$ GeV is

$$\sigma_{t\bar{t}}^{\mathrm{NNLO-NNNLL}}(\sqrt{s} = 1.96\mathrm{TeV}, m_t = 175\mathrm{GeV}) = 6.77 \pm 0.42\mathrm{pb} \tag{2.1}$$

[1]The calculation of the total production cross-section involves factorization into perturbative series and non-perturbative part. The factorization parameter μ is normally taken to be the same as the renormalization scale μ of the perturbative expansion. Were the series expanded to all orders, none of the observables would depend on μ. The presence of such dependence stems from truncation of the series at some finite number of terms. For $t\bar{t}$ cross-section the scale is typically set to $\mu \approx M_t$. The aforementioned uncertainty is due to arbitrariness of this choice and is typically estimated by varying the scale inside the range $M_t/2 < \mu < 2M_t$, [3].

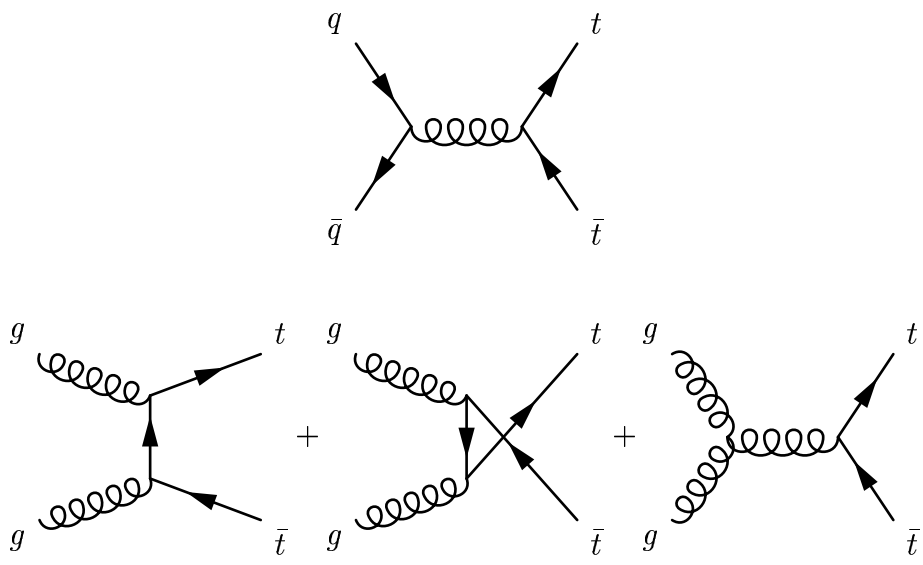

Figure 2.2: Top pair production

as presented in [10].

2.3 Decay of the top quark

The Standard Model top quark decays into a b-quark and a W-boson most of the time, the predicted branching ratio $\mathcal{B}(t \to bW) > 0.998$. Charge-current decays into $t \to Ws$ and $t \to Wd$ are also allowed but are strongly suppressed by the Cabibbo-Kobayashi-Maskawa mixing elements with factors of $10^{-3} - 10^{-4}$. These two decays as well as $t \to WbZ$ are the only Standard Model decays allowed at tree level, not counting the radiative decays such as $t \to Wbg$ and $t \to Wb\gamma$.

The flavor-changing neutral current (FCNC) decays which are also allowed (but not at tree level) include such processes as $t \to cg$, $t \to c\gamma$, $t \to cZ$. The branching ratios are of the order of 10^{-13} which is well below the detection limit of even next generation particle experiments.

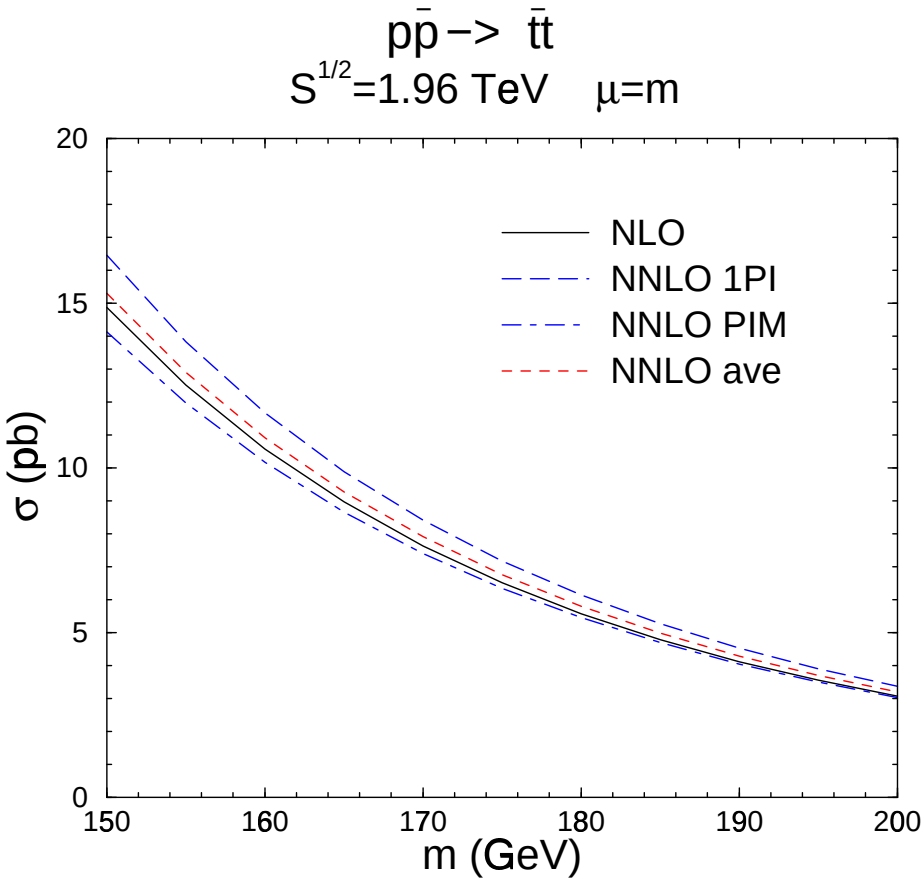

Figure 2.3: NLO and NNLO pair production cross-section

At Tevatron energies both top and anti-top are produced essentially at rest. As was already mentioned before, the lifetime of the top-quark is so short ($\Gamma \approx 1.5$GeV, which leads to $\tau \approx 5 \times 10^{-25}$ s) that it decays before it is able to form bound states, or hadronize. Such a short lifetime is in part due to the CKM-allowed decay into the b-quark.

The W-bosons that come from the predominant $t \to bW$ top quark decay, in turn decay very quickly, on the timescale of 10^{-25} into either a quark-antiquark pair or a lepton-neutrino pair. The branching ratios for these decays are essentially equal, with a caveat that all the quark flavors come in three different colors. Consequently, the

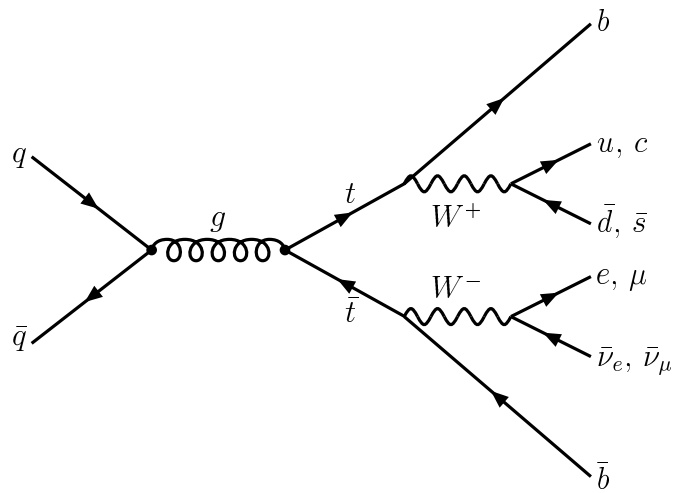

Figure 2.4: Top-antitop pair production and decay process

probability for a W to decay into each type of leptons is 1/9, while the probability to decay into either $u\bar{d}$ or $c\bar{s}$ is 2/3. In $t\bar{t}$ production events, both W-bosons decay independent of each other. The fraction of events when both W-bosons decay into electrons, (ee) events, is 1/81, the same is true for $(\mu\mu)$, the fraction of $(e\mu)$ events is 2/81, Figure 2.4.

Events where both W-s decay leptonically are called *dilepton* events. Taus are not included in this analysis. The reason for this is that tau-leptons decay leptonically 36% of times, and 64% hadronically. The secondary electrons and muons from taus are not easily identified as such, due to softer lepton energies and two additional neutrinos. Overall, dilepton event comprise about $4/81 \approx 4.9\%$ of $t\bar{t}$ decays.

Events where one of the W-s decay leptonically and the other one hadronically are known as *lepton+jets* events. Around 30% of the $t\bar{t}$ events are expected to be of this type. And finally, both W-bosons decay hadronically in about 44% of the cases. This decay channel is normally called *all-hadronic*.

The b-quarks that are produced in the top decays hadronize and result in a *jet*[2].

[2]a jet is a collection of energetic colorless particles with spatially collimated momenta. Normally,

The type of events dealt with in the present analysis is characterized by two leptons, e or μ, two energetic jets and some imbalance in transverse momentum, called *missing transverse energy* that is due to the presence of two neutrinos from leptonic W decays.

2.4 Top quark properties

The Standard Model top quark is a fermion with spin of $S = \frac{1}{2}$, weak isospin $T_3 = \frac{1}{2}$, electric charge $Q = \frac{2}{3}$. All these important properties, together with lifetime, CKM mixing $|V_{tb}|$, gauge couplings, Yukawa coupling Y_t and top quark mass are the objectives of various direct and indirect measurements. The top quark mass is one of the key properties that is possible to measure directly. In fact there is a whole family of analyses that strive to measure it in all $t\bar{t}$ decay channels to the best possible precision.

The top quark mass was directly measured at Tevatron Run I, right after top quark discovery in 1995, using the multitude of methods in all three $t\bar{t}$ decay channels, see [11–15]. The summary of these results is shown in Figure 2.5. At present, the research effort directed at the measurement of the mass includes both applications of the methods used previously, which should benefit from the increased Run II luminosity and upgrades performed on the detectors, and new sophisticated analysis techniques, developed based on the expertise that was acquired between now and then. Chapter 5 will introduce the analysis method used in this study. Inspired by a method used by D0 collaboration in Run I [16], it aims at making the best possible measurement of the mass by utilizing all the information content of the data events and by employing a theoretical description of the underlying physics via computation of a tree-level matrix element for top-antitop pair production and decay.

fragmentation of a parton results is a cascade of hadrons that propagate in a narrow cone along the original parton's direction. Thus, a well-reconstructed jet ideally corresponds to a single parton.

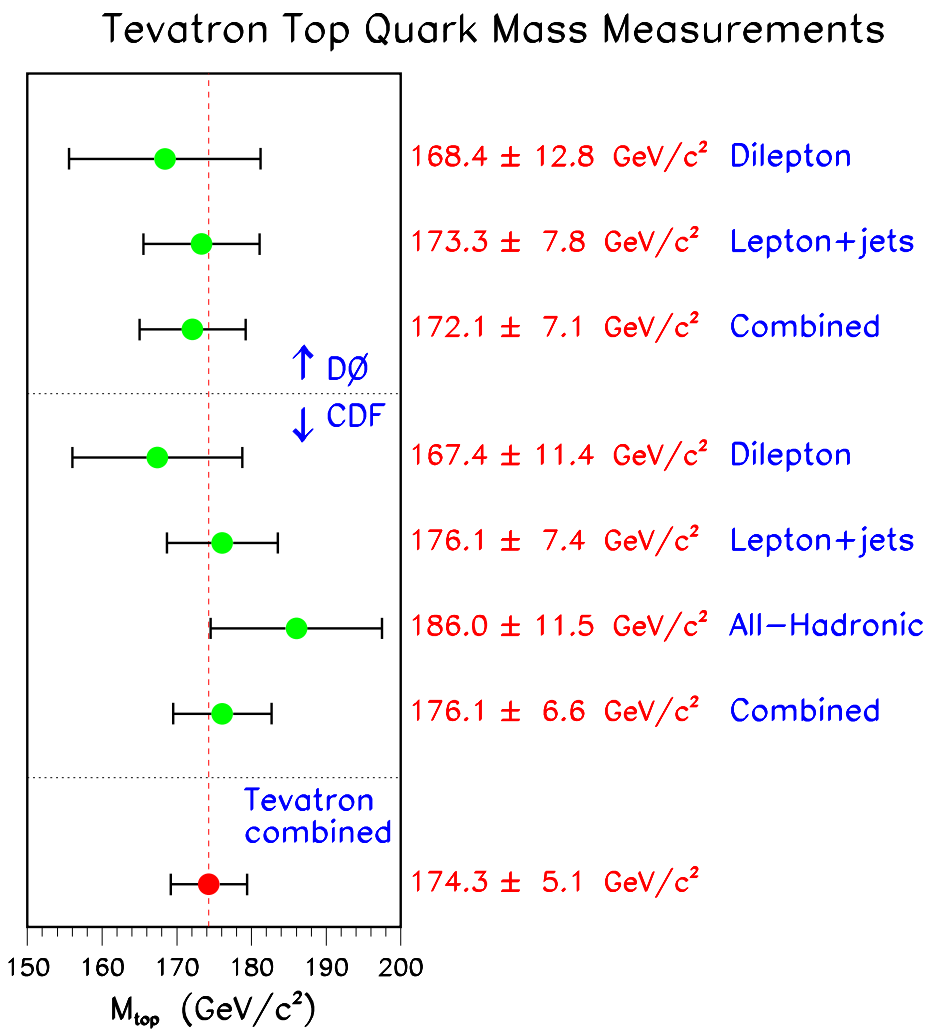

Figure 2.5: The mass measurement at Tevatron Run I

Chapter 3

Apparatus

After the discovery of the top-quark, Fermilab remains a host to the only accelerator facility in the world able to produce pairs of top and anti-top quarks *en masse* and to the detector facilities able to record enough event information for the in-depth study of the top quark properties. The upgraded Tevatron accelerator produces beams of protons and anti-protons with energies as high as 980 GeV, thus bringing the center-of-mass energy of the $p\bar{p}$ collisions to $\sqrt{s} = 1.96$ TeV. The final state particles used in this measurement were observed by the CDF II detector and the information recorded by its subsystems was used in reconstruction of interactions, identification of the events in which pairs of top and anti-top quarks were produced and ultimately enabled researchers to measure the quantities of interest. In this chapter both the Collider and the Detector equipment are described.

3.1 The Collider

The Accelerator complex at Fermilab consists of several key components, that can be conceptually separated into a series of accelerators that prepare the protons, produce

and store anti-protons and finally accelerate both protons and antiprotons to center of mass energy of 1.96 TeV and orchestrate the collisions. The schematic view of the accelerator chain is shown in Figure 3.1.

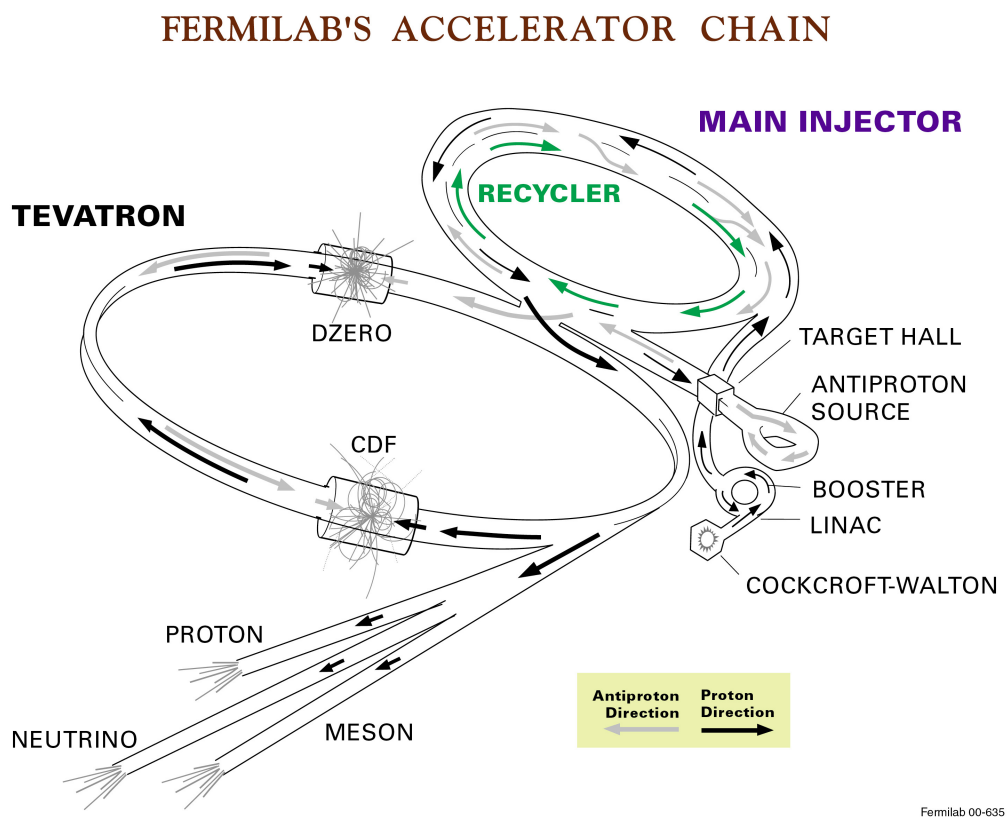

Figure 3.1: Schematic view of the Tevatron accelerator complex

3.1.1 Proton source

The Pre-accelerator is a linear accelerator that produces negative hydrogen ions and accelerates them to 750 keV simply by applying the electric field to the ionized hydrogen. The output frequency is 15 Hz and the resulting H^- ions then enter into the Linac or Linear Accelerator.

The Linac is the next step in the acceleration process. It takes negatively charged hydrogen ions from 750 keV to 400 MeV. The Linac also operates with 15 Hz fre-

quency. The modes of operation include feeding the beam to the Booster, feeding the beam to the Nuclear Therapy Facility or simply dumping the beam into a concrete block.

The Booster is the first circular accelerator in the proton accelerator chain. It has a radius of 75 meters and consists of alternating magnets and RF cavities. The Booster strips electrons of the H^- ions and accelerates the protons from 400 MeV to 8 GeV. The RF cavities apply the accelerating field while the magnets apply the bending field to keep protons in the circular orbit and ramp it up in accordance with the instantaneous energy of the beam.

The Main Injector is a circular accelerator that serves several purposes. For one, it accelerates the protons that transported from the Booster from 8 GeV to 150 GeV. In another mode of operation the Main Injector stacks the antiprotons and accelerates them to 120 GeV. The circumference of this machine is seven times that of the Booster and it is able to accelerate beam every 2.2 sec.

3.1.2 Anti-proton source

The production of the antiprotons is a technologically challenging task and thus the antiprotons production and storage capacity is the main limiting factor for the colliding beams luminosity.

The antiprotons are produced at the Target station when the 120 GeV proton beam coming from the Main Injector hits a nickel target. In this process many types of particles are being produced. A system of magnets is then used to separate 8 GeV antiprotons and direct them to the next stage accelerator.

The purpose of the Debuncher, a triangular synchrotron[1] machine where antipro-

[1] a circular accelerator in which both magnetic field and accelerating electric field are changed synchronously as the particles are accelerated, in order to maintain the same particle orbit

tons are directed after being produced, is not to accelerate them but rather to make the momentum of the particles inside the beam more uniform — this process is normally referred to as "cooling"[2]. The mean radius of the Debuncher is 90 meters. The resulting 8 GeV beam of antiprotons is then delivered into the Accumulator.

The Accumulator is located in the same tunnel as the Debuncher and is also a triangular synchrotron. It is used for storage and further cooling of the antiprotons.

The Recycler is a relatively recent addition to the Fermilab accelerator chain. It resides in the same tunnel as the Main Injector and is used to decelerate and cool down the antiprotons left in the Tevatron after the store. Several different cooling techniques are used in the Recycler which serves an important purpose of improving the antiproton utilization efficiency.

3.1.3 Tevatron

With the diameter of exactly 2 km the Tevatron is the largest of Fermilab accelerators, and the only one that uses superconductive niobium/titanium alloy magnets which are able to create 4.2 T fields. The Tevatron is mainly a storage ring. In the so called 36×36 operation mode there are 36 bunches of protons and 36 of antiprotons circling the ring in the opposite directions. The bunches of protons and antiprotons are passing through each other, "bunch-crossing", every 396 ns.

The beams of protons and antiprotons undergo focusing via quadrupole magnets in the B0 and D0 interaction points, around which the CDF and D0 detectors are built. This is done in order to reduce the beam spot size and thus increase the instantaneous luminosity and the chance of a proton collision with antiproton. The

[2]another way of looking at it is to consider cooling as a process of increasing particle density in momentum phase-space

instantaneous luminosity is given by:

$$\mathcal{L} = \frac{N_B N_p N_{\bar{p}} f}{2\pi\sigma_p^2\sigma_{\bar{p}}^2} \tag{3.1}$$

where the N_B is the number of bunches in the machine, $N_{p,\bar{p}}$ — the number of protons/antiprotons in a bunch, f is the bunch revolution frequency and $\sigma_{p,\bar{p}}^2$ is the effective width of the proton/antiproton beams.

The integrated luminosity $\int \mathcal{L}dt$ is a measure of the total number of collisions throughout a certain period of data-taking. This analysis is based on events observed in $\int \mathcal{L}dt = 340\text{pb}^{-1}$ [3] , which is about three times the amount of data acquired during the Run I.

3.2 The CDF II Detector

The Collider Detector at Fermilab, known as CDF, is a multipurpose particle detector built around the Tevatron B0 interaction point. It is approximately 15 meters long and 10 meters high and maintains approximate axial and forward-backward symmetries. The associated Cartesian coordinate system is defined as a right-handed basis with the z-axis set by the colliding beams and the protons moving in the positive z-direction. The x axis points radially outwards and y axis vertically upwards.

Although occasionally it is convenient to work in cylindrical (r, z, ϕ) or polar (r, θ, ϕ) coordinates, where the azimuthal angle ϕ is the (xy) plane angle measured from the direction of x axis, another coordinate system is commonly used in collider

[3] 1 barn = 10^{-28}m^2 is a unit measure of interaction cross-section; the instantaneous luminosity is usually measured in units of $\text{cm}^{-2}\text{s}^{-1}$, while the time-integrated luminosity in units of inverse cross-section: pb^{-1}or fb^{-1}.

physics. In this system the polar angle θ is replaced by pseudo-rapidity:

$$\eta = -\ln\tan\frac{\theta}{2} \tag{3.2}$$

The utility of the (r, η, ϕ) coordinate system stems from the axial symmetry of the experiment and from the nature of proton-antiproton collisions. The latter manifests itself in the fact that the interactions of colliding partons often result in considerable longitudinal momentum of the collision products. The rapidity of the system:

$$\zeta \equiv \frac{1}{2}\ln\frac{E+p_z}{E-p_z} \tag{3.3}$$

transforms under boosts along the z-axis as $\zeta' = \zeta + \tanh^{-1}\beta$ and thus $\Delta\zeta$ are invariant under such transformations. The pseudo-rapidity is the ultra relativistic or massless approximation to the real rapidity of the system:

$$\eta \equiv \frac{1}{2}\ln\frac{p+p_z}{p-p_z} = -\ln\tan\frac{\theta}{2} \tag{3.4}$$

Many detector components are segmented uniformly in η and ϕ. Typically the pseudo-rapidity η refers to "detector" η determined with respect to center of the detector coordinate system. The η can also be determined with respect to the point where the interaction took place — in that case it is called "event" η.

After each collision the particles that were produced in the interaction traverse through various detector subsystems. The first one they encounter is the tracking system, then calorimetry and finally the muon subdetectors. These are the basic components that provide the data that serves as the foundation of our measurement. Various other components exist which are essential to some physics analyses, for instance Cherenkov Luminosity Counters and the Time-of-Flight detector. They

were not used for this particular analysis and are described elsewhere. The schematic overview of the CDF detector is shown in Figure 3.2.

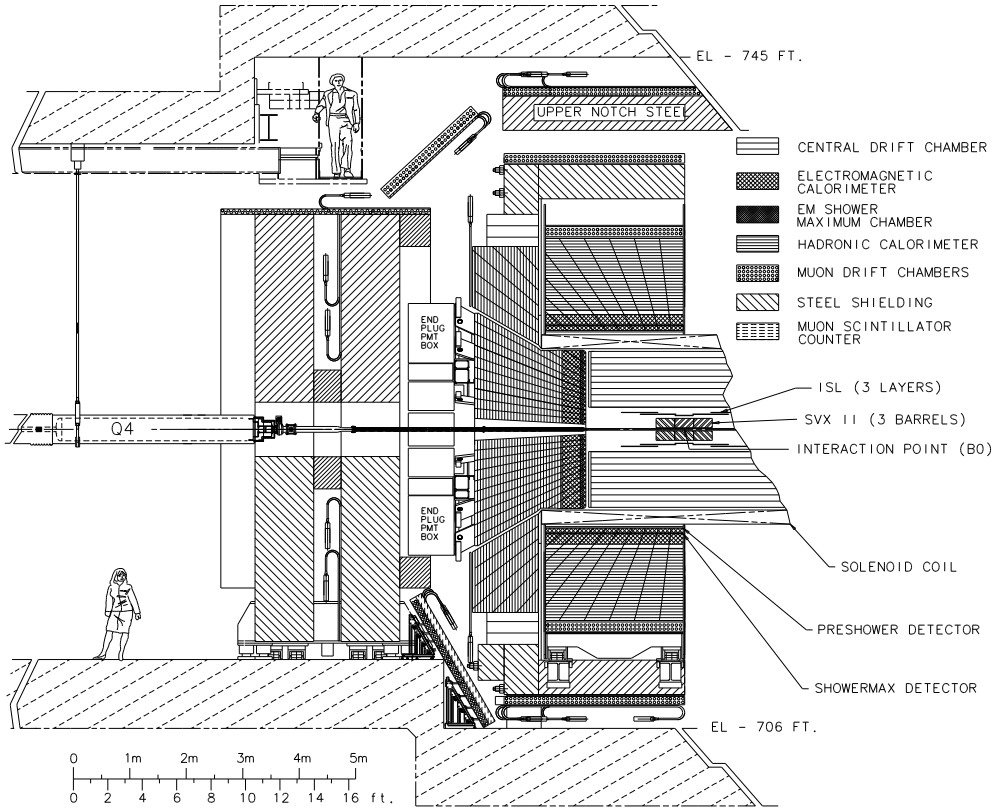

Figure 3.2: CDF II detector

3.2.1 Tracking

The CDF tracking system consists of the Central Outer Tracker (COT) and silicon detector subsystem that in turn consists of Silicon VerteX detector (SVX), Intermediate Silicon Layers (ISL) and Layer 00 (L00).

The entire tracking volume resides inside a superconducting solenoid magnet with the radius of 1.5 meters and the length of 4.8 meters. It creates uniform magnetic field of 1.4 T along the direction of the z-axis. The trajectory of a charged particle in

magnetic field is a helix. From the parameters of this helix the particle momentum can be determined, as the magnitude of the magnetic field is known.

The schematic view of the CDF tracking system in the $(r - z)$ plane is shown in Figure 3.3. The region of the detector with $|\eta| \leq 1.0$ is referred to as "central".

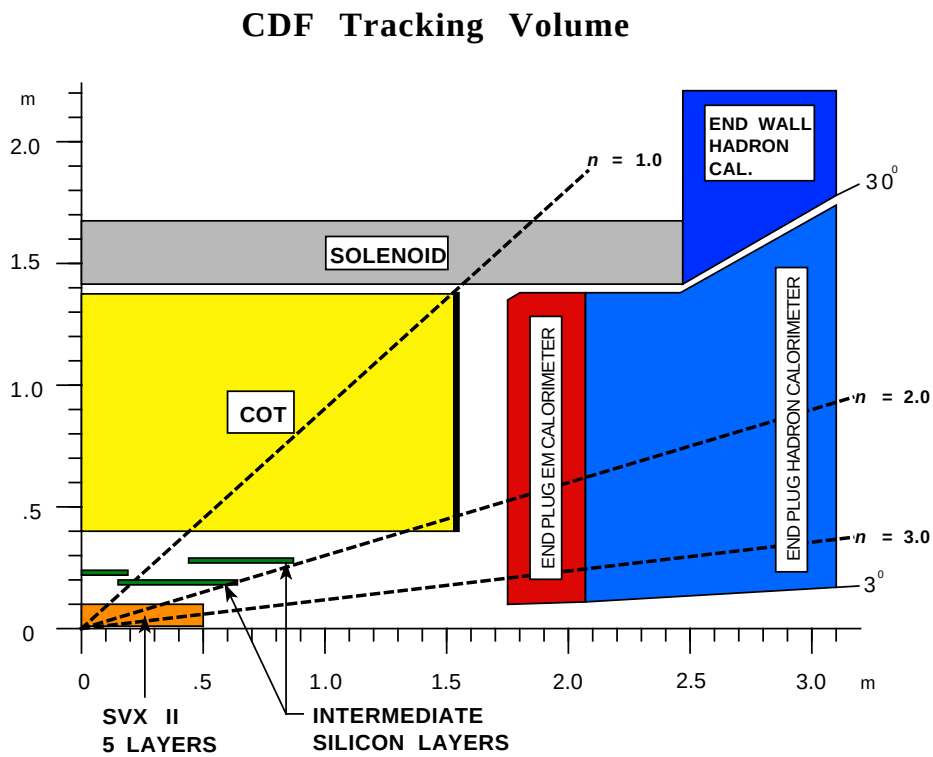

Figure 3.3: The CDF tracking system

As can be seen from the above schematic a charged particle that is produced in this rapidity interval has to travel through the entire COT tracking volume and thus has a better transverse momentum measurement than a particle with $|\eta| > 1.0$. The region $1.0 < |\eta| \leq 3.6$ is called "plug" or "forward".

The first subdetector that a particle created in a collision traverses is the Silicon detector. The main part, SVX, consists of three cylindrical barrels placed end-to-end in Z; each is 29 cm long with five layers of double sided micro-strip silicon wafers.

It occupies the space between 2.5 and 10.7 cm. The technology used allows the measurement of the ionization induced by a charged particle traversing the silicon wafer, the "hit" position, to be measured with the precision of 12μm. The double-sided silicon microstrips that are used in SVX are arranged so that one side of a chip has axial[4] strips, while the other side hosts either 90° stereo[5] strips or small angle 1.2° stereo[6] strips. Such an arrangement makes is possible to combine the $(r - \phi)$ and $(r - z)$ measurements into a three-dimensional position measurement.

Both the ISL and L00 are the extensions to the silicon tracking subsystem. The L00 consists of two sets of single-sided radiation-hard silicon microstrips mounted directly onto the beampipe at radii of 1.35 and 1.62 cm. It provides the position measurement closest to the interaction point. The ISL consists of several layers of double-sided silicon placed at the radii of 22, 20 and 28 cm. It is aimed at extending the tracking coverage to the region of $1.0 \leq |\eta| \leq 2.0$ as well as to provide help with resolving any ambiguities in matching COT tracks with SVX tracks in a dense-track environment.

The individual "hits" both from the COT and the silicon detectors are linked together with pattern-recognition software into a "track", the entity that describes the trajectory of a charged particle. The measure of the performance of the tracking system can be illustrated by the ability to determine the parameters of the helix trajectory. The resolution in the impact parameter that is achieved by the tracking system is about 40μm, and the z_0 resolution is about 70μm, where z_0 is the z coordinate of the closest approach to the z-axis.

The Silicon detector subsystem has $722,432$ readout channels. The hit data is collected, assembled and packed for transmission by radiation hard integrated circuits.

[4]strips aligned along the z axis, providing finest granularity in $(r - \phi)$
[5]thus perpendicular to z
[6]set at a small angle to z direction

The data is transported via an optical fiber link to the external data-processing units.

Precise position measurements so close to the interaction point that are possible with the Silicon Vertex detector are used to extrapolate the tracks all the way to the collision region. It is crucial for the determination of the vertex position and provides a measurement that can distinguish a particle which is coming from a primary interaction from a particle which was produced at a secondary, displaced vertex and thus is a decay product of another long lived particle.

After a charged particle exits the Silicon detector it passes through the Central Outer Tracker. The COT occupies the region with $|z| < 155$ cm and $44 < r < 132$ cm. It is a cylindrical multi-wire open-cell drift chamber filled with Argon-Ethane gas mixture, which was chosen as it provides fast drift velocity. This design constraint, in turn, stems from the need to avoid event pileup; consequently the maximum drift time is required to be less than 396 ns. The gas mixture used has the maximum drift time of about 50 ns in the drift field of roughly 2 kV/cm.

The COT consists of $30,240$ sense wires grouped into eight superlayers. The superlayers alternate between axial and stereo, with the latter having the wires strung at $\pm 2^\circ$ with respect to the axial direction. Each charged particle that escapes the COT traverses 96 layers of sense wires that ideally can provide the same number of position measurements. The single hit resolution of the COT is about 140μm. The track reconstruction software converts the individual hits into the fitted particle trajectories, the helix parameters of which allow the measurements of charged particle momenta. It results in the transverse momentum resolution of $\frac{\delta p_T}{p_T} \approx 0.15\% p_T(\mathrm{GeV}/c)^{-1}$.

Whenever possible the hit information from both the COT and the Silicon detector are combined to produce the best track fit possible. For the particles with very high momenta the parameters of a track are harder to determine precisely as the curvature of the helix is quite small. Fortunately for some of the particles, in

particular, electrons, an additional measurement of their energies is possible via the Calorimetry subsystem.

3.2.2 Calorimetry

Charged particles with energies greater that 350 MeV may leave the tracking volume and propagate beyond the solenoid magnet that surrounds it. Neutral particles, both photons and neutral hadrons, leave the tracking volume undetected. Even if they were seen by the tracking system no information about their momenta would be available for a quite obvious reason — their trajectories do not bend in magnetic field. In many of cases the measurement of their momenta is essential for the understanding of observed events. The calorimetry subsystem serves the purpose of filling this gap and is based on the fact that as particles that have reasonably high electromagnetic or hadronic interaction cross-sections propagate through matter they transfer their energy to the medium until eventually all of it is absorbed. Some media produce measurable response to such energy depositions by emitting light in amounts dependent on the amount of energy lost by the particles.

The CDF calorimetry system consist of alternating layers of scintillator and absorber material. As particles interact with absorber they produce cascades of particles or "showers" that penetrate the scintillator. The light from the latter is guided into the photomultipliers. Their response is in turn digitized and with the help of relevant calibrations converted into the measurement of the deposited energy.

All the calorimeters are divided into segments or "towers" in such a way that the division boundaries between them point at the interaction point. The entire calorimetry system consists of two regions, central and forward; the later is also known as the "plug".

The central calorimeters cover the region of 2π in ϕ and as far as $|\eta| < 1.0$

in pseudorapidity. They are segmented into the "towers" of $0.11 \times 15°$ in $\eta \times \phi$. The electromagnetic (CEM) part consists of alternating layers of lead absorber and polystyrene scintillator, while the hadronic part (CHA) uses thicker steel plates as the absorber. The CEM is $18X_0$ radiation lengths thick, while the CHA is around $4.5\lambda_0$ attenuation lengths thick. The energy resolution of the CEM is estimated to be:

$$\frac{\sigma_E}{E} = \frac{13.5\%}{\sqrt{E_T}} \oplus 2\% \tag{3.5}$$

The $\oplus$ notation means that the constant part is added in quadrature. The CHA resolution is estimated to be:

$$\frac{\sigma_E}{E} = \frac{50\%}{\sqrt{E_T}} \oplus 3\% \tag{3.6}$$

The shower-maximum (CES) and pre-shower (CPR) detectors are also considered a part of the calorimetry system. The CES is a gas multiwire proportional chamber with cathode strips that provide measurements of the z position and anode wires that allow a measurement of the ϕ of the energy deposition. The chamber is embedded into the CEM at about $5.9X_0$ where the maximum of electromagnetic energy deposition occurs. The position resolution in both directions is around 2 mm. The CPR consists of proportional chambers placed between the solenoid and the calorimeter. These two subsystems, CES and CPR, provide both position measurement that helps in matching energy depositions to tracks and in shower profile measurements — information used in particle identification to distinguish between $e^{\pm}/\gamma$ and γ/π_0.

The plug calorimeters cover the pseudorapidity range of $1.1 < |\eta| < 3.4$; the general segmentation pattern is observed. The electromagnetic section (PEM) uses calcium-tin-lead alloy as an absorber and is $21X_0$ radiation lengths thick. The hadronic part (PHA) uses iron and is about $7\lambda_0$ attenuation lengths thick. The

energy resolution of the PEM is estimated to be:

$$\frac{\sigma_E}{E} = \frac{14.4\%}{\sqrt{E_T}} \oplus 0.7\% \tag{3.7}$$

while the energy resolution of the hadronic part:

$$\frac{\sigma_E}{E} = \frac{80\%}{\sqrt{E_T}} \oplus 5\% \tag{3.8}$$

The plug shower-maximum (PES) detector consists of strips of scintillator located at about $6X_0$ inside the PEM and providing position measurements with resolution of around 1 mm.

It should be noted that the segmentation of the calorimeters is rather large and thus it is quite possible that the energy measured by a particular tower was contributed to by multiple particles. Occasionally this poses a problem as the energies of the individual particles can not be determined. In other situations, most notably when a "jet" of particles that results from hadronization of a quark or gluon coming directly from hard scattering hits the calorimeter, the total energy of all component particles is exactly the information that is needed.

3.2.3 Muon detection

Muons are 200 times heavier than electrons, so they lose substantially less energy due to electromagnetic interactions as they travel through the calorimeter material. This allows the muons to pierce through the calorimetry subsystem after they exit the tracking volume. The CDF muon subsystem consists of several chambers that are located outside of the calorimeters and includes Central MUon detector (CMU), Central Muon uPgrade (CMP), Central Muon eXtension (CMX). Due to space and

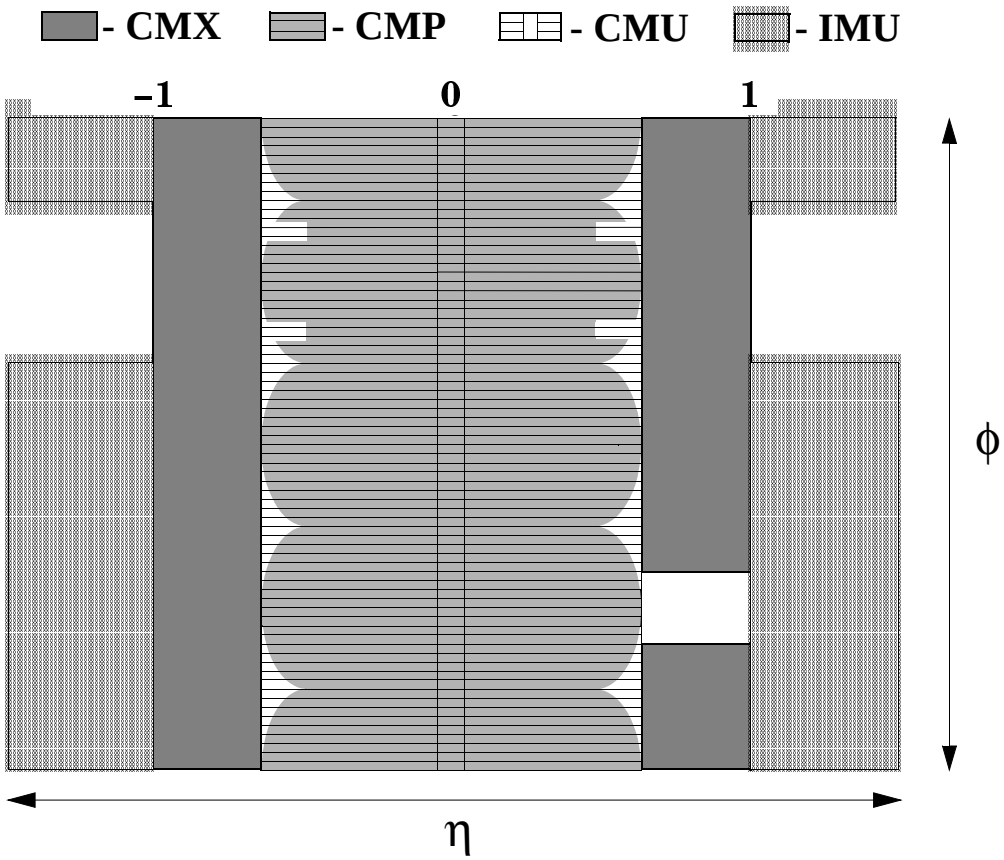

Figure 3.4: Muon subsystem coverage

design constraints the muon coverage is incomplete. Figure 3.4 shows the $\phi-\eta$ regions that are instrumented.

The CMU is comprised of series of rectangular drift cells four layers deep. The hits registered in at least 3 out of 4 layers form a "stub", which after being properly matched with the corresponding COT track suggests the presence of a muon.

The CMP subdetector consists of both drift chambers and scintillator plates and functions similar to the CMU by providing a "stub" that is used in muon reconstruction. The coverages of CMP and CMP partially overlap, refer to Figure 3.4. The CMP is placed behind additional 60 cm of steel and thus is less sensitive to remnant

hadrons that penetrate through CHA (punchthrough hadrons).

The CMX subsystem, like CMP, combines drift cells and scintillator plates arranged in semi-conical arches that cover the pseudo-rapidity region of $0.6 < |\eta| < 1.0$.

3.2.4 Event reconstruction

The event data read out by the CDF detector has to undergo event reconstruction which, roughly speaking, converts tracking system hits, calorimeter energy deposition measurements and muon chamber stubs into physics objects that are associated with certain particles. The physics objects that are immediately relevant to this analysis consist of so called high-P_T leptons — electrons or muons, jets and "missing E_T", $\not\!\!E_T$ — a measure of transverse momentum imbalance that is associated with neutrinos that escape the detector.

Electron identification starts with large energy deposition in the EM part of the calorimeter. An existence of a high-P_T track that matches the calorimeter readout is required as well as properties of the calorimeter shower profile — unlike a hadronic shower that spreads into hadronic section and often spills over into neighboring towers, electromagnetic showers are short and well localized. A number of other requirements are imposed on an electron candidate and due to different instrumentation these requirements vary for different pseudo-rapidity ranges.

Central electrons (CEM) propagate through the region of the detector with $|\eta| < 1.1$. The following list summarizes the identification criteria that a high-P_T central electron has to satisfy:

- $E_T > 20$ GeV [7]
- $P_T > 10$ GeV [8]

[7] determined from the calorimeter energy deposition
[8] from COT track curvature

- $E_{\rm had}/E_{\rm em} < 0.055 + 0.00045 \times E_{\rm tot}$
- $E/P < 2$ when $E_T < 100$ GeV or $P_T < 50$ GeV
- $L_{\rm shr} < 0.2$ [9]
- -3.0 cm $< Q \times \Delta x < 1.5$ cm, $|\Delta z| < 3$ cm [10]
- $\chi^2_{\rm strip} < 2$ [11]
- $z_{\rm vertex} < 60$ cm
- track quality requirement[12]
- fiducial[13]
- not a conversion
- $E_T^{\rm iso}/E_T^{\rm cluster} < 0.1$ [14]

Plug electrons are required to have $1.2 < |\eta| < 2.0$ and energy deposition in PEM. The electron candidates with no track requirements are called PEM, while so called Phoenix electrons (PHX) use PES information and PEM energy to find the best match between them and a silicon track. The identification requirements are summarized below:

- $E_T > 20$GeV [15]

[9] lateral shower profile variable, a measure of deviation of energy depositions in cluster towers from typical energy depositions observed in electron test-beam data

[10] Δx and Δz are the $r-\phi/r-z$ distances between the COT track and the matching CES cluster

[11] comparison of the CES $r-z$ profile to the electron test beam profile

[12] track must pass through 3 axial and 3 stereo COT superlayers with at least 7 (out of 12) hits in each

[13] must traverse a well-instrumented detector region

[14] $E_T^{\rm iso}$ is the energy transverse to the beam direction in the cone of $\Delta R < 0.4$ around the cluster excluding the electron cluster itself

[15] as measured by PEM

- $E_{\rm had}/E_{\rm em} < 0.05$
- $U_{5\times9} \geq 0.65$ and $V_{5\times9} \geq 0.65$ [16]
- $\chi^2_{3\times3} < 10$ [17]
- $\Delta R_{\rm PES} < 3$ cm [18]
- $N_{\rm Si} \geq 3$ [19]
- $|z_0| < 60$ cm
- $E_T^{\rm iso}/E_T^{\rm cluster} < 0.1$

Muon candidates are subdivided into several categories according to the detector subsystems that they propagate through. Muons that produce stubs in both CMU and CMP chambers are called CMUP muons. The coverage of muon subsystems is different and the muons that have a stub in either CMU or CMP are labeled CMU-only or CMP-only muons. Muons that traverse and create a stub in CMX are called CMX. The COT tracks with no associated stubs are also considered as muon candidates if they deposit minimum energy in calorimeters. Such muon candidates are denoted CMIO, central minimum ionizing objects. The list below summarizes additional criteria that a muon candidate has to satisfy:

- $P_T > 20$ GeV
- $|z_0| < 60$ cm
- impact parameter $d_0 < 0.2$ cm for tracks without Silicon hits, $d_0 < 0.02$ cm otherwise

[16] these variables provide a kind of isolation requirement
[17] fit of the energy distribution in neighboring nine towers to the electron test-beam data
[18] the distance between the best fit cluster center and PES centroid position, also applied to PHX tracks
[19] number of Silicon hits

- track quality[20]
- $E_{\rm em} \leq 2 + \max(0; 0.0115(P - 100))$ GeV
- $E_{\rm had} \leq 6 + \max(0; 0.0280(P - 100))$ GeV
- $E_{\rm em} + E_{\rm had} > 0.1$ GeV (for CMIO only)
- $|\Delta x|_{\rm CMU} \leq 3$ cm (CMUP or CMU-only)
- $|\Delta x|_{\rm CMP} \leq 5$ cm (CMUP or CMP-only)
- $|\Delta x|_{\rm CMX} \leq 6$ cm (CMX)
- $E_T^{\rm iso}/P_T < 0.1$ [21]
- not a cosmic ray[22]

Quarks and gluons produced in the collisions undergo fragmentation as they travel away from the interaction point. This results in a stream of energetic colorless particles propagating in a relatively narrow cone around the original parton's direction — a hadronic jet. Most typically a jet consists of charged and neutral pions, kaons and to a lesser extent light baryons, like protons and neutrons. The energy of the original parton is inferred from the sum of energy depositions of jet constituents in calorimeter towers. Jet clustering is the procedure whereby the energy in nearby calorimeter cells is joined together in order to include as much as much as possible the energy depositions associated with the original parton, while excluding the energies that are not directly related to it.

[20] at least 7 COT hits on at least 3 axial and 3 stereo COT superlayers

[21] where $E_T^{\rm iso}$ is the transverse energy in the cone of $\Delta R = 0.4$ around the muon track excluding the tower associated with the track

[22] cosmic filter algorithm relies on various timing measurements

The jet clustering starts with the most energetic calorimeter tower in a cluster, called a seed tower, and computes the energy sum in a cone of a given $\Delta R = \sqrt{\Delta\eta^2 + \Delta\phi^2}$. This analysis uses the cone size of $\Delta R = 0.4$. After a cluster is formed around the seed tower, the position of an E_T-weighted centroid is computed as:

$$\begin{aligned} \eta_{\text{centroid}} &= \frac{\sum_{\text{towers}\in\text{cluster}} E_T^i \eta^i}{\sum_{\text{towers}\in\text{cluster}} E_T^i} \\ \phi_{\text{centroid}} &= \frac{\sum_{\text{towers}\in\text{cluster}} E_T^i \phi^i}{\sum_{\text{towers}\in\text{cluster}} E_T^i} \end{aligned} \tag{3.9}$$

The centroid position defines the new cluster center and the new clustering cone is drawn around it. The process is repeated until the cluster remains unchanged. In some situations the clusters overlap and are either merged if the overlap is more than 75% or left unchanged.

A jet "raw" four-momentum is then determined based on the energy of the cluster and the position of the centroid. There are a lot of effects both physics and detector that contribute to the deviation of the jet four-momentum constructed as outlined above and the four-momentum of the original parton. Several corrections are applied to the raw quantities:

$$E_T^{\text{corr}} = (E_T^{\text{raw}} \times f_{\text{rel}} \times f_{\text{time}} \times f_{\text{scale}} - E_T^{\text{MI}}) \times f_{\text{abs}} - E_T^{\text{UE}} + E_T^{\text{OC}} \tag{3.10}$$

where the corrections are the following:

- Level 1: relative correction, f_{rel}, detector-η dependent, take into account differences in tower-by-tower calorimeter response
- Level 2: time-dependent correction, f_{time}, compensates for calorimeter deterioration over time, due, for instance, to aging of the phototubes
- Level 3: raw energy scale, f_{scale}, accounts for non-linearities in single-particle

response, determined from the photon-jet balancing

- Level 4: multiple interactions, E_T^{MI}, corrects for the possibility of several interactions in a particular bunch-crossing, parametrized by the number of vertices in the event

- Level 5: absolute energy correction, f_{abs}, a P_T-dependent factor obtained from the Monte Carlo as a mean ratio of parton P_T to the jet P_T

- Level 6: underlying event, E_T^{UE}, accounts for any contributions to the jet energy not coming from the original parton, beam remnants, spectator partons

- Level 7: out-of-cone correction, E_T^{OC}, parametrized by P_T and determined from Monte Carlo, accounts for the energy deposited outside of the cone due to gluon radiation and fragmentation effects.

Jet corrections are important to this analysis as one of the largest systematic uncertainties in the final measurement of the mass is the uncertainty in the jet energy scale. A lot of effort s been invested by the CDF collaboration into studies of jet energy and relations between measured jet energy and the energy of the original parton. This analysis builds upon the understanding accumulated in the process.

The so called "missing energy" or $\not\!\!E_T$ is a reconstructed object that is not directly related to a single particle produced in a collision. Considered as a two-component vector that lies in the plane transverse to the beam direction it is simply the negative of the sum of all transverse momenta in the event. More precisely, the uncorrected $\not\!\!E_T$ is the negative of the vector sum of all calorimeter tower depositions projected on the transverse plane.

The missing energy is often thought of as a measure of the sum of the momenta of the particles that escape detection, most notably neutrinos. In order to be more

readily interpretable as such the raw $\not{E}_T$ needs to be corrected:

$$\vec{\not{E}}_T^{\,\text{corr}} = \vec{\not{E}}_T^{\,\text{raw}} - \sum_{\text{muons}} (\vec{P}_T^{\mu} - \vec{E}_T^{\mu}) - \sum_{\text{jets}} (\vec{E}_{T,\text{jet}}^{\text{corr}} - \vec{E}_{T,\text{jet}}^{\text{raw}}) \tag{3.11}$$

The corrections here account for the fact that a large fraction of the muon energies are not seen by the calorimeters and for the fact that there is a known discrepancy between a jet and a corresponding parton energy that can be carefully corrected for.

Chapter 4

Event Selection

In the previous chapter it was briefly outlined how the proton-antiproton collisions are produced and how the data is collected and processed to form physics objects. Obviously, not every event recorded contains a $t\bar{t}$ production and decay. This chapter delves into how the stream of data is sifted through in order to find top-quarks.

4.1 Trigger System

The Tevatron accelerator produces bunches of protons and anti-protons that pass through each other at the interaction point every 396 ns. The total proton-antiproton interaction cross-section and the instantaneous luminosity are such that roughly one interaction per bunch-crossing is expected.

It is neither possible nor necessary to record every collision event. The storage capacity and data transfer rates are constrained. It takes about 2 ms to read out the entire detector and the size of the resulting event record is about 200 kB which in turn results in a data output of about 250 MB/s.

The CDF Trigger system is designed to reduce the output data rate while retaining

high efficiency for a variety of physics processes by multi-stage real-time event filtering. Each level selects "interesting" events according to certain criteria and only events that are accepted at lower level are passed on to the next trigger level.

The Level 1 trigger is a custom designed hardware trigger that is able to find simple physics objects, or primitives, and makes decisions based solely on the number of primitives in the event. The information from the detector is buffered into 42-event deep pipeline and the processing is done in 3 parallel streams. It may take up to 5.5μs for the Level 1 processor to make a decision. One of the streams analyzes calorimeter information in search of objects that may further be reconstructed into electrons, photons or jets. Another stream searches muon subsystems data for track segments or "stubs". The third stream deals with tracking data via its eXtremely Fast Tracker (XFT) and extrapolation unit (XTRP) that matches tracks found by XFT to calorimeter and muon data. The event rate is reduced from 2.5 MHz to about 50 kHz with the corresponding rejection rate of about 150.

The Level 2 trigger is also a hardware system that includes a special purpose processor that perform limited event reconstruction on the events accepted by Level 1 and stored in one of the four asynchronous event buffers. After the limited reconstruction is done the Level 2 programmable processors examine the resulting data and make a decision based on whether any of the defined Level 2 trigger criteria are satisfied. The latency of the Level 2 system is around $20 - 30\mu$s. The data rate is further reduced down to $200 - 300$ Hz. A Level 2 trigger decision to accept an event leads to the entire detector to be read out.

After the Level 2 "accept" decision the digital data from the entire detector is sent to the Event Builder CPU nodes that perform the assembly of all the event fragments into complete event records suitable for data analysis. The event data is then passed on to the Level 3 trigger system that consists of a farm of parallel general-purpose

processor nodes. The full information and improved resolution available at this stage enables more detailed event reconstruction and accurate trigger decision. In case the event is accepted by Level 3 the data is passed on to the output node and committed to the permanent storage. The data rate reduction is about a factor of 4 and the total event rate becomes 75 Hz which is quite acceptable. The overview of the CDF trigger system is presented in Figure 4.1.

4.2 DIL dataset

The selection of the events that have a high probability of being a $t\bar{t}$ is a complex multi-stage process. Other CDF physics analyses, most notably the $t\bar{t}$ cross-section measurement, have the sample composition studies and optimization of the event selection criteria with respect to number of events selected versus the amount of background (non-$t\bar{t}$) as a centerpiece and a foundation.

Our mass measurement chooses to build upon the expertise acquired by the cross-section measurement group and follows the event selection criteria that was developed. The dataset that was adopted for use is called "DIL", which is very similar in spirit to that used in the CDF Run I cross-section measurement. The tradeoffs made by this selection favor lower background levels at the cost of smaller total number of events in the sample.

The event selection starts with the inclusive central electron, inclusive muon and plug calorimeter datasets that are described in more detail in Appendix A, which also lists all the categories of dilepton candidate events that are considered in this analysis. A number of additional requirements are imposed on these primary datasets. They are:

- 2 leptons with $p_T > 20$ GeV, at least one of which is considered a well-identified,

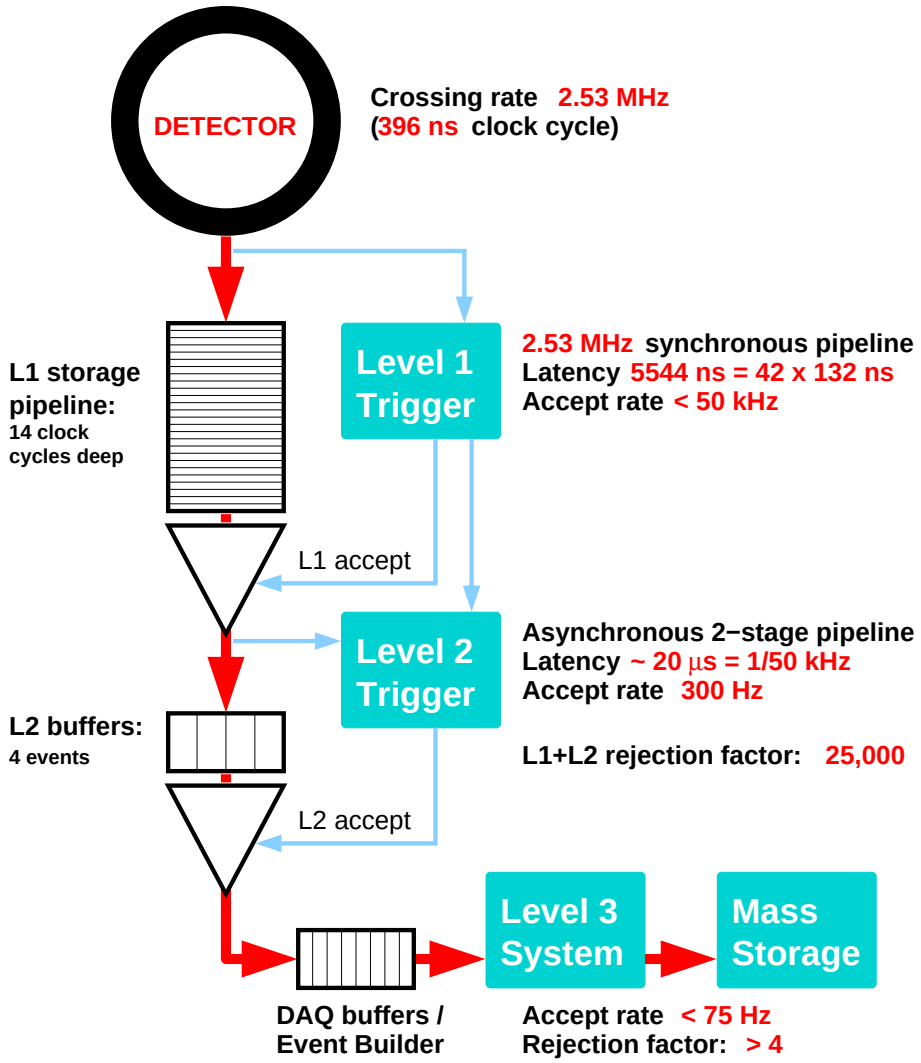

Figure 4.1: CDF Data Acquisition system

isolated[1], lepton.

- 2 or more jets with level 5 corrected $E_T > 15$ GeV and $|\eta| < 2.5$
- $\not\!\!E_T > 25$ GeV [2]
- if $\not\!\!E_T < 50$ GeV the angle between $\not\!\!E_T$ and any jet or lepton in the event is required to be at least 20 degrees
- $H_T > 200$ GeV, where H_T is the sum of all transverse energies in the event: $\not\!\!E_T$, lepton E_T-s and E_T-s of all tight jets
- require leptons to have opposite sign charges
- Z-veto requirement: in ee and $\mu\mu$ events with dilepton invariant mass between 76 and 106 GeV require "jet significance" $\sigma_j > 8.0$ [3] and $\Delta\phi_j > 10$ degrees[4]

In addition to these selection criteria, cosmic ray removal and conversion removal are performed on events from the data.

For any final dataset, which is determined by the event selection procedure used, it is possible to estimate the fraction of the events of a certain type that pass all the requirements. This quantity, called acceptance, depends on the values of event cuts. In our case it can also be considered a function of the assumed top-quark mass as the samples of different mass have different spectra in selection variables and thus the fractions of accepted events to the total are different. Figure 4.2 shows the dependence of the acceptance on the top quark pole mass. For several reasons that may become

[1]An isolated lepton is one for which no more than 10% extra energy is measured in a cone of $\Delta R \equiv \sqrt{(\Delta\phi)^2 + (\Delta\eta)^2} \leq 0.4$ around the lepton.

[2]$\not\!\!E_T$ in the events was corrected for the muon energies as well as for jet energy scale corrections

[3]where "jet significance" σ_j is defined as: $\sigma_j = \not\!\!E_T / \sum_k (\vec{\not\!\!E_T} \cdot E_T^k)$ and the sum is performed over all tight jets that are in the same hemisphere with $\not\!\!E_T$ vector; the scalar product is understood as a product of 2D vectors

[4]where $\Delta\phi_j$ is defined as a minimum angle between $\not\!\!E_T$ and any tight jet in the event

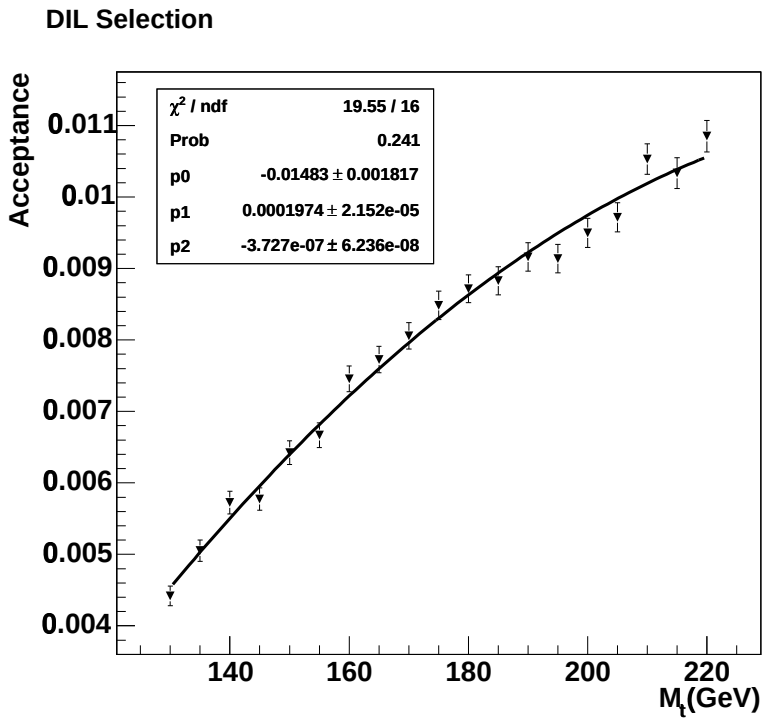

Figure 4.2: Acceptance of the DIL selection as a function of top pole mass, parametrized by $p_0 + p_1 M_t + p_2 M_t^2$.

clear later the acceptance curve plays an important role in the measurement of the mass but the absolute values of the acceptance are not crucial. The most relevant feature is the shape — relative change of the acceptance with mass.

Another piece of information that this analysis relies on is the expected sample composition. The knowledge of the expected numbers of events from the signal process and other processes that contribute to the sample is necessary for the construction of appropriate likelihood expression. Major background processes include diboson production accompanied by two jets from initial or final state gluon radiation, Drell-Yan process[5] with two extra jets, events where one of the reconstructed leptons is in fact a hadronic jet which has fragmented (and interacted in the detector) in such

[5] $\ell\bar{\ell}$ pair production via either Z boson production or virtual photon

Process	N_{DIL}
$t\bar{t}$	17.2 ± 1.4
WW	1.23 ± 0.21
WZ	0.40 ± 0.07
DY$\rightarrow ll$	4.66 ± 1.3
Fakes	3.5 ± 1.4
DY$\rightarrow \tau\tau$	0.77 ± 0.16
Total	27.7 ± 2.3

Table 4.1: Expected sample composition in $\int L = 340pb^{-1}$. The number of expected $t\bar{t}$ events assumes $\sigma_{t\bar{t}} = 6.7$ pb and $M_t = 175$ GeV.

a was as to pass all the electron identification requirements ("fakes") and Drell-Yan production of a Z boson, which then decays to $\tau\bar{\tau}$, with extra jets. Table 4.1 shows the expected sample composition for the DIL sample of the appropriate acquired integrated luminosity.

The number of expected $t\bar{t}$ events is quoted for the assumed top-quark pole mass of $M_t = 175$ GeV and the corresponding $t\bar{t}$ production cross-section $\sigma_{t\bar{t}} = 6.7$ pb. It is worth mentioning that the signal cross-section is a strong function of the assumed top-quark mass and thus the expected sample composition is adjusted by extrapolating the expected number of signal events via the known functional form of the cross-section dependence on the mass, as previously shown in Figure 2.3. Both the likelihood expression and the construction of the appropriate pseudo-experiments rely on it.

Chapter 5

Matrix Element and the measurement of mass

The most direct approach to the measurement of the top quark mass is based largely on Monte Carlo event generators. This approach is well-established among high-energy physicists and is extensively used in variety of analyses. The detailed theoretical understanding of the physics processes is incorporated in these generators to create events and simulate the entire detector response. This approach works rather well when the data is abundant and the quantities of interest can be extracted from just a couple of observables by comparing their distributions in the data to the Monte Carlo predictions.

One perceived shortcoming becomes obvious when researchers try to incorporate as much information as possible by using most of the observables in the event. Many of the methods that rely heavily on Monte Carlo event generation implicitly try to evaluate probability values for the observed data events by interpolating between the generated events. To put it another way: the density of Monte Carlo events in the space of observable variables approximates the probability density which is

then estimated at the points with observable values from the data. Thus, it is not surprising that progressively more and more generated events are needed to sample the space of higher dimensions as the quality of interpolation critically depends on it, especially for feature-rich observable spaces.

The key idea of the matrix-element based analyses is that it should be possible, at least in principle, to employ our understanding of the underlying physics process to explicitly evaluate the likelihood for a particular event, data or Monte Carlo generated, by computing the squared matrix element and further the differential cross-section. The latter almost immediately leads to the probability density in the space of observable variables. The simulation still plays an important role, but now mainly to provide a model for detector response. The treatment of the underlying physics changes from approximation to evaluation. The evaluation is not totally precise as a number of simplifying assumptions needed to be made. However the gain is still clearly visible as will be shown further.

5.1 Construction of the posterior probability

What does our data tell us about the mass? There are several ways to answer this question and one of them is to use a Bayesian approach and construct a posterior probability distribution $p(M_t|\{\text{data}\})$, which tells us, given the data that was taken, how likely are the different values of the top quark mass.

The construction of the posterior probability starts with the per-event likelihood $p(\mathbf{x}|M_t)$, which is the probability of observing an event with the measured variables $\mathbf{x}$, given a top quark pole mass of M_t:

$$p(\mathbf{x}|M_t) = \frac{1}{\sigma(M_t)} \frac{d\sigma(M_t)}{d\mathbf{x}} \tag{5.1}$$

where $\frac{d\sigma}{d\mathbf{x}}$ is the per-event differential cross-section. Naturally, the probability density for the entire dataset would be simply a product of the per-event probability densities, as the events are deemed independent of each other:

$$p(\{\mathbf{x}_i\}|M_t) = \prod_i p(\mathbf{x}_i|M_t) \tag{5.2}$$

where the index, i, runs over all the events in the dataset.

The explicit assumption of a uniform prior distribution of top-quark mass is made, within a wide enough interval that encloses the current world's average:

$$p(M_t|\{\mathbf{x}_i\}) \propto p(\{\mathbf{x}_i\}|M_t) \tag{5.3}$$

The Standard Model could be used to calculate the per-event probabilities directly if all of the parton level quantities were observed. This is not the case. One of the big deviations from such ideal situation is due to the presence of two neutrinos that can not be detected. The other major factor is the impossibility of direct measurement of quark momentum. It has to be inferred from the momentum of the corresponding hadronic jet. The detector response is parametrized by the *transfer functions* that relate certain observed quantities to the parton-level ones. The quantities that are not measured directly are effectively "hidden" and have to be integrated over:

$$p_{t\bar{t}}(\mathbf{x}|M_t) = \frac{1}{N}\int d\Phi_{\text{part}}|\mathcal{M}_{t\bar{t}}(p_{\text{part}}; M_t)|^2 f(p_{\text{obs}}, p_{\text{part}}) f_{\text{PDF}}(q_1) f_{\text{PDF}}(q_2) \tag{5.4}$$

where the integration is done over the phase space of final state partons, unobserved, and $f(p_{\text{obs}}, p_{\text{part}})$ denotes a set of transfer functions that relate parton-level quantities to the observed ones, effectively parameterizing certain physics like hadronization and the detector response. The q-s are the four-vector of incoming partons, f_{PDF} is

the parton-distribution function of the colliding protons. The overall normalization constant is such that the integral over the entire space of observables is unity:

$$\int d\mathbf{x}\ p(\mathbf{x}|M_t) = 1 \tag{5.5}$$

Constraints such as momentum conservation which appear as delta functions and affect the integration are implicitly included within the phase space volume element. They are discussed in greater detail later on.

5.2 Treatment of the backgrounds

The per-event signal probability $p_{t\bar{t}}(\mathbf{x}|M_t)$ is sufficient to extract the top quark mass from an event sample that consists entirely of $t\bar{t}$ dilepton events. However, the top quark candidate events collected by CDF include some number of background events that mimic the $t\bar{t}$ event signature. Thus, the generalized per-event probability expression takes the form:

$$p(\mathbf{x}|M_t) = p_s(\mathbf{x}|M_t)p_s + p_{b1}(\mathbf{x})p_{b1} + p_{b2}(\mathbf{x})p_{b2}... \tag{5.6}$$

which is a sum of the probability densities for each process, weighted by their respective prior probabilities.

There are two conceptually different approaches to the mass measurement. Both are heavily affected by the fact that the top quark cross-section is strongly dependent on the assumed top mass. The first method, the one that is used in this analysis, does not use the information about the observed number of events and the measured acquired luminosity. It focuses on the mass measurement itself and thus has just one free parameter — the mass. The second method effectively combines the mass mea-

surement with the cross-section measurement and utilizes both the observed number of events and the luminosity measurement to extract two parameters simultaneously.

For the ease of presentation the formula presented from this point on have just one background component. In reality this is trivially extended to include as many backgrounds as necessary. To reiterate, the single-event likelihood is written as:

$$p(\mathbf{x}_i|M_t) = p(\mathbf{x}_i|s, M_t)p(s) + p(\mathbf{x}_i|b)p(b) \tag{5.7}$$

where $p(s)$ and $p(b)$ are the *a priori* probabilities of a given event to be signal or background. They satisfy the normalization condition: $p(s) + p(b) = 1$.

Properly normalized conditional probabilities from (5.7) can be expressed in term of differential cross-sections for signal and background and acceptance-adjusted total cross-sections:

$$p(\mathbf{x}_i|s, M_t) = \frac{1}{\sigma_s \epsilon_s}\left(\frac{d\sigma_s}{d\mathbf{x}_i}\right) \tag{5.8}$$

$$p(\mathbf{x}_i|b) = \frac{1}{\sigma_b \epsilon_b}\left(\frac{d\sigma_b}{d\mathbf{x}_i}\right) \tag{5.9}$$

where $\epsilon_{s,b}$ reflects the entire acceptance efficiency, including detector acceptance and selection efficiency.

The acceptance-adjusted total cross-sections are defined as the integrals of respective differential cross-section over the accepted regions:

$$\sigma_s \epsilon_s = \int_{\texttt{accepted}} \left(\frac{d\sigma_s}{d\mathbf{x}}\right) d\mathbf{x} \tag{5.10}$$

$$\sigma_b \epsilon_b = \int_{\texttt{accepted}} \left(\frac{d\sigma_b}{d\mathbf{x}}\right) d\mathbf{x} \tag{5.11}$$

The expected number of signal and background events are expressed as (5.12, 5.13)

$$\lambda_s = \mathcal{L}\sigma_s\epsilon_s \tag{5.12}$$

$$\lambda_b = \mathcal{L}\sigma_b\epsilon_b \tag{5.13}$$

where $\mathcal{L}$ is the total luminosity.

It is important to note that the number of signal and background events are independently Poisson-distributed with parameters given by the above expected numbers (5.12, 5.13). The expected number of background events does not depend on the parameter of interest. The signal fraction of the sample, on the other hand, depends on the mass parameter through the mass-dependent expected number of signal events.

The total acceptance-adjusted cross-sections can be expressed in term of expected number of signal and background events. The dependence of the acceptance adjusted total cross-section on the mass is parametrized with parameters determined using Monte Carlo samples of different mass. Let us denote the total accepted signal cross-section as $(\sigma_s\epsilon_s)(M_t)$. The sample composition is given by the expected number of signal events $\lambda_s(M_t)$ and background λ_b. For assumed top mass m_0 the sample composition is estimated by the $t\bar{t}$ production cross-section measurement group and are presented in [17] and in more detail in [18]. The expected numbers of events of each type are dependent on the selection used. We introduce the normalization factors $\mathcal{N}_s$ and $\mathcal{N}_b$ which, when multiplied by the corresponding differential cross-sections,

produce the proper probability densities:

$$
\begin{aligned}
p_s(\mathbf{x}_i|M_t) &= \frac{d\sigma_s}{d\mathbf{x}_i}\frac{(\sigma_s\epsilon_s)(m_0)}{(\sigma_s\epsilon_s)(M_t)\,\mathcal{N}_s(m_0)} \\
p_b(\mathbf{x}_i) &= \frac{d\sigma_b}{d\mathbf{x}_i}\frac{1}{\mathcal{N}_b} \\
\lambda_s(M_t) &= \frac{\lambda_s(m_0)}{(\sigma_s\epsilon_s)(m_0)}(\sigma_s\epsilon_s)(M_t)
\end{aligned}
\tag{5.14}
$$

The per-event probability density is then given by:

$$
\begin{aligned}
p(\mathbf{x}_i|M_t) &= p_s(\mathbf{x}_i|M_t)\frac{\lambda_s(M_t)}{\lambda_s(M_t)+\lambda_b} + p_b(\mathbf{x}_i)\frac{\lambda_b}{\lambda_s(M_t)+\lambda_b} \\
&= \left[\frac{d\sigma_s}{d\mathbf{x}_i}\frac{\lambda_s(m_0)}{\mathcal{N}_s(m_0)} + \frac{d\sigma_b}{d\mathbf{x}_i}\frac{\lambda_b}{\mathcal{N}_b}\right]\left(\frac{1}{\frac{\lambda_s(m_0)}{(\sigma_s\epsilon_s)(m_0)}(\sigma_s\epsilon_s)(M_t)+\lambda_b}\right)
\end{aligned}
\tag{5.15}
$$

The likelihood expression for the entire dataset is, of course, simply a product of per-event probability densities given by (5.15):

$$
p(\{\mathbf{x}\}|M_t) = \left(\frac{1}{\frac{\lambda_s(m_0)}{(\sigma_s\epsilon_s)(m_0)}(\sigma_s\epsilon_s)(M_t)+\lambda_b}\right)\prod_i\left[\frac{d\sigma_s}{d\mathbf{x}_i}\frac{\lambda_s(m_0)}{\mathcal{N}_s(m_0)} + \frac{d\sigma_b}{d\mathbf{x}_i}\frac{\lambda_b}{\mathcal{N}_b}\right] \tag{5.16}
$$

Chapter 6

Transfer functions

The per-event probability density which was introduced in the previous Chapter is a function of the observed variables. The model of the underlying physics process, on the other hand, is defined in terms of parton-level quantities, many of which are not observed directly in the detector environment. The task of bridging the gap between the two is assigned to the transfer functions.

It is possible to think of transfer functions in terms of conditional probabilities that quantify how likely it is to measure certain reconstructed event properties given "true" underlying values of the parton-level quantities. A conditional probability distribution that maps all the hidden event quantities to those observed is, at least in principle, not impossible to construct. It is, however, impractical and, as will be shown later, computationally expensive. Thus, various simplifying approximations are made. These approximations allow the transfer function to be factorized into separate simpler functions, some of which we deliberately replace with Dirac δ-functions. The latter is another way of saying that we presume certain variables to be measured precisely by the detector. Among these are lepton momenta and jet angles. Jet energies, on the other hand, although directly related to the energy of the parent b-quark,

usually are quite different.

In accordance with the general interpretation of transfer functions as the probability of reconstructing objects with properties y given the corresponding variables x immediately after the hard-scattering process, the jet energy transfer function $f(E_{parton}, E_{jet})$ describes the probability of a parton with energy E_{parton} to be measured as a jet with energy E_{jet} in the CDF detector.

6.1 Parameterization of $f(E_{parton}, E_{jet})$

The method of extraction and parametrization of the jet energy transfer function largely follows D0 Run I matrix element analyses, [19], [20]. It is based on the joint distribution of parton and jet energies in the simulated events:

$$n(E_{jet}, E_{parton})dE_{jet}dE_{parton} = n(E_{parton})dE_{parton}f(E_{parton}, E_{jet})dE_{jet} \tag{6.1}$$

where $n(E_{jet}, E_{parton})dE_{jet}dE_{parton}$ refers to the number of events with jet energy between E_{jet} and $E_{jet}+dE_{jet}$ and parton energy between E_{parton} and $E_{parton}+dE_{parton}$. The $n(E_{parton})dE_{parton}$ is the number of partons with energy between E_{parton} and $E_{parton} + dE_{parton}$.

The transfer function itself is parametrized as a sum of two Gaussian distributions:

$$f(\delta) = \frac{1}{\sqrt{2\pi}(p_2 + p_3 p_5)}\Big[\exp\frac{-(\delta - p_1)^2}{2p_2^2} + p_3 \exp\frac{-(\delta - p_4)^2}{2p_5^2}\Big] \tag{6.2}$$

where $\delta \equiv E_{parton} - E_{jet}$ and each p_i depends linearly on E_{parton}:

$$p_i = a_i + b_i E_{parton} \tag{6.3}$$

One of the Gaussian functions is intended to account primarily for the peak in the joint distribution, the other to describe the tails[1]. Such parametrization results in ten fit parameters that need to be determined[2]. To extract them an unbinned likelihood fit is performed with the likelihood defined as:

$$-\ln L = -\sum_{i=1}^{N} \ln n(E^{(i)}_{parton}) - \sum_{i=1}^{N} \ln f(E^{(i)}_{parton}, E^{(i)}_{jet}) \tag{6.4}$$

Using b-quarks matched with the jets from `HERWIG` $t\bar{t}$ events for $M_t = 178$ GeV/c^2, the parameters shown in Table 6.1 are obtained. The joint distribution of jet and parton energies that these transfer functions aim to parametrize is shown in Figure 6.1.

p_i	a_i	b_i
p_1	-1.822 ± 0.623	-0.0257 ± 0.008
p_2	2.535 ± 0.540	0.078 ± 0.005
p_3	0.670 ± 0.075	0.0 ± 0.001
p_4	-1.556 ± 0.789	-0.192 ± 0.012
p_5	7.881 ± 0.665	0.099 ± 0.008

Table 6.1: Parameters for $f(E_{parton}, E_{jet})$ extracted using matched b-jet and quarks from HERWIG $t\bar{t}$ MC.

6.2 Tests of $f(E_{parton}, E_{jet})$

A simple test of the jet transfer function can be done by attempting to predict the jet energy distribution resulting from a known distribution of parton energies from Monte Carlo generated events run through a full CDF detector simulation. This is done by integrating the expression for $n(E_{jet}, E_{parton})dE_{jet}dE_{parton}$ in equation 6.1

[1]qualitatively, p_1 and p_4 describe the means of the two Gaussian distributions, p_2 and p_5 are responsible for the corresponding widths and both means and widths are allowed to float linearly with E_{parton}

[2]the parametrization of p_i can be refined by, for instance, inclusion of quadratic and cubic (in E_{parton}) terms. However, current parametrization performs well as will be shown shortly

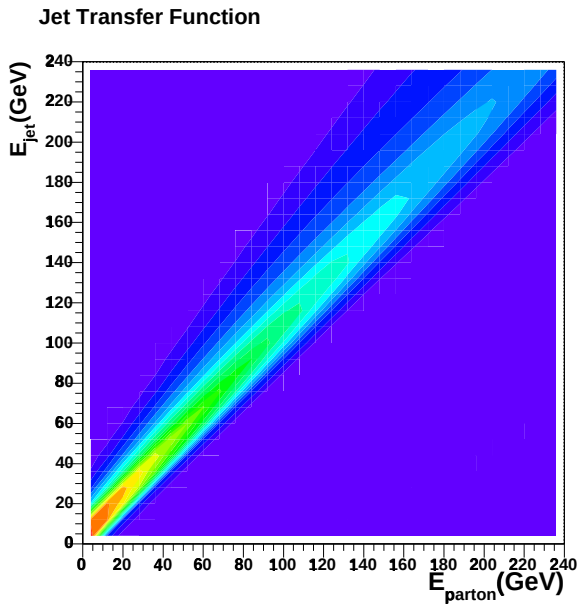

Figure 6.1: Joint distribution of E_{parton} and E_{jet}. This histogram shows (in color) the density (blue – low to red – high) of simulated partons with energies E_{parton} which are matched to jets with energies E_{jet}.

over a slice of parton energy:

$$H(E_{jet}) = \int_{E_{parton_2}}^{E_{parton_1}} n(E_{parton}) dE_{parton} f(E_{parton}, E_{jet}) \tag{6.5}$$

Such a test using $H(E_{jet})$ and a similar test using $H(E_\delta) \equiv H(E_{jet} - E_{parton})$ are shown in Figure 6.2 for the full parton energy range and in Figure 6.3 for smaller slices in parton energy.

Since the jet transfer function models the detector response to partons, it should be independent of the physics process producing these partons. This statement is tested by using $f(E_{parton}, E_{jet})$ parameterized from $M_t = 178$ GeV/c^2 events to predict the jet energy distribution resulting from b-quarks in the Monte Carlo top decays of varied top masses. Figure 6.4 shows that the jet transfer function derived using partons from $M_t = 178$ GeV/c^2 top decays can accurately predict jet energies from top decays of

M_t ranging from 150 GeV/c^2 through 200 GeV/c^2.

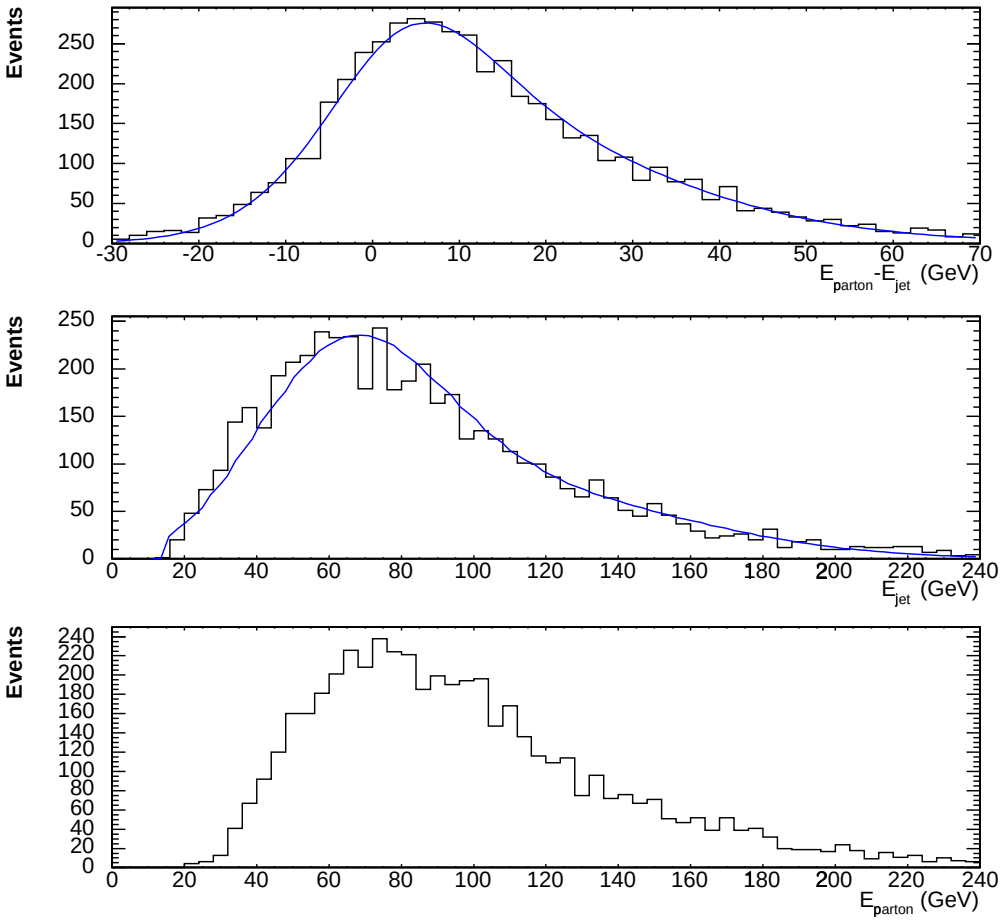

Figure 6.2: A simple test of $f(E_{parton}, E_{jet})$: the histograms show the simulated E_{jet} and $E_{parton} - E_{jet}$ distributions from a known distribution of E_{parton}. The lines show the predicted distributions for E_{jet} and $E_{parton} - E_{jet}$ as derived from E_{parton} using $f(E_{parton}, E_{jet})$. The bottom plot shows a distribution of parton energies that the predictions are based upon.

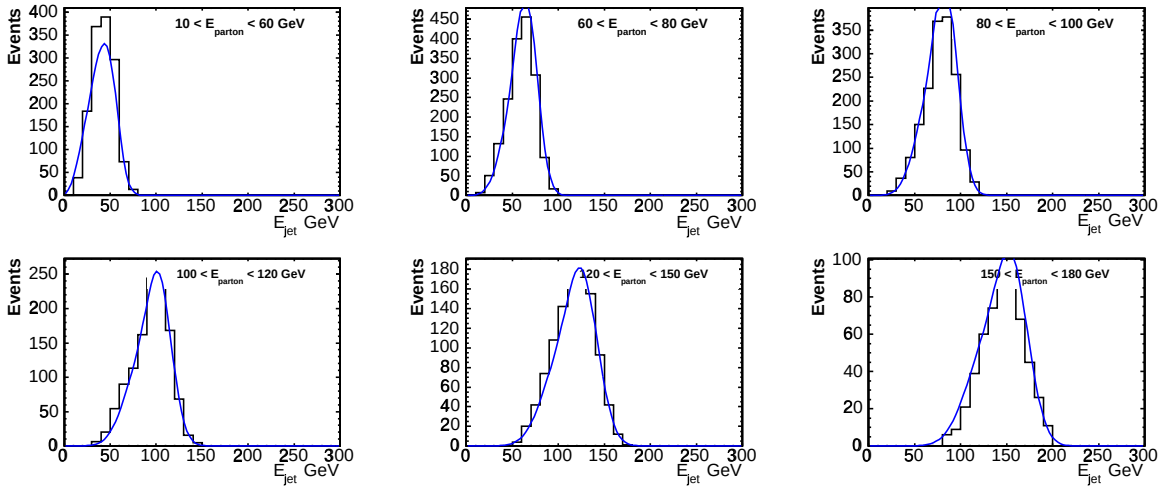

Figure 6.3: A simple test of $f(E_{parton}, E_{jet})$ over smaller ranges of E_{parton}: simulated E_{jet} from a known distribution of E_{parton} over small sub-ranges of that E_{parton} distribution. The lines shows the predicted distributions for E_{jet} as derived from E_{parton} using $f(E_{parton}, E_{jet})$.

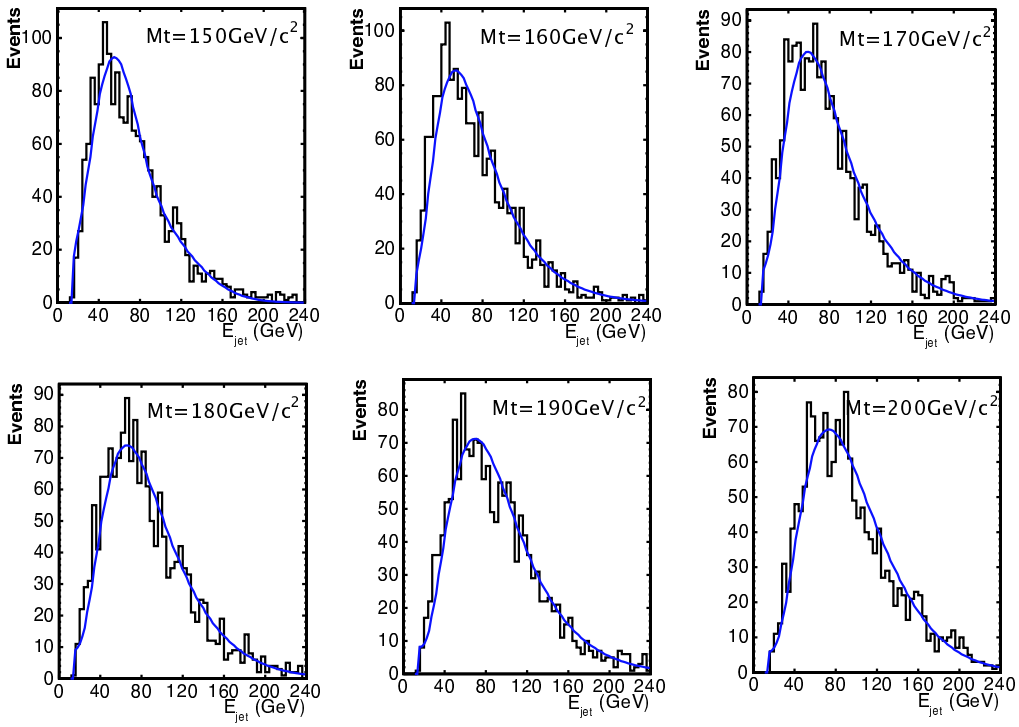

Figure 6.4: Tests of $f(E_{parton}, E_{jet})$ stability. The jet energy distributions shown are from detector simulation of b-quarks from MC $t\bar{t}$ decay of M_t = 150, 160, 170, 180, 190, and 200 GeV/c^2. The line shows the predicted jet energy distribution for each case using the parton energy distribution (not shown) and $f(E_{parton}, E_{jet})$ derived from b-quarks from MC $t\bar{t}$ decay of M_t = 178 GeV/c^2

Chapter 7

Signal Matrix Element

7.1 The Calculation

The evaluation of the per-event probability hinges on the calculation of the per-event differential cross-section of the top quark pair production and decay. The derivation of the expression that will be used to compute it starts with the cross-section for a generic $2 \rightarrow 2$ process:

$$\sigma = \int \sum_{i,j} \frac{(2\pi)^4 |\mathcal{M}|^2}{4\sqrt{(p_1 \cdot p_2)^2 - m_1^2 m_2^2}} f_{\mathtt{PDF}}(x^i) f_{\mathtt{PDF}}(x^j) d\Phi_6 dx_i dx_j \tag{7.1}$$

At the heart of the calculation is the expression for the matrix element. The expression for the production and decay process $q\bar{q} \rightarrow t\bar{t} \rightarrow (W^+ b)(W^- \bar{b}) \rightarrow (\bar{e}\nu b)(e\bar{\nu}\bar{b})$ evaluated to the leading order (LO) has the following form[1]:

$$|\mathcal{M}|^2 = \frac{g_s^4}{9} F \bar{F}$$
$$\left((2 - \beta^2 s_{qt}^2) - \frac{(1 - c_{\bar{e}q} c_{e\bar{q}}) - \beta(c_{\bar{e}t} + c_{e\bar{t}}) + \beta c_{qt}(c_{\bar{e}q} + c_{e\bar{q}}) + \frac{1}{2}\beta^2 s_{qt}^2 (1 - c_{e\bar{e}})}{\gamma^2 (1 - \beta c_{\bar{e}t})(1 - \beta c_{e\bar{t}})} \right) \tag{7.2}$$

[1] the LO matrix element expressions used are from [21, 22]

where s_{ab} and c_{ab} are respectively sine and cosine between particles a and b in the $q\bar{q}$ rest frame, β is the top-quark velocity in $q\bar{q}$ rest frame, $\gamma = (1-\beta^2)^{-1/2}$ and g_s is the strong coupling constant [2]. The top-quark propagator and decay terms are given by:

$$F = \frac{g_w^4}{4}\left[\frac{m_t^2 - m_{\bar{e}\nu}^2}{(m_t^2 - M_t^2)^2 + (M_t\Gamma_t)^2}\right]\left[\frac{m_t^2(1-\hat{c}_{\bar{e}b}^2) + m_{\bar{e}\nu}^2(1+\hat{c}_{\bar{e}b})^2}{(m_{\bar{e}\nu}^2 - M_W^2)^2 + (M_W\Gamma_W)^2}\right] \tag{7.3}$$

where m_t is the invariant mass of the t-quark decay products, $\hat{c}_{ab}$ is the cosine of the angle between particles a and b in the W^+ rest frame.

$$\bar{F} = \frac{g_w^4}{4}\left[\frac{m_{\bar{t}}^2 - m_{e\bar{\nu}}^2}{(m_{\bar{t}}^2 - M_t^2)^2 + (M_t\Gamma_t)^2}\right]\left[\frac{m_{\bar{t}}^2(1-\hat{c}_{e\bar{b}}^2) + m_{e\bar{\nu}}^2(1+\hat{c}_{e\bar{b}})^2}{(m_{e\bar{\nu}}^2 - M_W^2)^2 + (M_W\Gamma_W)^2}\right] \tag{7.4}$$

where $m_{\bar{t}}$ is the invariant mass of the $\bar{t}$-quark decay products, $\hat{c}_{ab}$ is the cosine between particles a and b in W^- rest frame. The M_t, ${\Gamma_t}^3$, M_W, Γ_W are the pole masses and widths of the top-quark and W-boson, and g_w is the weak coupling constant [4].

With the spin correlation term from Equation 7.2 omitted the expression is reduced to:

$$|\mathcal{M}|^2 = \frac{g_s^4}{9}F\bar{F}(2-\beta^2 s_{qt}^2) \tag{7.5}$$

In the calculations that follow, only the $q\bar{q} \to t\bar{t}$ production matrix element is used, while $gg \to t\bar{t}$ is neglected. Our motivation for doing so comes from the fact that only $\approx 15\%$ of the $t\bar{t}$ pair at Tevatron are produced via gluon fusion. Nonetheless, we check the legitimacy of this simplification by evaluating the corresponding systematic uncertainty, refer to Section 10.7 on page 133.

Expression (7.1) describes the total cross section for this process, σ. We require the differential cross-section with respect to observed quantities, $\frac{d\sigma}{d\mathbf{x}}$. To evaluate

[2] $g_s^2/4\pi = \alpha_s$

[3] $\Gamma(t \to Wb) = \frac{G_F}{8\pi\sqrt{2}}M_t^3|V_{tb}|^2\left(1 - 3\frac{M_W^4}{M_t^4} + 2\frac{M_W^6}{M_t^6}\right)$ at LO

[4] $G_F/\sqrt{2} = g_w^2/8M_W^2$

the differential cross-section for the observed quantities corresponding to a particular event configuration, we take the expression inside the integral, introduce conditional probability terms that relate the observed quantities to the parton level variables and subsequently integrate over all parton-level phase space.

The matrix element depends on two initial state momenta — incoming q_1 and q_2. Outgoing parton-level variables are: b-quarks p_1 and p_2, leptons ℓ_1 and ℓ_2, neutrinos ν_1 and ν_2. Observed quantities consist of jets j_1 and j_2, measured leptons L_1 and L_2 and two components of missing transverse energy.

The set of assumptions regarding the transfer between parton-level quantities and the observables consists of the following:

- Leptons are measured perfectly. This assumption effectively translates into "transfer function" for leptons being a three-dimensional δ-function

$$\delta^3(l_1 - L_1)\ \delta^3(l_2 - L_2)$$

- Jet angles are measured perfectly. Equivalently,

$$\delta(\theta_{j_1} - \theta_{p_1})\delta(\phi_{j_1} - \phi_{p_1})f(E_{p_1}, E_{j_1})\,\delta(\theta_{j_2} - \theta_{p_2})\delta(\phi_{j_2} - \phi_{p_2})f(E_{p_2}, E_{j_2})$$

  is the b-parton to jet transfer function. We will normally call the energy part "jet transfer function" for brevity[5].

[5]there is some potential ambiguity here. When dealing with δ-functions in spherical coordinates one would normally need to include extra factors, for instance:

$$\delta^3(\vec{r} - \vec{r'}) = \frac{1}{r^2}\ \delta(r - r')\ \delta(\cos\theta - \cos\theta')\ \delta(\phi - \phi')$$

We have some freedom in definition of the transfer functions and we choose to *define* it so that by integration in spherical coordinates Jacobian factors are absorbed in $f(E_j, E_p)$, angular δ-functions are $\delta(\theta_j - \theta_p)\delta(\phi_j - \phi_p)$, while $p_R^2 \sin(\theta_p) dp_R d\theta_p d\phi_p$ is the volume element. The validity of the implicit assumption that jet energy transfer functions are independent of θ or, equivalently, pseudo-

- We assume incoming partons to be massless and to have transverse momentum components $q_x \ll q_z$, $q_y \ll q_z$, where the coordinate system is chosen so that z-axis is set along the colliding beam, and x and y are in the transverse plane.

- Masses of the final state leptons are zero, masses of the b-quarks are known.

7.1.1 Introducing the notation

We begin with an expression for the differential cross-section that is given by (7.6).

$$
\begin{aligned}
d\sigma = \left(\frac{1}{(2\pi)^3}\right)^6 \iint \sum_{i,j} & |M(q_1^i, q_2^j \to \ell_1, \nu_1, p_1, \ell_2, \nu_2, p_2)|^2 \\
& (2\pi)^4 \delta^4(q_1 + q_2 - \ell_1 - \nu_1 - p_1 - \ell_2 - \nu_2 - p_2) \\
& \delta(q^x)\, \delta(q^y)\, dq^x\, dq^y\; f^i_{\texttt{PDF}}(\xi_1^i, Q^2)\; f^j_{\texttt{PDF}}(\xi_2^j, Q^2)\; f_{\texttt{flux}}(q_1^z, q_2^z)\, d\xi_1^i\, d\xi_2^j \\
& \delta^3(\ell_1 - L_1)\, \delta^3(\ell_2 - L_2)\, \frac{d^3\ell_1}{2E_{\ell_1}} \frac{d^3\ell_2}{2E_{\ell_2}} \\
& f(E_{p_1}, E_{j_1})\, f(E_{p_2}, E_{j_2}) \delta(\theta_{p_1} - \theta_{j_1})\, \delta(\theta_{p_2} - \theta_{j_2})\, \delta(\phi_{p_1} - \phi_{j_1})\, \delta(\phi_{p_2} - \phi_{j_2}) \frac{d^3p_1}{2E_{p_1}} \frac{d^3p_2}{2E_{p_2}} \\
& f_{\texttt{utf}} \frac{d^3\nu_1}{2E_{\nu_1}} \frac{d^3\nu_2}{2E_{\nu_2}}
\end{aligned}
\tag{7.6}
$$

The Bjorken variables ξ_1^i and ξ_2^j can be considered as fractions of the beam energy carried by the interacting incoming partons. We express them in terms of q_1^z and q_2^z as $\xi_1^i = q_1^z/E_{\texttt{beam}}$ and $\xi_2^i = q_2^z/E_{\texttt{beam}}$. The sum is over possible incoming parton flavors. We integrate over all the final state parton-level three-momenta (final state particles are stable).

The δ-functions in q_x and q_y constrain transverse momenta of the incoming partons

rapidity η is supported by the observation that no strong angular dependence is present. This, of course, can be refined to allow for angular dependence but is not perceived necessary for our initial analysis.

to be zero. This is not strictly true or necessary. For simplicity we use this in the derivation of the differential cross-section and show later that by a trivial change this constraint can be removed and this extra integration can be reintroduced later together with appropriate prior distributions for q_x, q_y[6].

The $f_{\texttt{utf}}$ factor is the unclustered energy transfer function. The motivation for it as well as a definition is given below. Loosely speaking, this function quantifies the dependence between parton-level momenta, measured jet energies and measured missing transverse energy.

7.1.2 Phase space transformation and Integration

In order to efficiently perform integrations over the parton-level variables, we perform a phase-space transformation which splits the original phase space into one or more subspaces, but introduces the equivalent number of extra variables and integrations. These variables are the relevant invariant masses. Some details on the formula used are provided in Appendix B and in [23]. We introduce invariant masses that correspond to intermediate t and $\bar{t}$ quarks and W-bosons.

The entire integrand after the phase space transformation results in (7.7). Each additional integration over invariant mass of the intermediate particle has a corresponding δ-function in squared invariant mass and each intermediate particle four-momenta has corresponding δ^4-function for the momentum conservation at the intermediate vertex. It would be easy to integrate over zero-components of intermediate

[6]Consider two incoming partons and their transverse momentum components: q_1^x, q_2^x, q_1^y and q_2^y. Let us change the variables to $q_x = \frac{1}{\sqrt{2}}(q_1^x + q_2^x)$, $q_y = \frac{1}{\sqrt{2}}(q_1^y + q_2^y)$, $q_u = \frac{1}{\sqrt{2}}(q_1^x - q_2^x)$ and $q_v = \frac{1}{\sqrt{2}}(q_1^y - q_2^y)$. Inspecting all the expressions that contain the transverse components we find out that they may only depend on the q_x and q_y. We may further assume that the initial momenta components are independent and Gaussian distributed. The q_u and q_v in this case are trivially integrated away — these variables are not present in the integrand and thus the integration over them (and their density) can be performed to yield unity. The resulting distribution of the q_x and q_y are also Gaussian, moreover in the absence of correlation between q_1^x and q_2^x, q_x will even have the same σ.

four-momenta that leaves only three-momenta integrals for the intermediate particles, but the algebra becomes quite involved and we chose a different approach.

$$
\begin{aligned}
d\sigma =&(2\pi)^4\,|M|^2\left(\frac{1}{(2\pi)^3}\right)^6\delta^4(q_1+q_2-t_1-t_2)\,\delta(t_1^2-M_{t_1}^2)\,d^4t_1\,\delta(t_2^2-M_{t_2}^2)\,d^4t_2\\
&\delta^4(t_1-w_1-p_1)\,\delta^4(t_2-w_2-p_2)\,\delta^4(w_1-\nu_1-\ell_1)\,\delta^4(w_2-\nu_2-\ell_2)\\
&\delta(w_1^2-M_{w_1}^2)\,d^4w_1\,\delta(w_2^2-M_{w_2}^2)\,d^4w_2\,\frac{d^3p_1}{2E_{p_1}}\frac{d^3p_2}{2E_{p_2}}\frac{d^3\nu_1}{2E_{\nu_1}}\frac{d^3\nu_2}{2E_{\nu_2}}\frac{d^3\ell_1}{2E_{\ell_1}}\frac{d^3\ell_2}{2E_{\ell_2}}\\
&\delta(q^x)\,\delta(q^y)\,dq^x\,dq^y\,f_{\texttt{flux}}(q_1^z,q_2^z)\,f^i_{\texttt{PDF}}(\frac{q_1^z}{E_{\texttt{beam}}},Q^2)\;f^j_{\texttt{PDF}}(\frac{q_2^z}{E_{\texttt{beam}}},Q^2)\;\frac{dq_1^z\,dq_2^z}{E^2_{\texttt{beam}}}\,f_{\texttt{utf}}\\
&\delta^3(\ell_1-L_1)\,\delta^3(\ell_2-L_2)\,f(E_{p_1},E_{j_1})\,f(E_{p_2},E_{j_2})\\
&\delta(\theta_{p_1}-\theta_{j_1})\,\delta(\theta_{p_2}-\theta_{j_2})\,\delta(\phi_{p_1}-\phi_{j_1})\,\delta(\phi_{p_2}-\phi_{j_2})\,dM_{t_1}^2\,dM_{t_2}^2\,dM_{W_1}^2\,dM_{W_2}^2
\end{aligned}
\tag{7.7}
$$

First we integrate over $d^3\ell_1\,d^3\ell_2$ and [optionally][7] over $dq^x\,dq^y$, making use of the corresponding δ-functions. This step results in the expression (7.8)

$$
\begin{aligned}
d\sigma =&(2\pi)^4\,|M|^2\left(\frac{1}{(2\pi)^3}\right)^6\delta\left((q_1+q_2)^0-t_1^0-t_2^0\right)\delta\left((q_1+q_2)^z-t_1^z-t_2^z\right)\\
&\delta(t_1^x+t_2^x)\;\delta(t_1^y+t_2^y)\\
&\delta(t_1^2-M_{t_1}^2)\;\delta(t_2^2-M_{t_2}^2)\;\delta(w_1^2-M_{W_1}^2)\;\delta(w_2^2-M_{W_2}^2)\;d^4t_1\;d^4t_2\;d^4w_1\;d^4w_2\\
&\delta^4(t_1-w_1-p_1)\;\delta^4(t_2-w_2-p_2)\;\delta^4(w_1-\nu_1-L_1)\;\delta^4(w_2-\nu_2-L_2)\\
&\frac{d^3p_1}{2E_{p_1}}\frac{d^3p_2}{2E_{p_2}}\frac{d^3\nu_1}{2E_{\nu_1}}\frac{d^3\nu_2}{2E_{\nu_2}}\frac{1}{2E_{L_1}}\frac{1}{2E_{L_2}}\\
&f_{\texttt{flux}}(q_1^z,q_2^z)\,f^i_{\texttt{PDF}}(\frac{q_1^z}{E_{\texttt{beam}}},Q^2)\;f^j_{\texttt{PDF}}(\frac{q_2^z}{E_{\texttt{beam}}},Q^2)\;\frac{dq_1^z\,dq_2^z}{E^2_{\texttt{beam}}}\,f_{\texttt{utf}}\;f(E_{p_1},E_{j_1})\,f(E_{p_2},E_{j_2})\\
&\delta(\theta_{p_1}-\theta_{j_1})\,\delta(\theta_{p_2}-\theta_{j_2})\,\delta(\phi_{p_1}-\phi_{j_1})\,\delta(\phi_{p_2}-\phi_{j_2})\,dM_{t_1}^2\,dM_{t_2}^2\,dM_{W_1}^2\,dM_{W_2}^2
\end{aligned}
\tag{7.8}
$$

[7] integrations over q_x, q_y can be postponed until the end and integrated with non-δ-function priors.

Next step consists of integration over

$$\delta\left((q_1+q_2)^0 - t_1^0 - t_2^0\right)\ \delta\left((q_1+q_2)^z - t_1^z - t_2^z\right)\ dq_1^z\ dq_2^z \tag{7.9}$$

The energy components in this expression are then expressed in terms of q_1^z and q_2^z in the collider approximation mentioned earlier [8]. The expressions inside these two δ-functions are used to solve for q_1^z and q_2^z in terms of the remaining variables. The entire expression gets an additional factor of 1/2 [9].

We carry on the integration with

$$\delta^4(w_1 - \nu_1 - L_1)\ \delta^4(w_2 - \nu_2 - L_2)\ d^4w_1\ d^4w_2 \tag{7.10}$$

that imposes the constraint

$$\begin{aligned} w_1 &= (L_1 + \nu_1) \\ w_2 &= (L_2 + \nu_2) \end{aligned} \tag{7.11}$$

Next integration is over t variables:

$$\delta^4(t_1 - w_1 - p_1)\ \delta^4(t_2 - w_2 - p_2)\ d^4t_1\ d^4t_2 \tag{7.12}$$

that results in:

$$\begin{aligned} t_1 &= (L_1 + \nu_1 + p_1) \\ t_2 &= (L_2 + \nu_2 + p_2) \end{aligned} \tag{7.13}$$

[8] massless incoming partons with transverse momenta of the incoming partons $q_t \ll q_z$. Here it means that without loss of generality we may substitute $q_1^0 = q_1^z$ and $q_2^0 = -q_2^z$ and make sure energies are positive.

[9] this is easily shown by either doing integrations over $dq_1^z\, dq_2^z$ one by one or by noticing that the system of coupled equations inside the two δ-functions has a Jacobian of 2.

Further integration over the angular variables of b-partons is done by first transforming the parton variables into spherical coordinates[10]:

$$d^3p \rightarrow p_R^2 \sin\theta_p d\theta_p d\phi_p dp_R \tag{7.14}$$

Then the expression takes the form:

$$\begin{aligned} d\sigma =& (2\pi)^4 \frac{|M|^2}{2} \left(\frac{1}{(2\pi)^3}\right)^6 f^i_{\texttt{PDF}}(\frac{q_1^z}{E_{\texttt{beam}}}, Q^2)\ f^j_{\texttt{PDF}}(\frac{q_2^z}{E_{\texttt{beam}}}, Q^2)\ \frac{1}{E^2_{\texttt{beam}}} \\ & \delta\left((L_1+\nu_1+p_1)_x + (L_2+\nu_2+p_2)_x\right)\ \delta\left((L_1+\nu_1+p_1)_y + (L_2+\nu_2+p_2)_y\right) \\ & \delta\left((L_1+\nu_1+p_1)^2 - M^2_{t_1}\right)\ \delta\left((L_2+\nu_2+p_2)^2 - M^2_{t_2}\right) \\ & \delta\left((L_1+\nu_1)^2 - M^2_{W_1}\right)\ \delta\left((L_2+\nu_2)^2 - M^2_{W_2}\right) \\ & \frac{p^2_{1R}\sin\theta_{p_1} dp_{1R}}{2E_{p_1}}\ \frac{p^2_{2R}\sin\theta_{p_2} dp_{2R}}{2E_{p_2}}\ \frac{d^3\nu_1}{2E_{\nu_1}}\ \frac{d^3\nu_2}{2E_{\nu_2}}\ \frac{1}{2E_{L_1}}\ \frac{1}{2E_{L_2}} \\ & f_{\texttt{flux}}(q_1^z, q_2^z)\ f_{\texttt{utf}}\ f(E_{p_1}, E_{j_1})\ f(E_{p_2}, E_{j_2})\ dM^2_{t_1}\ dM^2_{t_2}\ dM^2_{W_1}\ dM^2_{W_2} \end{aligned} \tag{7.15}$$

Dirac δ-functions have a number of properties that are used extensively in simplification of the cross-section integrals. A well known property of a δ-function in a single variable is given by (7.16)

$$\delta(g(x)) = \sum_i \frac{\delta(x - x_i)}{|g'(x_i)|} \tag{7.16}$$

where x_i are the zeros of $g(x)$. For an integral of two-dimensional function of two variables, it should be reasonably modified to:

$$\delta(\mathbf{f}(x, y)) = \sum_i \frac{\delta(x - x_i)\delta(y - y_i)}{|J(x_i, y_i)|} \tag{7.17}$$

[10] p_R denotes the radial component of a b-parton's three-momentum

where J is the determinant of the Jacobian matrix of $\mathbf{f}$ evaluated at the zero-points. Skipping the mathematically rigorous proof we will use (7.17) keeping in mind that degenerate zeroes should in theory receive special treatment.

Further integrations over 6 components of neutrino momenta and 6 "free" δ-functions has a twofold effect. First, the integration in question is equivalent to solving the system of equations that is obtained by requiring the expressions inside δ-function to equal zero. The neutrino solutions obtained in the process should then be substituted into all the expressions that depend on them and expressing the rest of the kinematic variables in term of measured variables and components of neutrino momenta. Second, the expressions inside the δ-functions are not the neutrino momenta themselves but some functions of those. Thus the entire expression is combined with the Jacobian terms that originate from this fact in a way similar to (7.17). There remain 6 extra integrations to be done at this point: 2 over the magnitudes of b-parton momenta, and 4 over the assumed invariant masses of t-quarks and W-bosons. Consequently for the purpose of finding neutrino solutions these quantities are assumed known, as the final stage integration will vary them and solve for neutrino momenta at each point of evaluation.

It should be emphasized that the sum over neutrino solutions comes naturally from the integration of δ-function (7.16), namely from the required sum over the zeroes of the δ-function argument; it makes little sense to undertake separation of neutrino solutions or to "rate" them by which one is perceived as "more likely".

7.1.3 Neutrino solutions

The system of equations for neutrino momenta is the following:

$$
\begin{aligned}
&(L_1 + \nu_1 + p_1)^2 = M_{t_1}^2 \\
&(L_2 + \nu_2 + p_2)^2 = M_{t_2}^2 \\
&(L_1 + \nu_1)^2 = M_{W_1}^2 \\
&(L_2 + \nu_2)^2 = M_{W_2}^2 \\
&(L_1 + \nu_1 + p_1)_x + (L_2 + \nu_2 + p_2)_x = 0 \\
&(L_1 + \nu_1 + p_1)_y + (L_2 + \nu_2 + p_2)_y = 0
\end{aligned}
\tag{7.18}
$$

The first two equations of (7.18) can be rewritten in the following way:

$$
\begin{aligned}
(\nu_1 \cdot p_1) &= \frac{M_{t_1}^2 - M_{W_1}^2 - m_b^2}{2} - (L_1 \cdot p_1) = a_{01} \\
(\nu_2 \cdot p_2) &= \frac{M_{t_2}^2 - M_{W_2}^2 - m_b^2}{2} - (L_2 \cdot p_2) = a_{02}
\end{aligned}
\tag{7.19}
$$

where we introduced a_{01} and a_{02} as a convenient notation. The second pair of equations from (7.18) take form:

$$
\begin{aligned}
(L_1 \cdot \nu_1) &= \frac{M_{W_1}^2}{2} = b_{01}^2 \\
(L_2 \cdot \nu_2) &= \frac{M_{W_2}^2}{2} = b_{02}^2
\end{aligned}
\tag{7.20}
$$

with additional notation introduced. Expanding the four-vector products in first four equation of (7.18) we can express ν_{1z} and ν_{2z} in terms of x and y components and

thus exclude them from the system:

$$
\begin{aligned}
E_{\nu 1} &= \frac{a_{01} + \nu_{1x} p_{1x} + \nu_{1y} p_{1y} + \nu_{1z} p_{1z}}{E_{p1}} \\
E_{\nu 1} &= \frac{b_{01} + \nu_{1x} L_{1x} + \nu_{1y} L_{1y} + \nu_{1z} L_{1z}}{E_{L1}}
\end{aligned}
\tag{7.21}
$$

These two result in:

$$
\nu_{1z} = \alpha + \beta \nu_{1x} + \gamma \nu_{1y} \tag{7.22}
$$

where

$$
\begin{aligned}
\alpha &= \left(\frac{p_{1z}}{E_{p1}} - \frac{L_{1z}}{E_{L1}} \right)^{-1} \left(\frac{b_{01}^2}{E_{L1}} - \frac{a_{01}}{E_{p1}} \right) \\
\beta &= \left(\frac{p_{1z}}{E_{p1}} - \frac{L_{1z}}{E_{L1}} \right)^{-1} \left(\frac{L_{1x}}{E_{L_1}} - \frac{p_{1x}}{E_{p1}} \right) \\
\gamma &= \left(\frac{p_{1z}}{E_{p1}} - \frac{L_{1z}}{E_{L1}} \right)^{-1} \left(\frac{L_{1y}}{E_{L1}} - \frac{p_{1y}}{E_{p1}} \right)
\end{aligned}
\tag{7.23}
$$

By making the $1 \rightarrow 2$ index substitution one gets corresponding expression for ν_{2z}. By introducing the notation:

$$
\begin{aligned}
A &= \frac{b_{01}^2 + \alpha L_{1z}}{E_{L1}} \\
B &= \frac{L_{1x} + \beta L_{1z}}{E_{L1}} \\
C &= \frac{L_{1y} + \gamma L_{1z}}{E_{L1}}
\end{aligned}
\tag{7.24}
$$

the original first four equations in (7.18) transform into two equations of the form:

$$
\begin{aligned}
(1 + \beta^2 - B^2)\nu_{1x}^2 + (1 + \gamma^2 - C^2)\nu_{1y}^2 + 2(\beta\gamma - BC)\nu_{1x}\nu_{1y} + \\
2(\alpha\beta - AB)\nu_{1x} + 2(\alpha\gamma - AC)\nu_{1y} + (\alpha^2 - A^2) = 0
\end{aligned}
\tag{7.25}
$$

or in yet another notation:

$$C_{1x}\nu_{1x}^2 + C_{1y}\nu_{1y}^2 + 2C_{1xy}\nu_{1x}\nu_{1y} + 2D_{1x}\nu_{1x} + 2D_{1y}\nu_{1y} + G_1 = 0 \tag{7.26}$$

Now using two remaining equations from (7.18), we substitute ν_{1x} through ν_{2x} and ν_{2y} through ν_{1y} and arrive at the following system:

$$\begin{aligned} a_1\nu_{2x}^2 + a_2\nu_{2x}\nu_{1y} + a_3\nu_{1y}^2 + a_4\nu_{2x} + a_5\nu_{1y} + a_6 = 0 \\ b_1\nu_{2x}^2 + b_2\nu_{2x}\nu_{1y} + b_3\nu_{1y}^2 + b_4\nu_{2x} + b_5\nu_{1y} + b_6 = 0 \end{aligned} \tag{7.27}$$

with the substitutions given by: $\nu_{1x} = -K_x - \nu_{2x}$ and $\nu_{2y} = -K_y - \nu_{1y}$ and

$$\begin{aligned} K_x &= (L_{2x} + p_{2x} + L_{1x} + p_{1x}) \qquad (-q_x) \\ K_y &= (L_{2y} + p_{2y} + L_{1y} + p_{1y}) \qquad (-q_y) \end{aligned} \tag{7.28}$$

The q_x and q_y terms in (7.28) are optional and can be included if the initial system transverse momentum is non-zero. This refinement will not affect the neutrino solutions themselves, the only adjustment that needs to be made in this case is in the aforementioned definitions of K_x and K_y. Coefficients in the bi-quadratic system of equations (7.27) are given by:

	first equation	second equation
ν_{2x}^2	C_{1x}	C_{2x}
$\nu_{2x}\nu_{1y}$	$-2C_{1xy}$	$-2C_{2xy}$
ν_{1y}^2	C_{1y}	C_{2y}
ν_{2x}	$2C_{1x}K_x - 2D_{1x}$	$2D_{2x} - 2C_{2xy}K_y$
ν_{1y}	$2D_{1y} - 2C_{1xy}K_x$	$2C_{2y}K_y - 2D_{2y}$
const	$C_{1x}K_x^2 - 2D_{1x}K_x + G_1$	$C_{2y}K_y^2 - 2D_{2y}K_y + G_2$

(7.29)

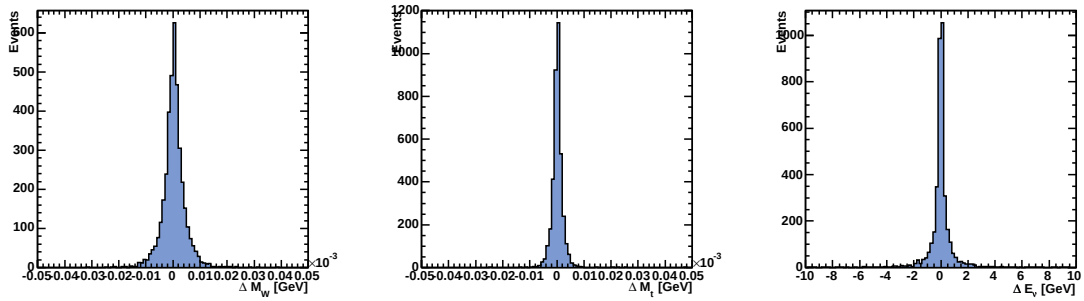

Figure 7.1: Residual in M_W, M_t and E_ν for numerical solutions to the equations required for a change of variables.

The two coupled equations are converted to a single fourth order polynomial which can be rapidly solved using numerical techniques. We employ the Sturm Sequence technique; Figure 7.1 demonstrates the accuracy of the solutions for parton-level quantities. Alternative analytical solutions can be found in Appendix D.

Note that it is possible for a forth order polynomial to have zero, two or four solutions. Multiple solutions are naturally summed over as our method requires. In the case where a particular set of observables and parton level quantities does not have any solutions, the integrand is zero. This does not constitute as issue, however, because the integration is performed over the entire parton-level phase space. The integrand may have zero value in a certain region of phase space, but the integral almost certainly will gain non-zero contribution from other regions.

7.1.4 Jacobian factor

Jacobian factor that appears from integrations over neutrino momenta components has the form:

$$J = \left| \frac{\partial f_i}{\partial \nu_{(1,2)(x,y,z)}} \right| \tag{7.30}$$

The f_i are the functions of neutrino momenta that occur inside δ-functions:

$$
\begin{aligned}
f_1 &= ((L_1 + \nu_1 + p_1)_x + (L_2 + \nu_2 + p_2)_x) \\
f_2 &= ((L_1 + \nu_1 + p_1)_y + (L_2 + \nu_2 + p_2)_y) \\
f_3 &= \left((L_1 + \nu_1 + p_1)^2 - M_{t_1}^2\right) \\
f_4 &= \left((L_2 + \nu_2 + p_2)^2 - M_{t_2}^2\right) \\
f_5 &= \left((L_1 + \nu_1)^2 - M_{W_1}^2\right) \\
f_6 &= \left((L_2 + \nu_2)^2 - M_{W_2}^2\right)
\end{aligned}
\tag{7.31}
$$

The determinant has the form:

$$
\begin{vmatrix}
1 & 0 & J_{3x} & 0 & J_{5x} & 0 \\
0 & 1 & J_{3y} & 0 & J_{5y} & 0 \\
0 & 0 & J_{3z} & 0 & J_{5z} & 0 \\
1 & 0 & 0 & J_{4x} & 0 & J_{6x} \\
0 & 1 & 0 & J_{4y} & 0 & J_{6y} \\
0 & 0 & 0 & J_{4z} & 0 & J_{6z}
\end{vmatrix}
$$

that evaluates to:

$$
\begin{aligned}
J = |&J_{3z}J_{4z}J_{5y}J_{6x} - J_{3y}J_{4z}J_{5z}J_{6x} - J_{3z}J_{4z}J_{5x}J_{6y} + \\
&+ J_{3x}J_{4z}J_{5z}J_{6y} + J_{3z}J_{4y}J_{5x}J_{6z} - J_{3z}J_{4x}J_{5y}J_{6z} + \\
&+ J_{3y}J_{4x}J_{5z}J_{6z} - J_{3x}J_{4y}J_{5z}J_{6z}|
\end{aligned}
\tag{7.32}
$$

with:

$$
\begin{aligned}
J_{3x} &= \frac{\partial f_3}{\partial \nu_{1x}} = \frac{2(L_1^0 + p_1^0)\nu_{1x}}{\sqrt{\nu_{1x}^2 + \nu_{1y}^2 + \nu_{1z}^2}} - 2(L_{1x} + p_{1x}) \\
J_{3y} &= \frac{\partial f_3}{\partial \nu_{1y}} = \frac{2(L_1^0 + p_1^0)\nu_{1y}}{\sqrt{\nu_{1x}^2 + \nu_{1y}^2 + \nu_{1z}^2}} - 2(L_{1y} + p_{1y}) \\
J_{3z} &= \frac{\partial f_3}{\partial \nu_{1z}} = \frac{2(L_1^0 + p_1^0)\nu_{1z}}{\sqrt{\nu_{1x}^2 + \nu_{1y}^2 + \nu_{1z}^2}} - 2(L_{1z} + p_{1z}) \\
J_{4x} &= \frac{\partial f_4}{\partial \nu_{2x}} = \frac{2(L_2^0 + p_2^0)\nu_{2x}}{\sqrt{\nu_{2x}^2 + \nu_{2y}^2 + \nu_{2z}^2}} - 2(L_{2x} + p_{2x}) \\
J_{4y} &= \frac{\partial f_4}{\partial \nu_{2y}} = \frac{2(L_2^0 + p_2^0)\nu_{2y}}{\sqrt{\nu_{2x}^2 + \nu_{2y}^2 + \nu_{2z}^2}} - 2(L_{2y} + p_{2y}) \\
J_{4z} &= \frac{\partial f_4}{\partial \nu_{2z}} = \frac{2(L_2^0 + p_2^0)\nu_{2z}}{\sqrt{\nu_{2x}^2 + \nu_{2y}^2 + \nu_{2z}^2}} - 2(L_{2z} + p_{2z}) \\
J_{5x} &= \frac{\partial f_5}{\partial \nu_{1x}} = \frac{2(L_1^0 \nu_{1x})}{\sqrt{\nu_{1x}^2 + \nu_{1y}^2 + \nu_{1z}^2}} - 2L_{1x} \\
J_{5y} &= \frac{\partial f_5}{\partial \nu_{1y}} = \frac{2(L_1^0 \nu_{1y})}{\sqrt{\nu_{1x}^2 + \nu_{1y}^2 + \nu_{1z}^2}} - 2L_{1y} \\
J_{5z} &= \frac{\partial f_5}{\partial \nu_{1z}} = \frac{2(L_1^0 \nu_{1z})}{\sqrt{\nu_{1x}^2 + \nu_{1y}^2 + \nu_{1z}^2}} - 2L_{1z} \\
J_{6x} &= \frac{\partial f_6}{\partial \nu_{2x}} = \frac{2(L_2^0 \nu_{2x})}{\sqrt{\nu_{2x}^2 + \nu_{2y}^2 + \nu_{2z}^2}} - 2L_{2x} \\
J_{6y} &= \frac{\partial f_6}{\partial \nu_{2y}} = \frac{2(L_2^0 \nu_{2y})}{\sqrt{\nu_{2x}^2 + \nu_{2y}^2 + \nu_{2z}^2}} - 2L_{2y} \\
J_{6z} &= \frac{\partial f_6}{\partial \nu_{2z}} = \frac{2(L_2^0 \nu_{2z})}{\sqrt{\nu_{2x}^2 + \nu_{2y}^2 + \nu_{2z}^2}} - 2L_{2z}
\end{aligned}
\tag{7.33}
$$

7.1.5 Integral: final

After neutrino solutions are found and the δ-function induced Jacobian is evaluated the expression for the unnormalized probability density takes the following form:

$$\frac{d\sigma}{d\mathbf{x}} = \left(\frac{1}{(2\pi)^3}\right)^6 (2\pi)^2 \iint \sum_{i,j} \frac{|M|^2}{2E^2_{\texttt{beam}}} \frac{p^2_{1R}\sin\theta_{p_1} dp_{1R}}{2E_{p_1}} \frac{p^2_{2R}\sin\theta_{p_2} dp_{2R}}{2E_{p_2}} \frac{J^{-1}}{E_{\nu_1}E_{\nu_2}E_{L_1}E_{L_2}}$$
$$f^i_{\texttt{PDF}}(\frac{q^z_1}{E_{\texttt{beam}}}, Q^2)\ f^j_{\texttt{PDF}}(\frac{q^z_2}{E_{\texttt{beam}}}, Q^2)\ f_{\texttt{flux}}(q^z_1, q^z_2)\ f_{\texttt{utf}}$$
$$f(E_{p_1}, E_{j_1})\ f(E_{p_2}, E_{j_2})\ M_{t_1}\ M_{t_2}\ M_{W_1}\ M_{W_2}\ dM_{t_1}\ dM_{t_2}\ dM_{W_1}\ dM_{W_2} \tag{7.34}$$

In order to obtain the differential cross-section the 6-dimensional integral (7.34) over b-parton momenta and four invariant masses should be evaluated. The sum is performed over the incoming parton flavors. The additional sum that needs to be done is over two possible jet assignments[11].

7.1.6 Observed missing transverse energy — another constraint

Additional information about the event is available from the observed missing transverse energy $\not{E}_T$. In order to include it in the analysis we need the probability distribution for observing certain values of the x and y components of the missing transverse energy given the parton quantities in the event *and* the measured jet energies. From this we construct a "pseudo"-transfer function that depends on the neutrino momenta, b-quark momenta and measured jet energies. If the intitial transverse momentum of the parton system, i.e. prior to the interaction that produced $t\bar{t}$

[11]For each event it is not known which jet corresponds to which lepton. In our case we have only two possibilities. If the jet assignment is considered a discrete variable that is not measured, the total probability is the sum over two possible values.

pair and prior to intitial state radiation, is q_x, q_y, then we have the relationship:

$$\begin{aligned} q^x &= E_T^x + \sum \nu^x - \sum p_j^x + \sum p^x \\ q^y &= E_T^y + \sum \nu^y - \sum p_j^y + \sum p^y \end{aligned} \tag{7.35}$$

where $E_T^{x,y}$ denotes components of total "detectable" transverse momenta, that is the sum of observed energy from the jets associated with the b quarks, the lepton energies, and any other energy observed in the calorimeter whether or not it comes from the $t\bar{t}$ system, $\nu^{x,y}$ — the components of "undetectable" transverse momenta from the neutrinos, $p_j^{x,y}$ are the jet momenta and $p^{x,y}$ are the momenta of the partons that produce the jets. The components of $\not{E}_T$ in an ideal detector are simply $-E_T^x$ and $-E_T^y$. Hence, we have:

$$\begin{aligned} \not{E}_T{}^x &= \sum \nu^x + \sum (p^x - p_j^x) - q^x \\ \not{E}_T{}^y &= \sum \nu^y + \sum (p^y - p_j^y) - q^y \end{aligned} \tag{7.36}$$

Mis-measurement of the jet energies is accounted for in the jet energy transfer function. However, Equation 7.36 gives an additional constraint between the observed missing transverse energy and the neutrino momenta, which will be integrated over.

The q_x and q_y components are unknown and thus will be integrated over as well. They are not arbitrary and indeed are expected to be small. We already used this implicitly when we assumed that $q_{x,y} \ll q_z$. When the integration over invariant masses of intermediate W-s and t-s is performed, the solutions for corresponding $q_{x,y}$ vary from likely to improbable. To quantify this effect and restrict $q_{x,y}$ to have "reasonable" values we introduce "prior" $p(q_x, q_y|I)$ that summarizes our knowledge about the momentum of the initial parton system. Naively it can be modeled as Gaussian-distributed deviation from $(0, 0)$ with appropriately chosen $\sigma_{q_{x,y}}$. Our expression for

the matrix element multiplied by the appropriate transfer functions and PDF-s gets an additional factor — initial transverse momentum prior.

As stated above, the transfer function for missing transverse energy characterizes the probability to observe a particular value of missing transverse energy given the expected value according to Equation (7.36), $p(\not{E}_{Tm}{}^x, \not{E}_{Tm}{}^y \mid \not{E}_T{}^x, \not{E}_T{}^y)$.Naively modeling this conditional probability density as a Gaussian[12], we effectively de-weight the angular and invariant mass solutions tried by the integration routine that correspond to the true missing transverse energy which differs from the measured by a large amount. Thus our desired transfer function will encode the resolution in the unclustered energy, or, which is equivalent, the relation between "ideal" $\not{E}_T$ of Equation (7.36) and the "real" $\not{E}_T$, measured in the detector.

The two functions[13], introduced above, are the prior for transverse momentum of the system distribution and the likelihood function for the measured missing transverse energy, conditional on the "true" missing transverse energy. In order to obtain the posterior probability (or differential cross-section) it is necessary to integrate over the variables of ignorance q_x and q_y. In the extreme case of a very narrow prior, these conditions effectively degenerate into constraints, removing two of the integrations.

[12]in our current analysis we use the following parametrization:

$$f_{\mathtt{UTF}} = \frac{1}{\sqrt{2\pi}\sigma} \exp\left(-\frac{(\not{E}_{Tm}{}^x - \not{E}_T{}^x)^2}{\sigma^2}\right) \frac{1}{\sqrt{2\pi}\sigma} \exp\left(-\frac{(\not{E}_{Tm}{}^y - \not{E}_T{}^y)^2}{\sigma^2}\right) \tag{7.37}$$

with $\sigma = 12.0$ GeV.

[13]It should be noted that although the effects of the introduction of these functions may appear to account for ISR and FSR, it does not, at least in a strict sense. Although one may speculate that ISR may be considered roughly equivalent to giving the system of initial partons a recoil and FSR as giving a contribution to mis-measurement of $\not{E}_T$, the reasoning behind such "intuitive" picture is not straightforward. First of all, the matrix element used in the calculation does not account for either. Second, the FSR kicks in *before* the measurement of final state particle momenta are done and thus the solutions for $q_{x,y}$ would give a momentum of $t\bar{t}$ system *after* recoil from FSR. This in turn means that the wrong momenta are used in calculation of matrix element for both final and initial state momenta. This makes our interpretation of the model as a leading order calculation with probabilistic marginalization over unmeasured quantities the preferred interpretation, i.e. the effects of ISF and FSR are not fully accounted for by any of the transfer functions.

7.2 Tests of the signal differential cross-section

The calculation of the differential cross section describes our understanding of the physical process of the production of top quark pairs and subsequent top-quark decays. However, to limit computational complexity, we introduced some assumptions that simplify the model. The most important of these are

- *Jet-parton matching*: we assume that all jets come from b-quarks, rather than from initial or final state radiation.
- *Jet-parton angles*: we assume that jet angles reflect perfectly the parton angles.
- *Lepton energy*: we assume that lepton energies are perfectly measured.

It is possible to measure the effect of these assumptions by testing our ability to extract the top mass in different sub-classes of events in which these simplifying assumptions are broken to increasing degrees.

7.2.1 Parton-level tests

We begin with simulated $p\bar{p} \to t\bar{t}$ events generated with Pythia in which all of the parton-level information from the hard scattering and subsequent decay is known. Evaluating the matrix element for these events as a function of top-quark pole mass, see Figure 7.2, we see the sharp peaks which correspond to the invariant mass of each of the top quarks in the event. Note that with perfect parton-level information, we do not need to perform any integration.

Individual events are not very instructive; we wish to probe whether the calculation contains a bias, and whether the error can be accurately estimated from the shape of the probability distribution derived from a sample of events. We form pseudo-experiments by constructing the joint probability of ten events, see Figure 7.3.

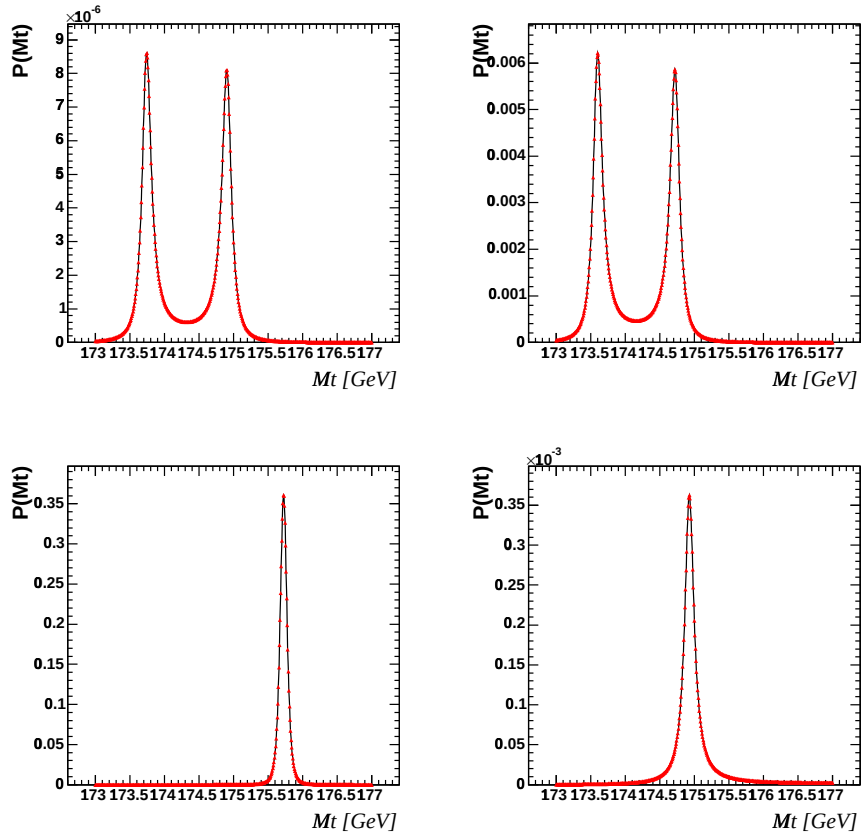

Figure 7.2: $|M|^2$ as a function of pole mass for four parton-level top quark pair events with $M_t = 175$ GeV.

Choosing the most probable value as the measured mass and extracting the error from the shape of the probability distribution should, to the extent that our model is accurate, give us an unbiased measure of the top mass and an accurate error estimate.

7.2.2 Smeared parton-level tests

To probe the integration machinery and numerical kinematics solutions, we use a more realistic test. First, we smear the energy of the b-quarks with Gaussians (where $\sigma_E = 0.1E_{parton}$) to produce simple jets. In addition, we disregard the b-quark momentum and all of the information from the ν and $\bar{\nu}$. This simulates the amount of information

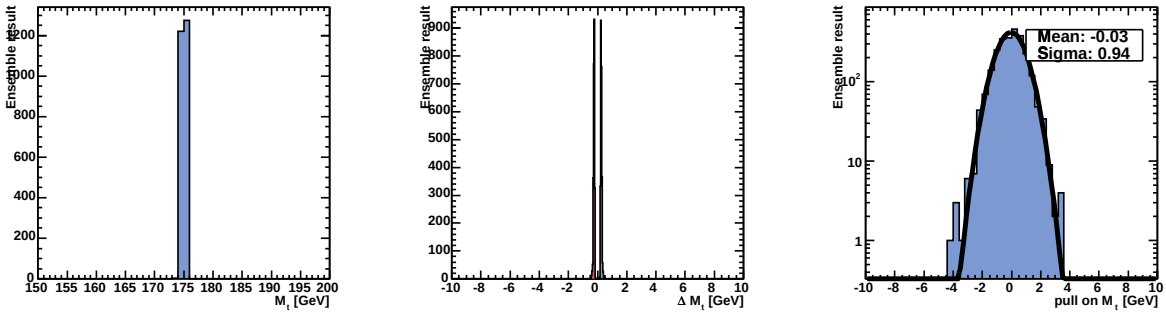

Figure 7.3: An ensemble of pseudo-experiments using perfect information for parton-level top quark pair events with $M_t = 175$ GeV. The extracted mass is the peak of the joint probability. As these shapes are not necessarily Gaussian, the positive and negative errors $\Delta M_t^{\pm}$ are defined such that $\int_{M_t-\Delta M_t^-}^{M_t+\Delta M_t^+} P(x|M_t) = 0.68$.

available in actual events, though the events are significantly cleaner and obey all of the assumptions listed above.

Figure 7.4 shows four example event probabilities. Figure 7.5 shows that the extracted measurement from pseudo-experiments of ten events each is unbiased and that the error is accurate.

The analysis machinery can be applied next to a still more realistic set of events in which the parton momenta are smeared using the shape of the extracted transfer functions. These events match in their nature the likelihood calculation that is used by the method. None of the assumptions are explicitly violated and all the components of the evaluation machinery are being tested. The results suggest that the machinery is working as expected and when applied to a set of events that hold all the simplifying assumptions true a reliable estimate of statistical error is obtained, Table 7.1.

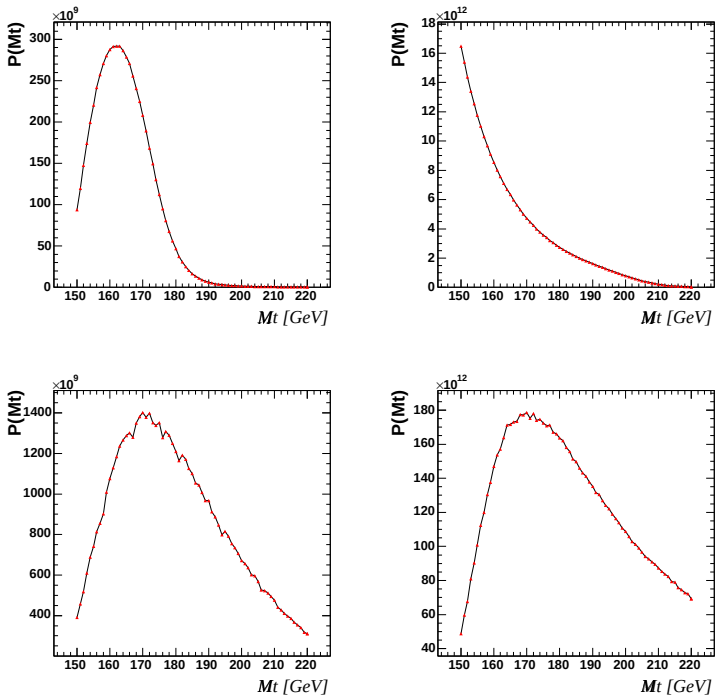

Figure 7.4: Posterior probability as a function of pole mass for four parton-level top quark pair events where the quark energies are smeared by 10% with $M_t = 175$ GeV and the four-momentum information of two neutrinos is ignored.

Sample	Jets	Leptons	Pull Width
Parton	Gaussian smeared	Perfect	1.04
Parton	TF smeared	Perfect	0.98

Table 7.1: Demonstration of well-behaved pull distributions in pseudo-experiments drawn from events which obey assumptions regarding jet and lepton resolution.

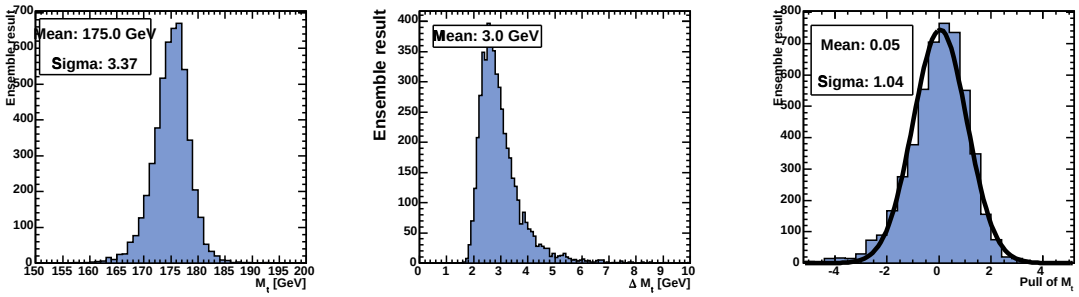

Figure 7.5: Distributions of reconstructed top-quark mass, predicted error on mass determination and pull in an ensemble of pseudo-experiments of 10 parton-level top quark pair events where the quark energies are smeared by 10% with $M_t = 175$ GeV

7.2.3 Tests with simulated events

Events which are measured by the CDF detector are far less ideal than smeared parton-level events. Occasionally, the direction of the jet deviates from the direction of the b-quark it originated from. While the lepton energy resolution is very good, especially for electrons, it is not perfect. In some cases, one of the two leading jets does not originate from a b-quark, but from radiation[14]. The sample also contains events with secondary leptons from $W \rightarrow \tau$ decays. We isolate and explore these effects in that order.

Jet Angle Resolution

In formulation of the differential cross-section, the correspondence between jet and parton angles are described by a δ-function. While the angle resolution is excellent in comparison to the energy resolution, it is not perfect. Figure 7.6 shows the angular distance between the parton and the reconstructed jet. This distribution has two features: the width at small ΔR shows the angular resolution for matched jets and partons while the high tail and the overflow bin at $\Delta R = 0.7$ represent jets which are not well matched to b-quarks.

In order to isolate the effect of the jet-angle resolution, a subset of events from a fully simulated sample with $M_t = 178$ GeV is examined. In this subset the effects of lepton energy resolution are removed by $P_T^{hepg} - P_T^{reco} < 2$ GeV requirement placed on lepton momenta, where P_T^{hepg} stands for generator-level, or "true", value of transverse momentum, while P_T^{reco} is the value of transverse momentum reconstructed from fully simulated detector response. The effects of incorrect jet-parton matching are to a large extent taken care of by $\Delta R < 0.4$ condition. Pseudo-experiments using this subset of events have a pull width of ≈ 1.1, suggesting that the jet-angle resolution contributes

[14]most frequently from initial state gluon radiation

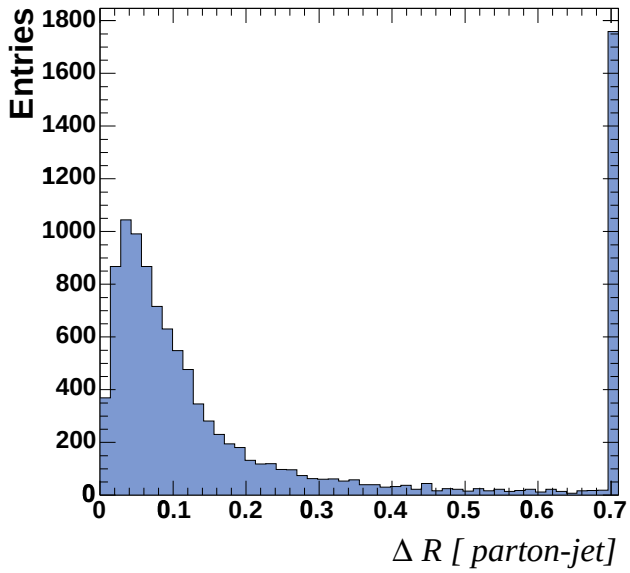

Figure 7.6: Angular matching between jets and b-quarks from top decay. The width of distribution demonstrates the angular resolution. Overflow bin at $\Delta R = 0.7$ illustrates the number of jets with no corresponding b-quark.

$\approx 10\%$ to the pull width.

When the pseudo-experiments with progressively more strict requirements on ΔR are performed the pull width decreases smoothly from ≈ 1.1 to ≈ 1.0, see Figure 7.7.

In order to further confirm the magnitude of this effect, imperfect jet-angle resolution is simulated via smearing parton-level events, see Figure 7.8. Pseudo-experiments drawn from these events show a $\approx 10\%$ increase in pull width, Table 7.2.

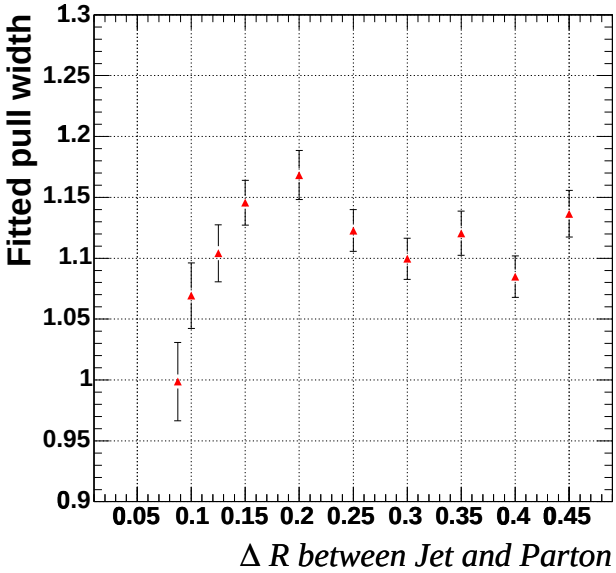

Figure 7.7: Variation of pull-width from pseudo-experiments as a function of the angular matching requirement between jets and partons.

Sample	Jets	Jet Angles	Leptons	Pull Width
FullSim	Reco	$\Delta R < 0.1$	$\Delta P_T < 2$ GeV	1.00
FullSim	Reco	$\Delta R < 0.4$	$\Delta P_T < 2$ GeV	1.08
Parton	TF smeared	Perfect	Perfect	0.98
Parton	TF smeared	Smeared	Perfect	1.07

Table 7.2: Pull width affected by the jet angle resolution, in fully reconstructed events and in artificially smeared parton-level events.

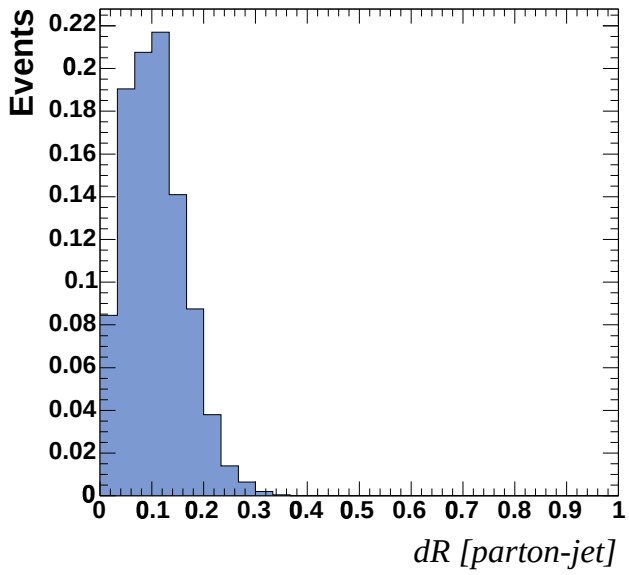

Figure 7.8: Angular resolution of jets after artificial smearing of the parton-level events.

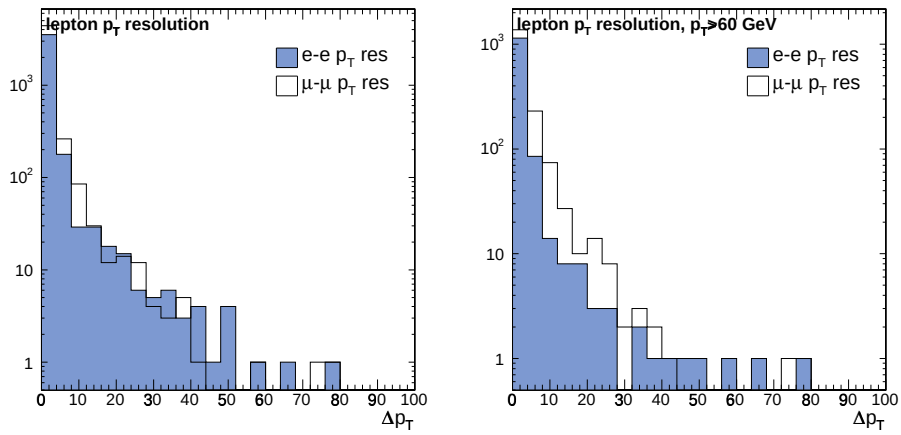

Figure 7.9: Left, $\Delta P_T \equiv P_T^{hepg} - P_T^{reco}$ for events with $20 < P_T < 60$ GeV. Right, ΔP_T for events with $P_T > 60$ GeV.

Lepton Resolution

Leptons are well measured by CDF, and the approximation that their energy resolution is ideal is quite reasonable. However, electrons and muons four-momenta are measured differently. While the energies of electrons at high E_T are measured by the calorimeter with a decent precision, the momenta of muons are measured by the central tracker, whose resolution at large P_T is distinctly reduced. Figure 7.9 shows the lepton P_T resolution at low and high P_T.

In order to isolate the effect of the imperfect momentum resolution, pseudo-experiments of fully simulated events with only electrons or only muons were constructed. Table 7.3 shows that events with muons have a $\approx 10\%$ larger pull width than events with electrons over a variety of jet requirements.

The magnitude of the effect can be confirmed by smearing lepton energies in parton-level events. Based on studies presented in [24], a two-level Gaussian smearing of the P_T^{-1} is done; the results are shown in Figure 7.10. Table 7.4 shows the pull width of pseudo-experiments drawn from these events, which confirms that lepton energy resolution can contribute $\approx 10\%$ to the pull width.

Sample	Jets	Leptons	Pull Width
FullSim	$\Delta R < .4$	ee	1.10
FullSim	$\Delta R < .4$	$\mu\mu$	1.25
FullSim	All	ee	1.26
FullSim	All	$\mu\mu$	1.36
FullSim	$= 2$	ee	1.12
FullSim	$= 2$	$\mu\mu$	1.28
FullSim	$= 2, \Delta R < .4$	$\geq 1\tau$	1.20

Table 7.3: Effect of muon momentum resolution on pull widths, for a variety of jet requirements. The effect of taus is also described. The "jets = 2" denotes the selection where only the events with exactly two jets are accepted.

Sample	Jets	Leptons	Pull Width	
Parton	TF-smeared	Perfect	Perfect	0.98
Parton	TF-smeared	Perfect	Smeared (less)	1.01
Parton	TF-smeared	Perfect	Smeared (more)	1.10

Table 7.4: Effect on the pull width of smearing lepton energies. The parameters of "less" and "more" smearing are shown in Figure 7.10

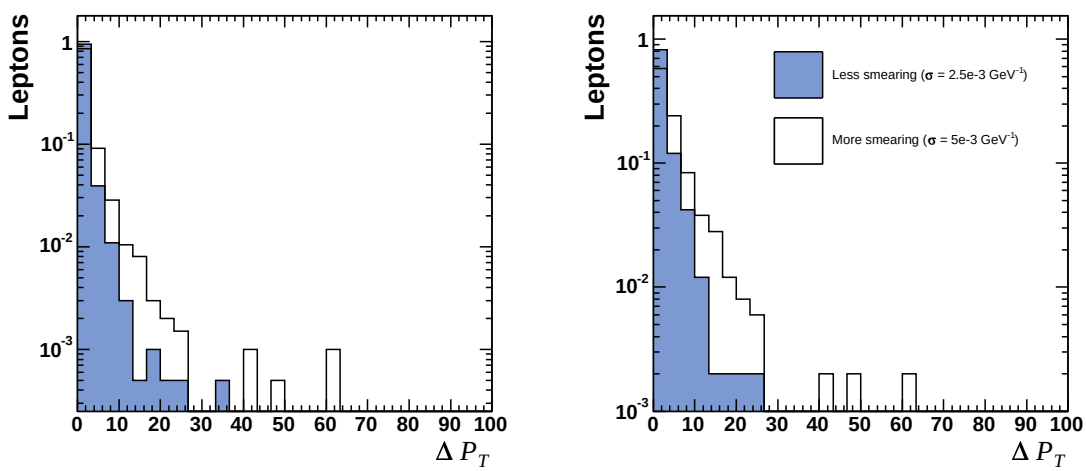

Figure 7.10: Lepton momentum are smeared by introducing a random term to the inverse P_T according to a Gaussian. Left, ΔP_T for events with $P_T < 60$ GeV. Right, ΔP_T for events with $P_T > 60$ GeV.

Sample	Jets	Leptons	Pull Width
FullSim	All	ee	1.26
FullSim	$\Delta R < 0.4$	ee	1.10
FullSim	All	$\mu\mu$	1.36
FullSim	$\Delta R < 0.4$	$\mu\mu$	1.25
FullSim	All	no τ	1.34
FullSim	$\Delta R < 0.4$	no τ	1.22
FullSim	All	All	1.42
FullSim	$\Delta R < 0.4$	All	1.18

Table 7.5: Increase in pull width due to jets which are unmatched to b-quarks. A $\approx 20\%$ effect is seen across lepton types.

Jet-Parton Assignment

As demonstrated by Figure 7.6, there is a significant population of jets which do not correspond to either b-quark from the top-antitop pair decay. This has a significant effect on the width of the pull distribution, as these events violate an important assumption and contain significantly less information about the $t\bar{t}$ event constituents than events with appropriate topologies. In order to estimate the size of the effect on the pull width a set of pseudo-experiments using only events where both jets match well to b-quarks is constructed. Table 7.5 shows that matching requirement decreases the pull width by $\approx 20\%$, and that this effect is observed for all lepton types.

The initial state radiation, or in other words a situation where radiation from incoming quark or gluon gives rise to a hard jet, is expected to be the largest source of jets that do not correspond to a b-quark from $t\bar{t}$ decay. This effect can be probed in some detail by studying the correlation between the number of jets in the reconstructed event, and the P_T of the $t\bar{t}$ system, which is a measure of the total recoil against initial state radiation. Figure 7.11 demonstrates a strong correlation between these quantities, suggesting that initial state radiation is the major source of extra jets in the event.

P_T	Pull Width	2 Matched Jets
All	1.42	70%
$0 < P_T < 10$	1.27	80%
$10 < P_T < 25$	1.42	69%
$25 < P_T < 50$	1.64	49%

Table 7.6: Correlation between increased P_T of the $t\bar{t}$ system, the pull width from pseudo-experiments, and the fraction of events with 2 jets from b-quarks.

Further analysis of pseudo-experiments formed using events from different $P_T^{t\bar{t}}$ bins show a correlation between the pull width and the recoil energy, see Table 7.6. Together, these suggest that events with significant initial state radiation give rise to additional reconstructed jets, which in turn contribute to a wider pull distribution.

Summary

Introduction of the events that are not properly described by our probability expression into the pseudo-experiments leads to an increased uncertainty of the ensemble mean. There would be a corresponding increase in the ensemble variance *if the probability expression included the terms that describe these extra deviations.* In our case a proper theoretical description of the events that violate the original assumptions cannot be easily included in the model. Consequently, the statistical uncertainty as estimated from any given pseudo-experiment is essentially determined by "good" events and thus stays the same. In summary, events which are not properly described result in additional random noise in the ensemble means, while no corresponding increase in estimated statistical uncertainty is happening, which in turn results in wider pull distributions.

Small deviations of the reconstructed mass from the true mass as well as the best estimate of the statistical uncertainty can be carefully measured in the simulated events. This approach is deemed reasonable as the reasons for these effects are

well understood and cannot be easily eliminated by refining the model. We discuss calibration of the response in Chapter 9.

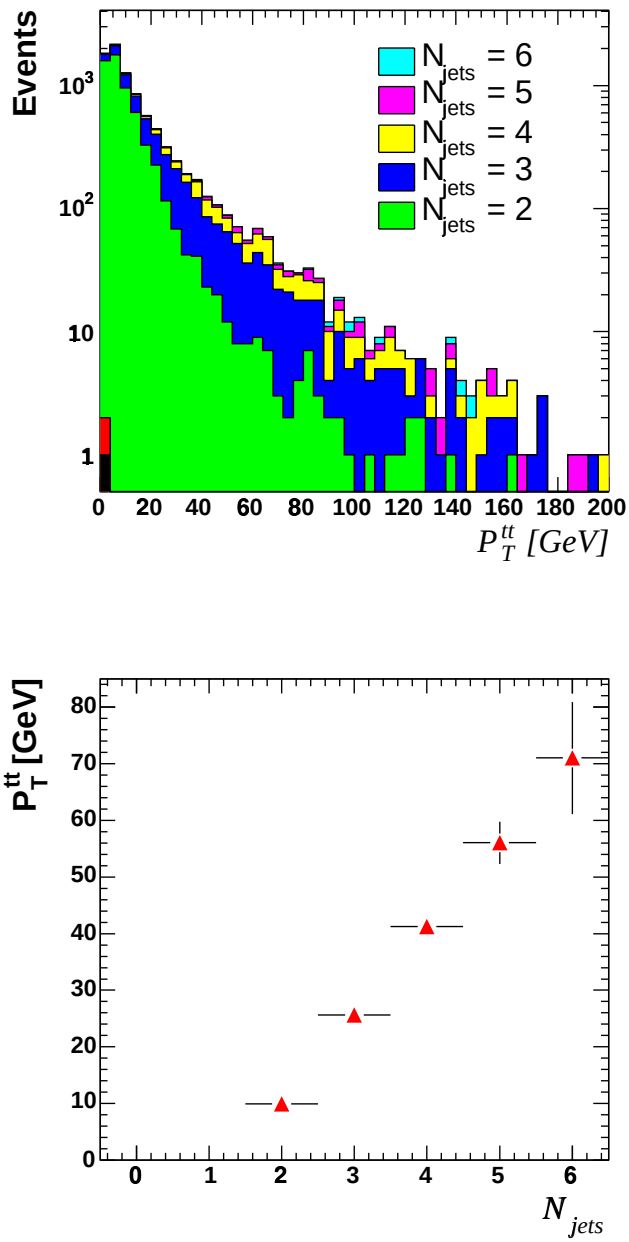

Figure 7.11: Correlation between the P_T of the $t\bar{t}$ system and the number of reconstructed jets. Top, distribution of P_T for events with varying jets. Bottom, average P_T for varying jet multiplicity.

Chapter 8

Backgrounds

While the di-lepton sample is fairly clean, it is not a pure sample. The major backgrounds are:

- Drell-Yan production with two jets (including $Z \rightarrow \tau\tau$)
- pair production of W bosons with two jets
- associated production of W and Z bosons with two jets
- production of W with three jets, where one is misreconstructed as a lepton

In order to reduce the effect of these events on the measurement of the mass, calculations of the differential cross-section for the Z+2jet process, the WW+2jet process and the $W + 3jet$ processes were performed. Section 8.1 discusses the calculation of the matrix element using the ALPGEN [25] routine, and the subsequent sections describe the procedure of integration of the matrix element over the phase space.

8.1 Matrix Element calculation with Alpgen

Background processes are different from the signal process in an important way.[1] While the signal process can be well described using a small number of diagrams (*e.g.* top quark pair production), the backgrounds to these events with hard jets typically require more than an order of magnitude more diagrams to accurately describe them. Furthermore, there is no closed-form expression for the QCD processes which dominate this production.

The matrix-element calculation machinery was extracted from a well-known Monte Carlo event generator which employs effective approximations to estimate the matrix element. There exists a wide variety of Monte Carlo event generators to choose from. Recently, generators such as CompHEP and Madgraph have provided generation based directly on the explicit construction and evaluation of the Feynman diagrams. These generators offer a transparent and clean interface to the matrix element. However, in the case of a final state with more than a single jet, the number of diagrams very quickly becomes unwieldy and the calculation very slow. For this reason, to use the matrix element evaluation of the ALPGEN [25] generator has been chosen as it offers the following advantages:

- The ALPHA algorithm, presented in [26–28], avoids explicit generation and evaluation of every diagram
- Large, well-studied samples of generated events were available at the time of this writing and formed the basis of understanding of the experimentally collected data.

In the next sections, the prescription that has been developed for the evaluation of the matrix element by adapting a portion of the ALPGEN program is discussed in

[1] we acknowledge Daniel Whiteson for substantial constributions to this section

some detail.

8.2 Interface to Alpgen

The matrix element calculated by ALPGEN is a function of the final and initial state particles spin, color, flavor as well as momentum. To evaluate the differential cross section for a single event, a sum over all possible configurations of spins, colors and flavors must be performed.

As the number of final state particles increases, the number of spin and color configurations grows quickly. A rigorous sum over each of the possibilities is impractical and unnecessary, however, as it appears to be possible to approximate the total sum with a statistical sampling. Figure 8.1 shows the distribution of $\Delta \ln |M|^2$ in generated events using sums of a specific number of terms. It is clear that the matrix element calculation is sensitive to the configuration and that it converges fairly rapidly.

Spin and color configurations are being sampled until the sum has converged, satisfying the criteria

$$\frac{RMS(|M|^2)}{Mean(|M|^2)\sqrt{N}} < \epsilon$$

where ϵ is the convergence tolerance, set to $\epsilon = 0.25$ for these calculations[2].

The calculation of the matrix element is well behaved. As an example, Figure 8.2 shows the variation of $|M_{Zjj}|^2$ with the di-lepton invariant mass. It shows the expected strong peak at $M_{ll} = M_Z$. Another illustration is provided by Figure 8.3 that shows the separation between Zjj and $t\bar{t}$ samples that is made possible by the above

[2]the form of the stopping criteria and the ϵ value were chosen such as to provide the best separation of signal and background at parton level while maintaining reasonable computation load

evaluation.

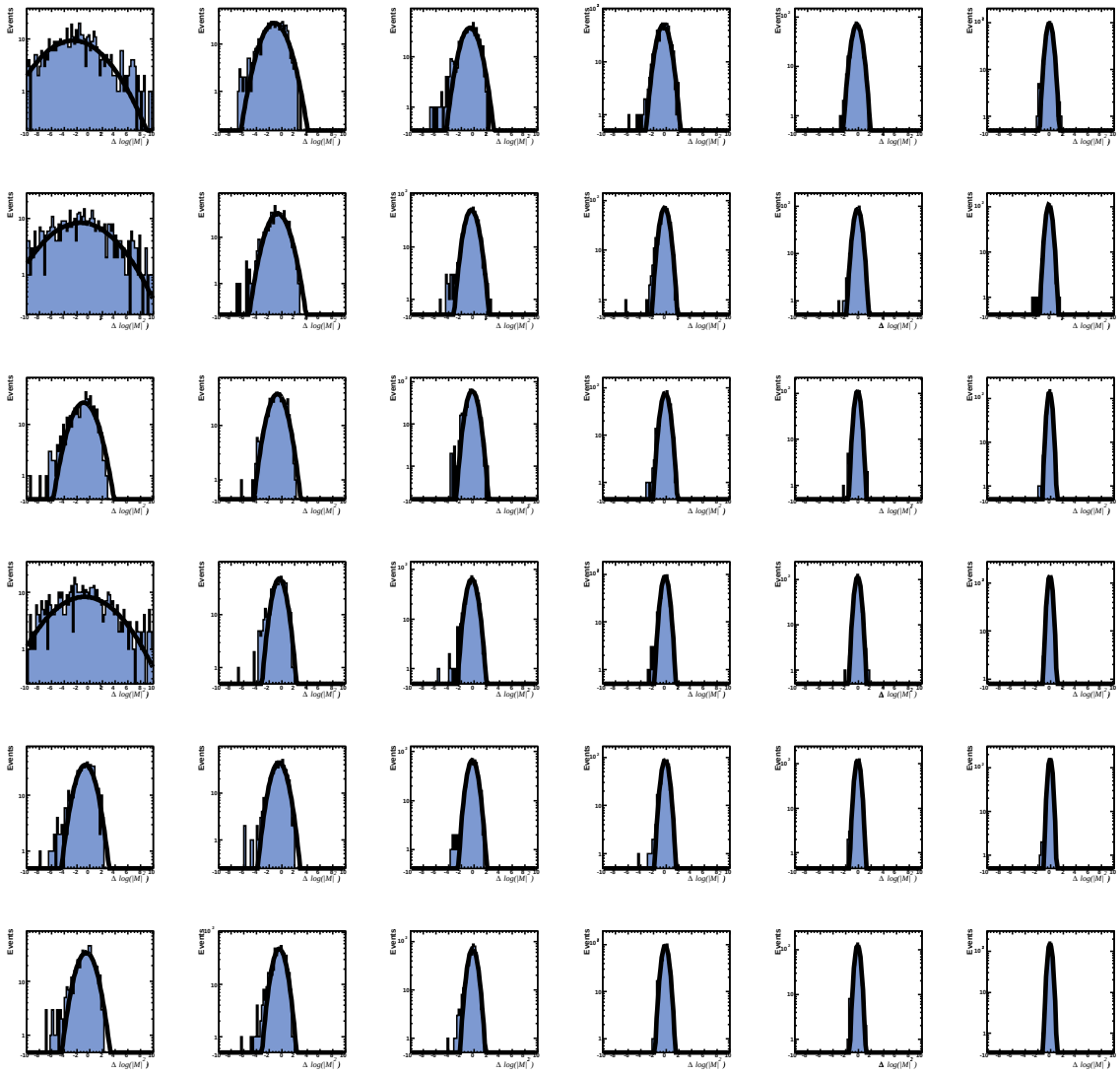

Figure 8.1: Variation in $\log(|M|^2)$ with increasing number of terms in the spin and color sum. From top, moving downwards, the number of spin terms sampled increases by powers of 2 from 1 to 32. From left, moving right, the number of color terms sampled increases by powers of 2 from 1 to 32. The x axis range is from -10 to $+10$ in $\Delta \ln |M|^2$.

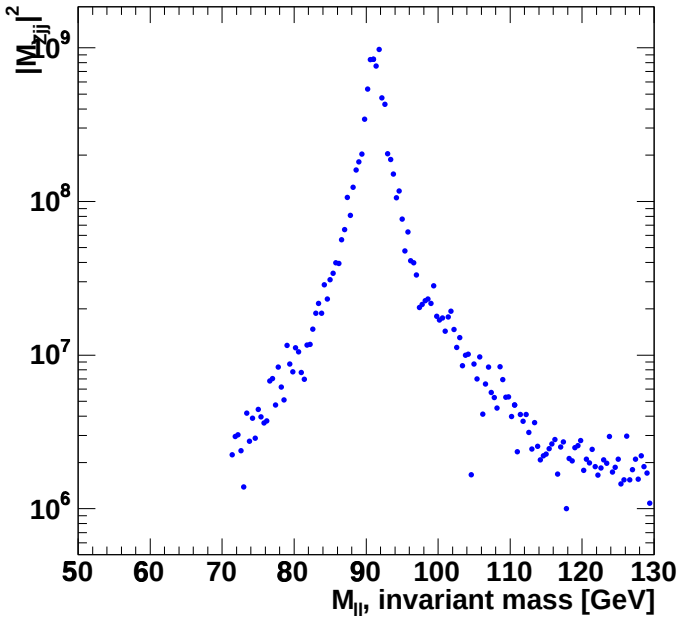

Figure 8.2: Variation of the squared matrix element for $pp \to Z(\to ll) + 2jets$ as a function of the leptonic pair invariant mass.

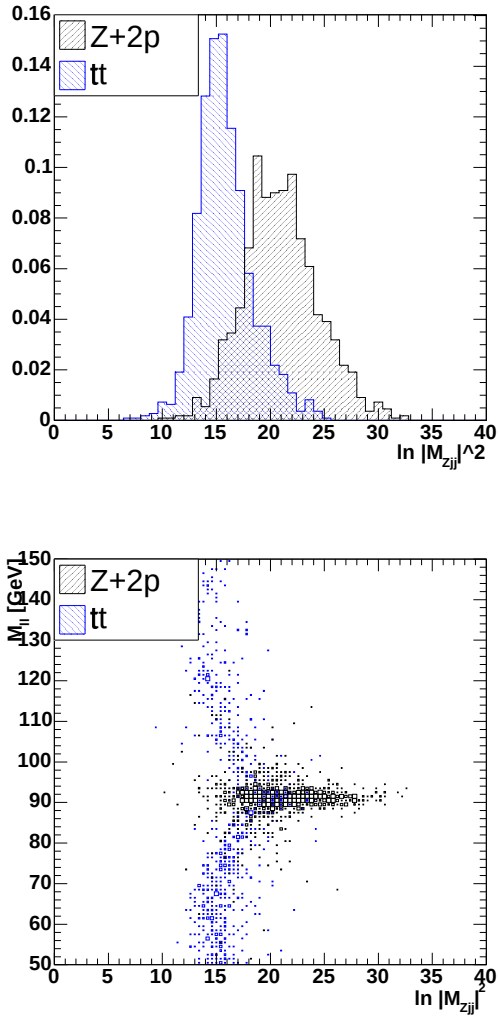

Figure 8.3: Evaluation of the squared matrix element for $pp \to Z(\to ll) + 2jets$ for parton-level $t\bar{t}$ and $Z + 2p$ events. The top plot shows a histogram of $\ln|M_{Zjj}|^2$, the bottom shows a two-dimensional histogram of $\ln|M_{Zjj}|^2$ (on x axis) versus $M_{\ell\ell}$ (on y axis).

8.3 Drell-Yan : Differential cross-section

The previous section described the evaluation of the matrix element using ALPGEN routines. This section describes the calculation of the differential cross-section for Z+2jet production, which requires integration of the matrix element over the phase space. In this case, the number of constraints from the measurement of the final state objects reduces the number of integrals to exactly zero.

We use the following notation: p_1, p_2 are the four-momenta of the final state partons which lead to creation of extra jets, L_1, L_2 are the four-momenta of the final state leptons, q_1, q_2 — the four-momenta of incoming partons. The expression for the differential cross-section of this process is of the form:

$$
\begin{aligned}
d\sigma = \sum_{a,b} \iint & \frac{1}{(2\pi)^{12}} \frac{1}{16} \frac{1}{E_{L_1} E_{L_2} E_{p_1} E_{p_2}} \\
& f(E_{p_1}, E_{j_1})\, f(E_{p_2}, E_{j_2})\, {p_{R1}}^2 \sin\theta_{p_1}\, {p_{R2}}^2 \sin\theta_{p_2} \\
& \delta(\phi_{p_1} - \phi_{j_1})\, \delta(\theta_{p_1} - \theta_{j_1})\, \delta(\phi_{p_2} - \phi_{j_2})\, \delta(\theta_{p_2} - \theta_{j_2}) \\
& dp_1^R\, d\theta_{p_1}\, d\phi_{p_1}\, dp_2^R\, d\theta_{p_2}\, d\phi_{p_2} \\
& f^a_{\mathtt{PDF}}(\frac{q_1^z}{E_{\mathtt{beam}}}, Q^2)\; f^b_{\mathtt{PDF}}(\frac{q_2^z}{E_{\mathtt{beam}}}, Q^2)\, \frac{dq_1^z\, dq_2^z}{E^2_{\mathtt{beam}}} \\
& \delta^4(q_1 + q_2 - L_1 - L_2 - p_1 - p_2) \frac{(2\pi)^4}{4(q_1^{\mathtt{cm}}\sqrt{s})} |\mathcal{M}|^2
\end{aligned}
\tag{8.1}
$$

In the above expression we set the transverse components of incoming parton momenta to zero. This simplification can be removed if necessary by the method similar to the one used in derivation of the signal differential cross-section.

Using the same collider approximation as before, without loss of generality, we assume $q_1^0 = q_1^z$ and $q_2^0 = q_2^z$. Integration over $dq_1^z\, dq_2^z$ and t and z parts of the four-dimensional δ-function result in the extra overall factor of $1/2$ and the following

substitution:

$$
\begin{aligned}
q_1^z &= \frac{1}{2}\left((L_1^z + L_2^z + p_1^z + p_2^z) + (L_1^0 + L_2^0 + p_1^0 + p_2^0)\right) \\
q_2^z &= \frac{1}{2}\left((L_1^z + L_2^z + p_1^z + p_2^z) - (L_1^0 + L_2^0 + p_1^0 + p_2^0)\right)
\end{aligned}
\tag{8.2}
$$

Evaluation of the integrals over $d^3p_1\, d^3p_2$ is performed in spherical coordinates, in order to take advantage of the angular δ-functions. After the angular integrations, all $\phi_{p_{1,2}}$ and $\theta_{p_{1,2}}$ are replaced by corresponding jet angles. Only two integrals and two δ-functions remain — $\delta(L_1^x + L_2^x + p_1^x + p_2^x)\,\delta(L_1^y + L_2^y + p_1^y + p_2^y)\, dp_1^R\, dp_2^R$. This leads to the following system of equations for radial components of the quarks:

$$
\begin{aligned}
\begin{pmatrix} (\sin\theta_{j_1}\sin\phi_{j_1}) & (\sin\theta_{j_2}\sin\phi_{j_2}) \\ (\sin\theta_{j_1}\cos\phi_{j_1}) & (\sin\theta_{j_2}\cos\phi_{j_2}) \end{pmatrix}
\begin{pmatrix} p_1^R \\ p_2^R \end{pmatrix}
&\equiv
\begin{pmatrix} a_{11} & a_{12} \\ a_{21} & a_{22} \end{pmatrix}
\begin{pmatrix} p_1^R \\ p_2^R \end{pmatrix} = \\
&= \begin{pmatrix} c_1 \\ c_2 \end{pmatrix} \equiv
\begin{pmatrix} -(L_1^x + L_2^x) & [+q^x] \\ -(L_1^y + L_2^y) & [+q^y] \end{pmatrix}
\end{aligned}
\tag{8.3}
$$

where the terms in square brackets have to be added if we allow non-zero transverse momenta of the incoming partons. As in the signal case, the expressions inside the δ-functions are some functions of the integration variables. The Jacobian factor is required. Using (7.17), we write down this factor as:

$$
\begin{aligned}
|J| &= \left|\frac{\partial f_i}{\partial x_j}\right| = \\
&= \begin{vmatrix} (\sin\theta_{j_1}\,\sin\phi_{j_1}) & (\sin\theta_{j_2}\,\sin\phi_{j_2}) \\ (\sin\theta_{j_1}\,\cos\phi_{j_1}) & (\sin\theta_{j_2}\,\cos\phi_{j_2}) \end{vmatrix} = \\
&= \sin\theta_{j_1}\,\sin\theta_{j_2}\,\sin(\phi_{j_1} - \phi_{j_2})
\end{aligned}
\tag{8.4}
$$

The entire expression for the differential cross-section:

$$
\begin{aligned}
d\sigma =& \frac{1}{(2\pi)^{12}} \frac{1}{16} \frac{1}{E_{L_1} E_{L_2} E_{p_1} E_{p_2}} f(E_{p_1}, E_{j_1}) f(E_{p_2}, E_{j_2})\, p_1^{R^2} p_2^{R^2} \sin\theta_{j_1} \sin\theta_{j_2} \\
& f^a_{\texttt{PDF}}(\frac{q_1^z}{E_{\texttt{beam}}}, Q^2) f^b_{\texttt{PDF}}(\frac{q_2^z}{E_{\texttt{beam}}}, Q^2) |J|^{-1} \frac{(2\pi)^4}{4(q_1^{\texttt{cm}}\sqrt{s})} \frac{|\mathcal{M}|^2}{2}
\end{aligned}
\tag{8.5}
$$

The flux factor $4(q_1^{\texttt{cm}}\sqrt{s})$ can be rewritten as $2|q_1^z q_2^z|$. With some trivial trigonometrical transformations:

$$
d\sigma = \frac{1}{(2\pi)^8} \frac{1}{16^2} \frac{f_{\texttt{PDF}}(\frac{q_1^z}{E_{\texttt{beam}}}, Q^2)\, f_{\texttt{PDF}}(\frac{q_2^z}{E_{\texttt{beam}}}, Q^2)}{E_{L_1} E_{L_2} E_{p_1} E_{p_2}} \frac{|\mathcal{M}|^2}{2} \frac{f(E_{p_1}, E_{j_1})\, f(E_{p_2}, E_{j_2})\, p_1^{R^2}\, p_2^{R^2}}{|q_1^z q_2^z|\,|\sin(\phi_{j_1} - \phi_{j_2})|}
\tag{8.6}
$$

and the p_1^R, p_2^R are the solutions of (8.3):

$$
p_1^R = \frac{c_1 a_{22} - c_2 a_{12}}{a_{11} a_{22} - a_{12} a_{21}} \qquad p_2^R = \frac{a_{11} c_2 - a_{21} c_1}{a_{11} a_{22} - a_{12} a_{21}}
\tag{8.7}
$$

with

$$
\begin{aligned}
& c_1 = -(L_1^x + L_2^x) \qquad [+q^x] \\
& c_2 = -(L_1^y + L_2^y) \qquad [+q^y] \\
& (a_{11} a_{22} - a_{12} a_{21}) = \sin\theta_{p_1} \sin\theta_{p_2} \sin(\phi_{p_1} - \phi_{p_2}) \\
& (c_1 a_{22} - c_2 a_{12}) = \sin\theta_{p_2} \left((L_1^y + L_2^y) \sin\phi_{p_2} - (L_1^x + L_2^x) \cos\phi_{p_2}\right) \\
& (a_{11} c_2 - a_{21} c_1) = \sin\theta_{p_1} \left((L_1^x + L_2^x) \cos\phi_{p_2} - (L_1^y + L_2^y) \sin\phi_{p_2}\right)
\end{aligned}
\tag{8.8}
$$

where, as before, the terms in square brackets should be included if non-zero incoming transverse momentum is considered.

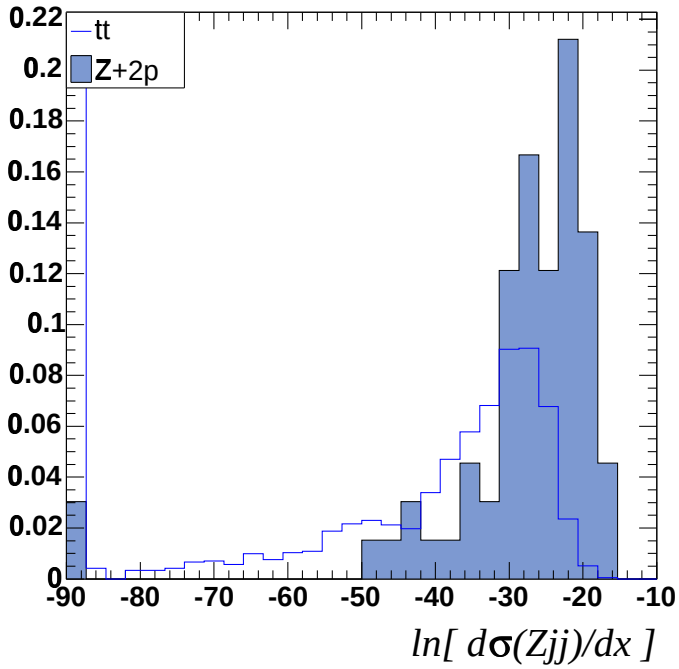

Figure 8.4: Evaluation of the Zjj probability for fully reconstructed Z and $t\bar{t}$ events, after selection is applied.

8.3.1 Performance

We evaluate the Zjj probability on events which have passed the final dilepton selections [3]. The imperfect detector response degrades our ability to separate the signal from the background events, and the event selection sculpts both sub-samples so that they are nearly identical kinematically. However, there is still visible discrimination between the Z events and the other constituents. Figure 8.4 shows the distribution of the natural logarithm of the Zjj probability densities.

[3] refer to the Chapter 4 and Appendix A for the description of the event selection

8.4 Cross section for W pair production

The calculation of the differential cross-section for WW+2 jets production requires integration of the matrix element over the phase space; it shares quite a few similarities with the $t\bar{t}$ and Drell-Yan calculations, presented in Chapter 7 and Section 8.3.[4]

An `ALPGEN` matrix element is used for the calculation, as was done for Drell-Yan. Unlike the latter, the presence of two neutrinos in the events results in six integrals to be evaluated.

8.4.1 Differential cross section and notation

We use the following notation: L_1, L_2 are the measured and ℓ_1, ℓ_2 are the parton-level four-momenta of the final state leptons, ν_1, ν_2 are the four-momenta of the final state neutrinos, p_1, p_2 are the four-momenta of the final state partons that lead to creation of extra jets and q_1, q_2 are the four-momenta of the incoming partons. The same set of assumptions made in the signal case about the measured lepton energies, jet angles, and transverse components of the initial parton energies applies here as well. The differential cross-section for the process then takes the form:

$$\begin{aligned} d\sigma = & \left(\frac{1}{(2\pi)^3}\right)^6 \iint \sum_{i,j} |M|^2 (2\pi)^4 \delta^4(q_1 + q_2 - \ell_1 - \nu_1 - p_1 - \ell_2 - \nu_2 - p_2) \\ & \delta(q^x)\,\delta(q^y)\,dq^x\,dq^y\; f^i_{\texttt{PDF}}\left(\frac{q_1^i}{E_{\texttt{beam}}}, Q^2\right)\; f^j_{\texttt{PDF}}\left(\frac{q_2^j}{E_{\texttt{beam}}}, Q^2\right)\; f_{\texttt{flux}}(q_1^z, q_2^z)\,\frac{dq_1^i dq_2^j}{E_{\texttt{beam}}} \\ & \delta^3(\ell_1 - L_1)\,\delta^3(\ell_2 - L_2)\,\frac{d^3\ell_1}{2E_{\ell_1}}\frac{d^3\ell_2}{2E_{\ell_2}} f(E_{p_1}, E_{j_1})\, f(E_{p_2}, E_{j_2}) \\ & \delta(\theta_{p_1} - \theta_{j_1})\,\delta(\theta_{p_2} - \theta_{j_2})\,\delta(\phi_{p_1} - \phi_{j_1})\,\delta(\phi_{p_2} - \phi_{j_2})\frac{d^3p_1}{2E_{p_1}}\frac{d^3p_2}{2E_{p_2}}\frac{d^3\nu_1}{2E_{\nu_1}}\frac{d^3\nu_2}{2E_{\nu_2}} \end{aligned} \tag{8.9}$$

Here, $\delta^3(\ell_i - L_i)$, $\delta(\theta_{p_1} - \theta_{j_1})$, and $\delta(\phi_{p_i} - \phi_{j_i})$ enforce the assumptions about lepton

[4] I would like to acknowledge Bo Jayatilaka for substantial contributions to the material covered in this section

momenta and jet angles, as in Equation 7.6. The same collider approximation as in the signal case, $q_{x,y} \ll q_z$ and massless incoming partons, leads to $q_i^0 = q_i^z$. Again, the δ-function is q_x and q_y can be refined into smoother distributions of incoming parton momenta. This would not complicate the formalism substantially, but considerably more computing resources would be required.

8.4.2 Phase space transformation and integration

Following a prescription analogous to the one developed for the signal case[5], a phase-space transformation is performed in order to make the integration over parton-level variables more efficient. Invariant masses of intermediate particles are introduced, in this case, the two W-bosons, using the procedure described in Appendix B. The integration method is quite similar to the signal case as described in Chapter 7. After integrating over $d^3\ell_i$ and the δ-functions introduced by the phase-space transformation, we express all the parton variables except the neutrino momenta in spherical coordinates, integrate over the parton angles and are left with:

$$
\begin{aligned}
d\sigma = \int (2\pi)^4 \frac{|M|^2}{2} \left(\frac{1}{(2\pi)^3}\right)^6 & f^i_{\texttt{PDF}}(\frac{q_1^z}{E_{\texttt{beam}}}, Q^2)\ f^j_{\texttt{PDF}}(\frac{q_2^z}{E_{\texttt{beam}}}, Q^2)\ \frac{1}{E^2_{\texttt{beam}}} \\
& \delta\left((L_1+\nu_1+p_1)_x + (L_2+\nu_2+p_2)_x\right)\ \delta\left((L_1+\nu_1+p_1)_y + (L_2+\nu_2+p_2)_y\right) \\
& \delta\left((L_1+\nu_1)^2 - M^2_{W_1}\right)\ \delta\left((L_2+\nu_2)^2 - M^2_{W_2}\right) \\
& \frac{p^2_{1R}\sin\theta_{p_1} dp_{1R}}{2E_{p_1}}\ \frac{p^2_{2R}\sin\theta_{p_2} dp_{2R}}{2E_{p_2}}\ \frac{d^3\nu_1}{2E_{\nu_1}}\ \frac{d^3\nu_2}{2E_{\nu_2}}\ \frac{1}{2E_{L_1}}\ \frac{1}{2E_{L_2}} \\
& f_{\texttt{flux}}(q_1^z, q_2^z)\ f(E_{p_1}, E_{j_1})\ f(E_{p_2}, E_{j_2})\ dM^2_{W_1}\ dM^2_{W_2}
\end{aligned}
\tag{8.10}
$$

At this point only the integration over the six neutrino momentum components

[5] refer to Chapter 7

remains to be done. Unlike the signal case, we only have two intermediate state invariant masses to integrate over. Thus, we must retain two neutrino momentum components as integration variables. We chose the z-components in order to make the expressions symmetric and simplify the algebra. We are then left with 6 integrations: 2 over the neutrino components ν_{1z} and ν_{2z}, 2 over the absolute magnitudes of the momenta of the partons which hadronized into jets p_{1R} and p_{2R}[6], and 2 over the assumed invariant masses of the W-bosons m_{W_1} and m_{W_2}. A proper Jacobian term (from Equation 7.17) as well as solutions for the remaining four neutrino momentum components in terms of either known quantities or the integration variables are required to complete the evaluation.

8.4.3 Neutrino solutions

The system of equations for neutrino momenta for W pairs is the following:

$$\begin{aligned}
&(L_1 + \nu_1)^2 = M_{W_1}^2 \\
&(L_2 + \nu_2)^2 = M_{W_2}^2 \\
&(L_1 + \nu_1 + p_1)_x + (L_2 + \nu_2 + p_2)_x = 0 \\
&(L_1 + \nu_1 + p_1)_y + (L_2 + \nu_2 + p_2)_y = 0
\end{aligned} \tag{8.11}$$

The need to solve for only four of the six neutrino components makes the derivation of neutrino solutions simpler than in the signal case. We define:

$$\begin{aligned}
Q_x &\equiv -L_{1x} - L_{2x} - p_{1x} - p_{2x} \\
Q_y &\equiv -L_{1y} - L_{2y} - p_{1y} - p_{2y}
\end{aligned} \tag{8.12}$$

Then, using the last two equations in (8.11), we make the substitutions $\nu_{2x} =$

[6]these can be also looked at as radial components of the parton three-momenta

$Q_x - \nu_{1x}$ and $\nu_{2y} = Q_x - \nu_{1y}$ in the first two equations. We expand the first two equations in (8.11) and derive two coupled quadratic equations in terms of ν_{2x} and ν_{2y} that are of the form:

$$\begin{aligned} a_1\nu_{2x}^2 + a_2\nu_{2x}\nu_{1y} + a_3\nu_{1y}^2 + a_4\nu_{2x} + a_5\nu_{1y} + a_6 = 0 \\ b_1\nu_{2y}^2 + b_2\nu_{2x}\nu_{1y} + b_3\nu_{1x}^2 + b_4\nu_{2y} + b_5\nu_{1x} + b_6 = 0 \end{aligned} \tag{8.13}$$

The two coupled equations are then converted to a single fourth order polynomial which can be solved numerically using the Sturm Sequence technique [29]. Alternatively, an analytical solution similar to the one shown in Appendix D can be employed.

8.4.4 Jacobian factor

The Jacobian factor that appears from integrations over neutrino momenta components has the form:

$$J = \left| \frac{\partial f_i}{\partial \nu_{(1,2)(x,y,z)}} \right| \tag{8.14}$$

The f_i are the functions of neutrino momenta that occur inside δ-functions:

$$\begin{aligned} f_1 &= ((L_1 + \nu_1 + p_1)_x + (L_2 + \nu_2 + p_2)_x) \\ f_2 &= ((L_1 + \nu_1 + p_1)_y + (L_2 + \nu_2 + p_2)_y) \\ f_3 &= \left((L_1 + \nu_1)^2 - M_{W_1}^2\right) \\ f_4 &= \left((L_2 + \nu_2)^2 - M_{W_2}^2\right) \\ f_5 &= \nu_{1z} \\ f_6 &= \nu_{2z} \end{aligned} \tag{8.15}$$

The determinant of the Jacobian has the form:

$$\begin{vmatrix} 1 & 0 & J_{3x} & 0 & 0 & 0 \\ 0 & 1 & J_{3y} & 0 & 0 & 0 \\ 1 & 0 & 0 & J_{4x} & 0 & 0 \\ 0 & 1 & 0 & J_{4y} & 0 & 0 \\ 0 & 0 & 0 & 0 & 1 & 0 \\ 0 & 0 & 0 & 0 & 0 & 1 \end{vmatrix}$$

This evaluates to:

$$J = |J_{3y}J_{4x} - J_{3x}J_{4y}| \tag{8.16}$$

Where:

$$\begin{aligned} J_{3x} &= \frac{\partial f_3}{\partial \nu_{1x}} = \frac{2L_1^0\nu_{1x}}{\sqrt{\nu_{1x}^2 + \nu_{1y}^2 + \nu_{1z}^2}} - 2L_{1x} \\ J_{3y} &= \frac{\partial f_3}{\partial \nu_{1y}} = \frac{2L_1^0\nu_{1y}}{\sqrt{\nu_{1x}^2 + \nu_{1y}^2 + \nu_{1z}^2}} - 2L_{1y} \\ J_{4x} &= \frac{\partial f_3}{\partial \nu_{2x}} = \frac{2L_2^0\nu_{2x}}{\sqrt{\nu_{1x}^2 + \nu_{1y}^2 + \nu_{1z}^2}} - 2L_{2x} \\ J_{4y} &= \frac{\partial f_3}{\partial \nu_{2y}} = \frac{2L_2^0\nu_{2y}}{\sqrt{\nu_{1x}^2 + \nu_{1y}^2 + \nu_{1z}^2}} - 2L_{2y} \end{aligned} \tag{8.17}$$

8.4.5 Final integral

The Jacobian factor is evaluated after neutrino solutions are found and a final expression for the unnormalized probability for WW+2 jets events becomes:

$$\begin{aligned}\frac{d\sigma}{d\mathbf{x}} = & \left(\frac{1}{(2\pi)^3}\right)^6 (2\pi)^2 \iint \sum_{i,j} \frac{|M|^2}{2E_{\texttt{beam}}^2} \frac{p_{1R}^2 \sin\theta_{p_1} dp_{1R}}{2E_{p_1}} \frac{p_{2R}^2 \sin\theta_{p_2} dp_{2R}}{2E_{p_2}} \\ & \frac{J^{-1}}{E_{\nu_1} E_{\nu_2} E_{L_1} E_{L_2}} d\nu_{1z} d\nu_{2z} f_{\texttt{PDF}}^i(\frac{q_1^z}{E_{\texttt{beam}}}, Q^2)\ f_{\texttt{PDF}}^j(\frac{q_2^z}{E_{\texttt{beam}}}, Q^2) \\ & f_{\texttt{flux}}(q_1^z, q_2^z) f(E_{p_1}, E_{j_1})\ f(E_{p_2}, E_{j_2})\ M_{W_1}\ M_{W_2}\ dM_{W_1}\ dM_{W_2}\end{aligned} \tag{8.18}$$

This 6-dimensional integral is very similar to the one obtained in the signal case. It is evaluated over the parton momenta, the W boson invariant masses, and the neutrino momenta z components to obtain the differential cross-section. The sum over i, j stands for the sum over incoming parton flavors.

8.4.6 Performance

The ALPGEN $WWjj$ matrix element is shown in Figure 8.5 evaluated over Monte Carlo generated parton-level $WWjj$ and $t\bar{t}$ events. We also evaluate the $WWjj$ probability on simulated events that have passed final dilepton selections for the DIL sample[7]. As with the Zjj case, the event selection accepts the background events which are kinematically very similar to $t\bar{t}$. There is still, however, visible discrimination between $WWjj$ events and $t\bar{t}$ events using the $WWjj$ probability calculation, as seen in Figure 8.6.

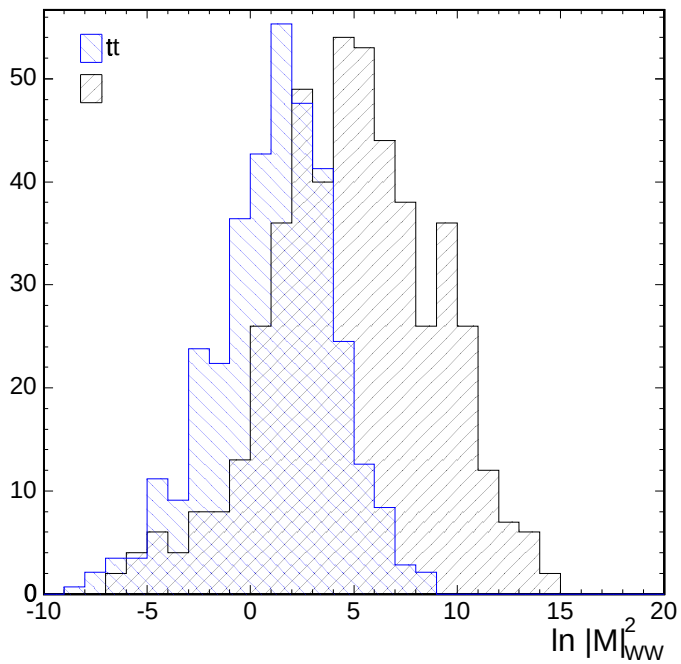

Figure 8.5: Evaluation of the squared matrix element for $pp \to WW(\to l\nu l\nu) + 2jets$ for parton-level $t\bar{t}$ and $WW + 2p$ events.

[7]sample composition described in Chapter 4

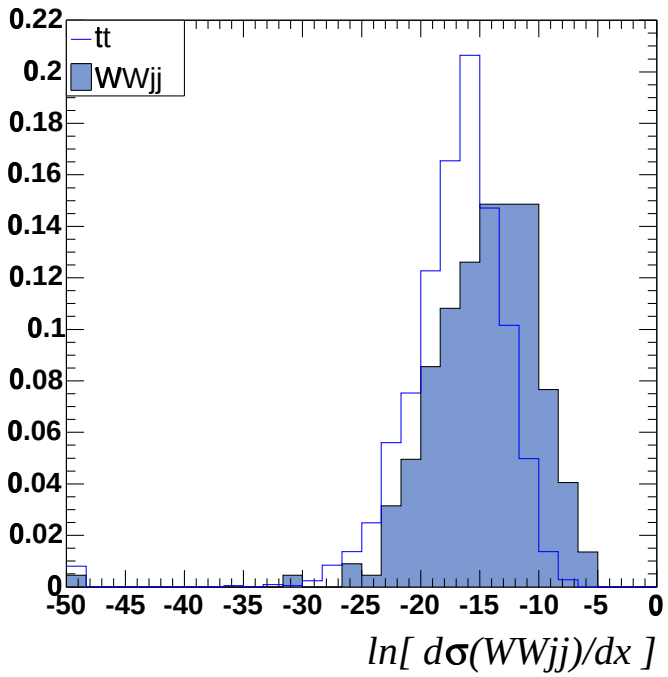

Figure 8.6: Evaluation of the $WWjj$ probability for WW and $t\bar{t}$ events in fully simulated events, after the signal selection cuts have been applied.

8.5 Modeling of backgrounds with fake leptons

Modeling of events with a fake lepton presents a particular challenge, as they do not correspond simply to a particular physical process.[8]

These events enter into the sample when a jet fakes a lepton signature, most typically an electron. As the rate at which jets fake leptons is very small, we expect the vast majority of the fake events to have a single real lepton and three jets. Events of this category are typically produced via the process

$$p\bar{p} \rightarrow Wjjj \rightarrow l\nu jjj$$

where the neutrino escapes without detection.

Using this process as the basis for our model, we write

$$P_{fake} = P_{Wjjj}(j_1, j_2, l_1, [l_2 \rightarrow j_3]) + P_{Wjjj}(j_1, j_2, [l_1 \rightarrow j_3], l_2)$$

where we sum over the possibilities that either lepton is a fake originating from a jet. Calculation of P_{Wjjj} follows the style of the other probability calculations above.

8.5.1 Wjjj: differential cross section

Calculation of the differential cross-section for W+3jet production requires integration of the matrix element over the phase space. In this case, the number of constraints from the measurement of the final state objects reduces the number of integrals to four.

We use the following notation: p_1, p_2, p_3 are the four-momenta of the final state partons which lead to creation of extra jets, L is the measured four-momentum of the

[8] I would like to acknowledge Daniel Whiteson for substantial contributions to the material covered in this section

final state lepton, ν the four-momentum of the final state neutrino and q_1, q_2 — the four-momenta of incoming partons. The expression for the differential cross-section of this process is of the form:

$$
\begin{aligned}
d\sigma = & \sum_{a,b} \iint \frac{1}{(2\pi)^{12}} \frac{1}{32} \frac{1}{E_L E_\nu E_{p_1} E_{p_2} E_{p_3}} \\
& f(E_{p_1}, E_{j_1})\, f(E_{p_2}, E_{j_2})\, f(E_{p_e}, E_{j_e})\, {p_{R1}}^2 \sin\theta_{p_1}\, {p_{R2}}^2 \sin\theta_{p_2}\, {p_{R3}}^2 \sin\theta_{p_3} \\
& \delta(\phi_{p_1} - \phi_{j_1})\, \delta(\theta_{p_1} - \theta_{j_1})\, \delta(\phi_{p_2} - \phi_{j_2})\, \delta(\theta_{p_2} - \theta_{j_2})\, \delta(\phi_{p_3} - \phi_{j_3})\, \delta(\theta_{p_3} - \theta_{j_3}) \\
& dp_{R1}\, d\theta_{p_1}\, d\phi_{p_1}\, dp_{R2}\, d\theta_{p_2}\, d\phi_{p_2}\, dp_{R3}\, d\theta_{p_3}\, d\phi_{p_3} d^3\nu \\
& f^a_{\mathtt{PDF}}(\frac{q_1^z}{E_{\mathtt{beam}}}, Q^2)\; f^b_{\mathtt{PDF}}(\frac{q_2^z}{E_{\mathtt{beam}}}, Q^2)\, \frac{dq_1^z\, dq_2^z}{E^2_{\mathtt{beam}}} \\
& \delta^4(q_1 + q_2 - L_1 - p_1 - p_2 - p_3) \frac{(2\pi)^4}{4(q_1^{\mathtt{cm}}\sqrt{s})} |\mathcal{M}|^2
\end{aligned}
\tag{8.19}
$$

In the above expression we set the transverse components of incoming parton momenta to zero. This simplification can be removed if necessary by the method similar to one used in derivation of the signal differential cross-section.

Using the same collider approximation as before, without the loss of generality $q_1^0 = q_1^z$ and $q_2^0 = q_2^z$. Integration over $dq_1^z\, dq_2^z$ and t and z parts of the four-dimensional δ-function result in the extra factor of 1/2 and the following substitution:

$$
\begin{aligned}
q_1^z &= \frac{1}{2}\left((L^z + p_1^z + p_2^z + p_3^z) + (L^0 + p_1^0 + p_2^0 + p_3^0)\right) \\
q_2^z &= \frac{1}{2}\left((L^z + p_1^z + p_2^z + p_3^z) - (L^0 + p_1^0 + p_2^0 + p_3^0)\right)
\end{aligned}
\tag{8.20}
$$

Evaluation of the integrals over $d^3p_1\, d^3p_2\, d^3p_3$ is performed in spherical coordinates, in order to take advantage of the angular δ-functions. After the angular integrations, all $\phi_{p_{1,2,3}}$ and $\theta_{p_{1,2,3}}$ are replaced by corresponding jet angles.

The entire expression for the differential cross-section:

$$
\begin{aligned}
d\sigma = & \sum_{a,b} \iint \frac{dp_{R_1} dp_{R_2} dp_{R_3} d\nu_z}{32\,(2\pi)^{12}\, E_L E_\nu E_{p_1} E_{p_2} E_{p_3}} \\
& f(E_{p_1}, E_{j_1}) f(E_{p_2}, E_{j_2}) f(E_{p_3}, E_{j_3})\, {p_{R1}}^2 {p_{R2}}^2 {p_{R3}}^2 \sin\theta_{j_1} \sin\theta_{j_2} \sin\theta_{j_3} \\
& f^a_{\mathtt{PDF}}(\frac{q_1^z}{E_{\mathtt{beam}}}, Q^2) f^b_{\mathtt{PDF}}(\frac{q_2^z}{E_{\mathtt{beam}}}, Q^2) \frac{(2\pi)^4}{4(q_1^{\mathtt{cm}}\sqrt{s})} \frac{|\mathcal{M}|^2}{2}
\end{aligned}
\tag{8.21}
$$

where the sum is over possible incoming parton flavors. The flux factor $4(q_1^{\mathtt{cm}}\sqrt{s})$ can be rewritten as $2|q_1^z q_2^z|$.

8.5.2 Performance

The matrix element for $Wjjj$ evaluated over parton-level events is shown in Figure 8.7. It is able to separate $t\bar{t}$ events from $Wjjj$ events quite well. In Figure 8.8, we have discarded the neutrino information, Gaussian smeared the parton-level quantities and performed the four-dimensional integration using Gaussian transfer functions.

Finally, we evaluate the full fake probability, applying the integration and transfer functions as above. We employ a sample of events from the data which are candidates to produce a fake lepton. Figure 8.9 shows the resulting distributions.

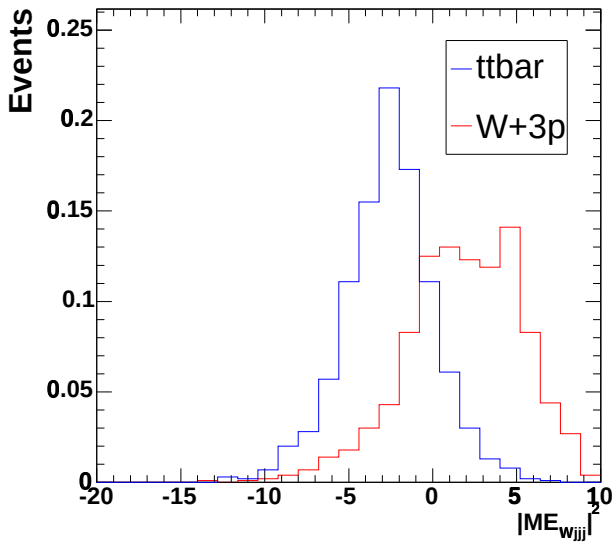

Figure 8.7: Evaluation of the squared matrix element for $pp \to W(\to l\nu) + 3jets$ for parton-level $t\bar{t}$ and $W + 3p$ events.

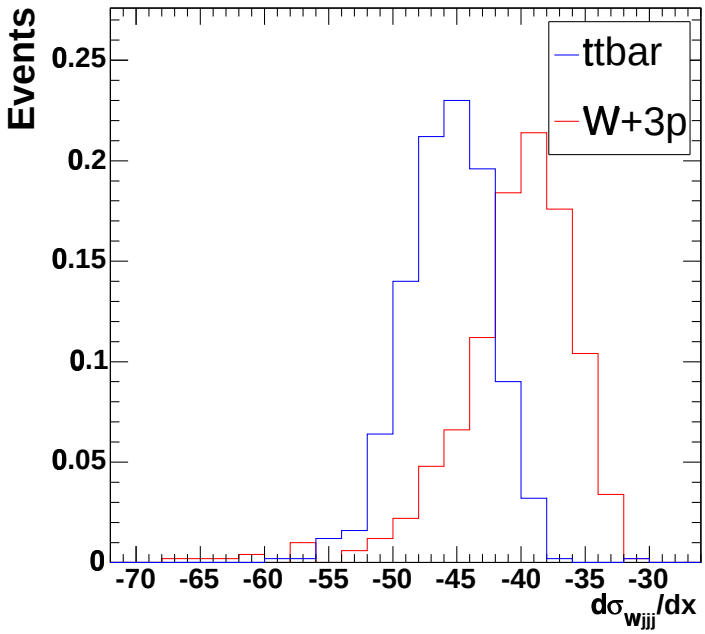

Figure 8.8: Evaluation of the $Wjjj$ probability for Gaussian smeared $Wjjj$ and $t\bar{t}$ events, neutrino information discarded.

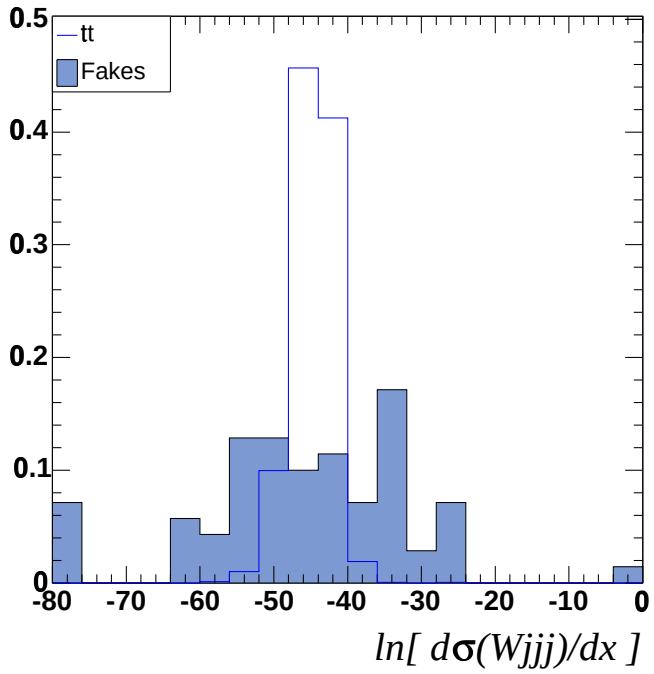

Figure 8.9: Evaluation of the $Wjjj$ probability for fully simulated $t\bar{t}$ and events from the data which are candidates to produce a fake lepton.

Chapter 9

Calibration of Response and Error Estimate

The mass extraction technique used in this analysis works well for the class of the events that are described by the model of top quark pair production and decay which was discussed in Chapter 7. It measures the mass without significant bias and with a well-estimated error[1].

The events in the data sample, however, are not restricted to this class of events. The response of the method is slightly degraded by the presence of poorly reconstructed jets, mismatched[2] jets, events with secondary leptons from $W \rightarrow \tau$ decays and background processes. Some of the factors that impair the method's ability to extract the true value of mass can be accounted for by proper modeling of corresponding effects, for example by introducing background probabilities. However, some of the effects not accounted for in our simple model (e.g. initial and final state radiation, $W \rightarrow \tau$ decay) cannot be easily treated by modifications to the likelihood expression.

[1] refer to Section 7.2.3

[2] the case where neither of the two jets with highest E_T is a direct product of the parton being considered in the matrix element evaluation

Thus, the expression for the posterior probability distribution of top-quark mass that is used in this analysis lacks terms for hard to model components. We can, however, explicitly correct for the incomplete nature of the method by measuring any systematic shift in the extracted value of the top quark mass and by increasing the estimated statistical uncertainty of the measurement to agree with the deviations between extracted mass and the true mass observed in a large ensemble of identical experiments. In this Chapter, the response of the method is measured and a calibration correction is derived. We consider sequentially the cases of signal only, signal and background events present but with only signal accounted for in the likelihood expression, and signal and background present where the latter is also accounted for, as best one can do, in the likelihood expression.

9.1 Signal only tests with P_s

We first measure the response of the method using only signal events. The number of events in each pseudo-experiment is a random number, Poisson distributed with expected number of events shown in Table 4.1. The probability expression in this case includes only the term that describes leading order $t\bar{t}$ production. Figure 9.1 shows that the response is linear, with a slope very close to 1.0. The statistical uncertainty is underestimated due to approximations made in the calculation of the likelihood, as discussed in detail in Chapter 7.

Figure 9.2 shows the residual[3] and pull[4] parameters.

[3] $DeltaM_t \equiv M_t^{\text{extracted}} - M_t$

[4] $\frac{M_t^{\text{extracted}} - M_t}{\sigma_{\text{estimated}}}$

9.2 Signal and background tests with P_s

At this stage we construct pseudo-experiments that follow the expected sample composition shown Table 4.1, while still using only the signal term in the probability expression. Figure 9.3 shows that the performance degrades significantly as the background smears out the top mass information. The degradation is manifested by the decrease in the slope of the response. The reasons for the decrease in sensitivity are quite obvious — none of the added backgrounds are properly described by signal-only probability expression.

9.3 Signal and background tests with P_s and P_b

When the description of the background processes in the form of P_b is added to the likelihood machinery, a significant amount of sensitivity to the top mass is recovered. It should be noted that the only backgrounds that are described are Z-boson production with two additional jets, W-boson pair production and W boson with three jets with one of the jets being mis-identified as a lepton. While the inclusion of the background probabilities improves the description of the events in the pseudo-experiments, it does not return it to the level of the signal-only case, for two reasons. First, the background probabilities are an imperfect description of the background events, due the the same assumptions made during the formulation of the signal probability. Second, the generated pseudo-experiments contain backgrounds that are not described by any probability term ($Z \to \tau\tau$ and WZ with extra jets).

Figure 9.4 shows the response with the full probability expression. Table 9.1 gives the estimated statistical error as each background is added to the pseudo-experiments and likelihood. Again, the introduction of background events increases the estimated statistical uncertainty, while including the background terms into the probability

Experiments	Likelihood	Response slope	Mass RMS
Signal	Signal	1.00	8.51 GeV
Signal+Z	Signal	0.90	9.82 GeV
Signal+Z	Signal+Z	0.95	8.62 GeV
Signal+Fakes	Signal	0.83	9.11 GeV
Signal+Fakes	Signal+Fake	0.94	8.47 GeV
Signal+WW	Signal	0.93	8.84 GeV
Signal+WW	Signal+WW	0.94	8.70 GeV
Signal+Z+WW+Fakes	Signal	0.74	11.07 GeV
Signal+Z+WW+Fakes	Signal+Z+WW+Fakes	0.86	9.41 GeV
Signal+Bg	Signal	0.72	11.17 GeV
Signal+Bg	Signal+Z+WW	**0.84**	**9.50** GeV

Table 9.1: Degradation of the error as background events are added to the simulated sample, and recovery of the sensitivity as the background probability is included. These estimates are obtained for the expected sample composition given by Table 4.1

expression we are able to recover part of the sensitivity. It should be noted that the slope of the response curve also improves when the background terms are included in the likelihood expression.

9.4 Derivation of response correction

The necessary bias correction is based on the numbers presented in Figure 9.4. We transform the raw mass into the corrected mass using a linear correction of the form:

$$M_t = 178.0\,\mathrm{GeV} + (M_t^{raw} - M_0)/s \tag{9.1}$$

where $M_0 = 177.2 \pm 0.21$ and $s = 0.84 \pm 0.02$. The statistical error on the parameters of this transformation is propagated to a systematic error in the final analysis. Figure 9.6

Experiments	Likelihood	Fitted Pull Width
Sig	Sig	1.40 ± 0.05
Sig+Z	Sig+Z	1.37 ± 0.05
Sig+Z+WW	S+Z+WW	1.38 ± 0.06
Sig+Z+WW+Fakes	S+Z+WW+F	1.44 ± 0.05
Sig+Z+WW+Fakes+$Z \to \tau\tau$	S+Z+WW+F	1.46 ± 0.05
Sig+Z+WW+Fakes+$Z \to \tau\tau + WZ$	S+Z+WW+F	1.49 ± 0.05

Table 9.2: Effect on the fitted pull of modeled and unmodeled backgrounds.

Sample	Fitted Pull Width
Herwig	1.49 ± 0.05
Pythia	1.43 ± 0.06
FSR less	1.44 ± 0.05
FSR more	1.44 ± 0.06
ISR less	1.46 ± 0.05
ISR more	1.45 ± 0.05

Table 9.3: Effect on the fitted pull variation of the signal sample

shows residuals and pull parameters of the slope-corrected and error-corrected top quark mass.

9.5 Derivation of error correction

The background events that are not taken into account by our likelihood expression contribute to the underestimate of the error. In Figure 9.5, we can see the effect on the extracted mass, measured error and fitted pull width as a function of the number of background events in pseudo-experiments. If the background probability is not included, the unmodeled background will increase the width of the extracted mass distribution but not the predicted error, resulting in an underestimate of the actual error and a larger pull width. When the background probability is included, the width of the extracted mass is relatively flat, and the result pull widths are stable.

In Table 9.2, we can see the effect on the fitted pull width in pseudo-experiments with successively increased backgrounds. Backgrounds for which we have a model do not increase the pull width, while unmodeled backgrounds do widen the pull. In Table 9.3, we verify that the final pull width is not very sensitive to reasonable changes in the underlying model.

We derive a correction factor for the expected error in the mass by fitting the pull width as a function of mass with a constant function, see Figure 9.6. We measure

$$S_{error} = 1.51$$

and apply this to all samples independent of M_t. The final corrected and scaled performance is illustrated by Figure 9.6 that shows pull width as a function of M_t before and after the error scaling. Figure 9.7 shows the distributions of ensemble means, errors and pull for the sample with $M_t = 178$ GeV after the slope correction and the error estimate scaling has been applied.

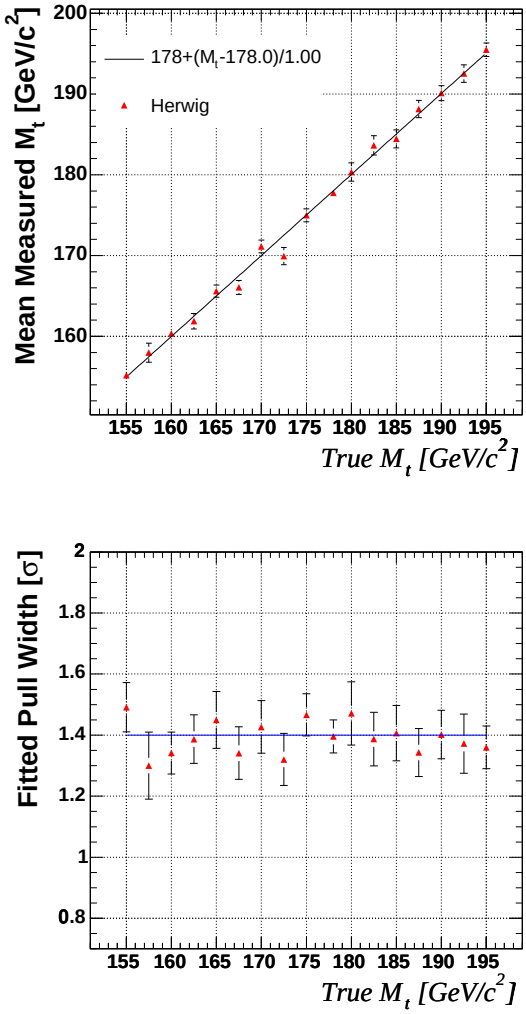

Figure 9.1: Top, response for pseudo-experiments of signal events, using only P_s to extract the mass. Bottom, width of pull distributions.

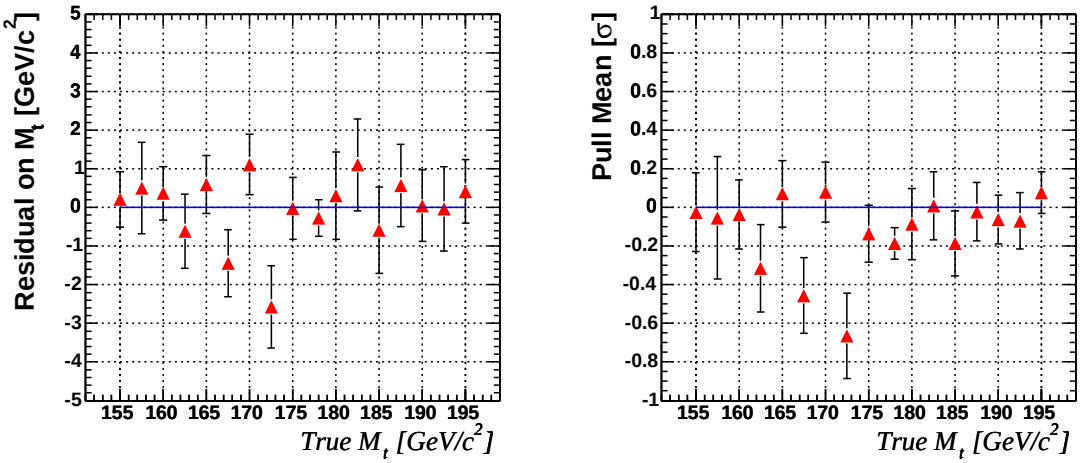

Figure 9.2: Residual in top mass, and mean of pull distribution for varying simulated M_t, in signal-only pseudo-experiments.

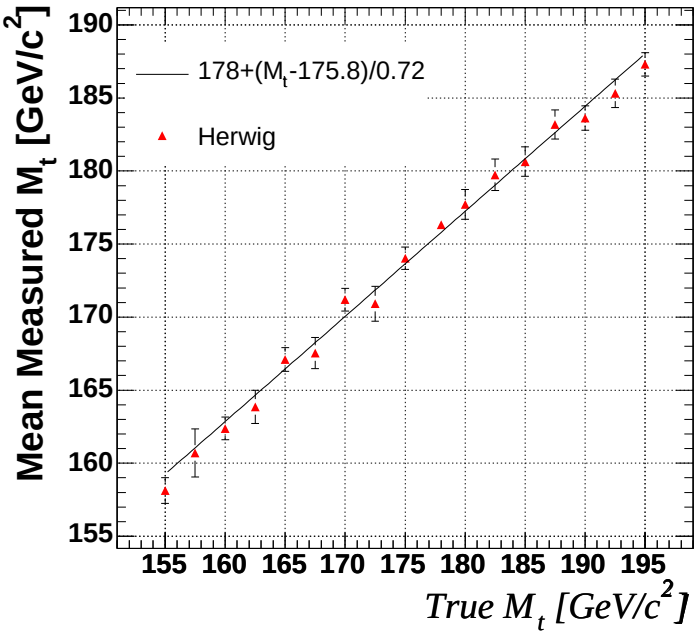

Figure 9.3: Response curve for pseudo-experiments of signal and background events, using only P_s to extract the mass.

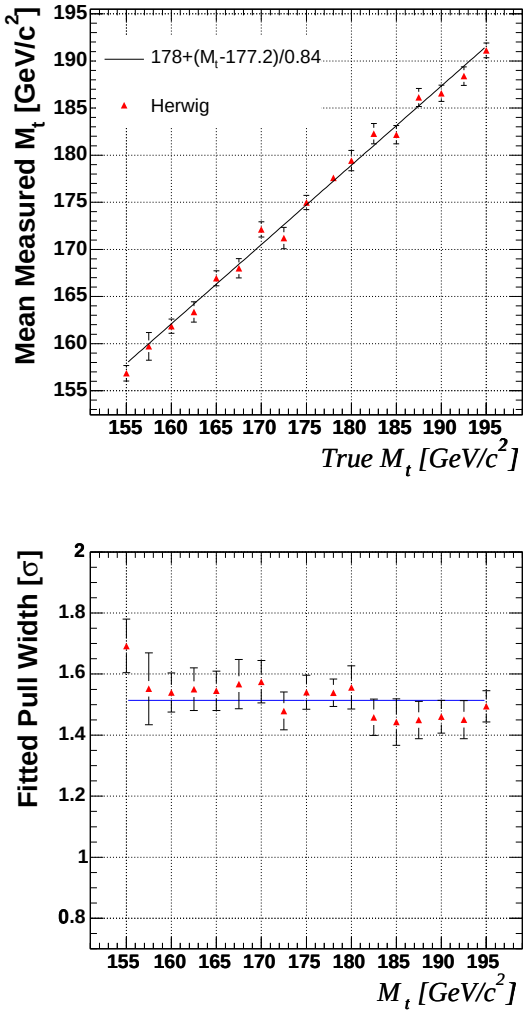

Figure 9.4: Top, response for pseudo-experiments of signal and background events, using P_s and P_b to extract the mass. Bottom, width of pull distributions.

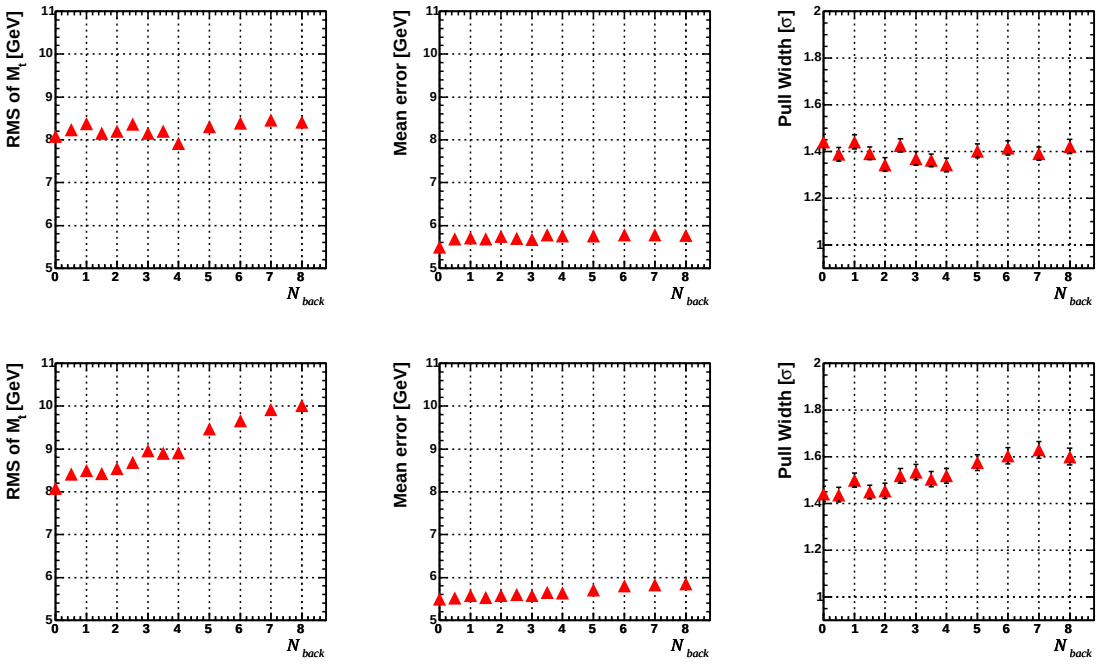

Figure 9.5: RMS of mass distribution, mean estimated statistical uncertainty and fitted pull width as a function of the number of expected Z background events with (*top*) and without (*bottom*) background probability. Expected number of signal events is kept constant. The statistical uncertainty is estimated from a width of the probability distribution for a given pseudo-experiment. The mean is taken over all generated pseudo-experiments.

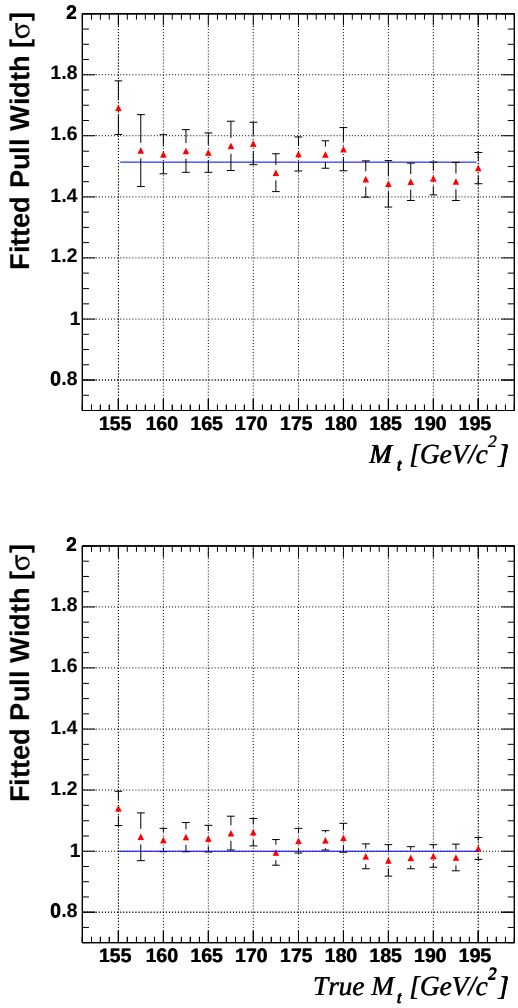

Figure 9.6: Pull widths before (*top*) and after (*bottom*) error scaling, for samples of different top mass using the DIL selection.

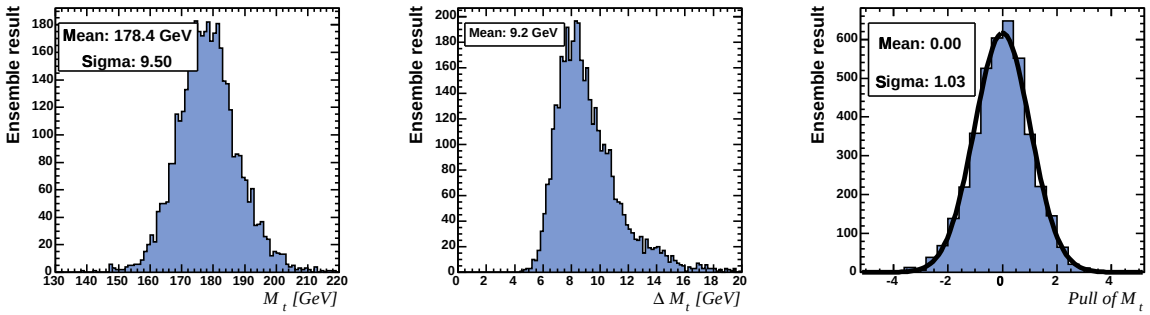

Figure 9.7: Extracted mass, error and pull for DIL selection and $M_t = 178$ GeV, all corrections applied.

Chapter 10

Systematics

The measurement presented in this thesis relies on the Monte Carlo simulated events in order to correct for various small systematic shifts. The majority of systematic errors, therefore, come from the uncertainty in how well the simulation is modeling the data. The correction prescription was presented in Chapter 9 together with a list of effects responsible for the introduction of such corrections. In this Chapter, the facets of the simulation which may not accurately describe the observed data are summarized and the sensitivity of the measurement is estimated.

The strategy used to evaluate the impact of such deviations consists of the following steps: first, pseudo-experiments are performed using a pool of events in which a certain parameter of the dataset has been modified; second, the average measured mass is extracted and the typical shift is determined and attributed to the introduced differences. In some cases, the magnitude of the shift is smaller than its assigned statistical error. For these effects the magnitude of the statistical error on the shift is taken as a systematic uncertainty.

10.1 Jet response

The measured energy of jets is calibrated using simulated and data events. Due to some uncertainty associated with the underlying hadronization process and limited data statistics, there is an uncertainty in the correction which needs to be applied to the raw jet energy.

The jet energy scale is varied in simulated events within the uncertainty and the difference in extracted top mass is measured.

Sample	Measured M_t for $M_t^{true} = 178.0$
JES $+1\sigma$	181.14 ± 1.20 GeV
JES -1σ	176.01 ± 1.20 GeV

Half of the difference between the two measurements, $\Delta_{\texttt{JES}} = 2.53$ GeV, is taken as the estimate of the corresponding systematic uncertainty.

The jet energy scale calibration is subdivided into several correction "levels" that account for different effects of hadronization and detector response[1]. The following table presents the values obtained for the top mass by changing the scale at every level by $\pm\sigma$ and recording ΔM_t: results in:

Level	$+\sigma$	$-\sigma$	$\Delta M_t/2$
Relative	179.48	177.97	0.75
Multiple Interactions	178.46	178.46	0.00
Absolute Correction	180.02	177.85	1.09
Underlying event	179.4	178.75	0.32
Out-of-Cone	181.14	176.83	2.16
Splash-out	179.3	178.71	0.29

[1]for a description of jet energy scale correction levels refer to Section 3.2.4

Combination of the above uncertainties in quadrature results in the estimate of the total uncertainty in the top mass, due to uncertainties in the jet energy scale, of 2.57 GeV. This is in excellent agreement with the value deduced by an overall change in the energy scale.

The jet energy scale and its systematic errors are derived primarily for events with light quark and gluon jets. Studies [30] have demonstrated that in lepton+jets events, the b-jet energy scale may be misestimated by 0.6%. For comparison, we have measured that moving b-jet energy scale up by 1% changes the extracted mass by 0.8 GeV. Thus, we assign an additional uncertainty of 0.48 GeV.

10.2 Generator

We measure the difference in our extracted mass when using events simulated with Pythia and with Herwig Monte Carlo event generators.

Sample	Measured M_t for $M_t^{true} = 178.0$
Herwig	178.2 ± 0.52 GeV
Pythia	178.5 ± 0.64 GeV

We take the difference between the two measurements, $\Delta_{Gen} = 0.2 \pm 0.8$ GeV.

10.3 Response calibration

The final corrected mass estimate depends on the parameters of the response curve[2]. Uncertainty in these translates directly into uncertainty in our mass measurement.

[2] refer to Section 9.4

We vary the response parameters within the statistical errors of the fit, and measure the difference in the extracted mass.

	Variation of (offset,slope)			
Sample	$(+\sigma, +\sigma)$	$(-\sigma, -\sigma)$	$(+\sigma, -\sigma)$	$(-\sigma, +\sigma)$
$M_t = 170$	171.7	171.9	171.4	172.2
$M_t = 178$	178.0	178.5	178.0	178.5
$M_t = 185$	183.4	184.1	183.6	183.9

In order to be conservative, we take half of the difference between the pair with the largest variation, $\Delta_{Resp} = 0.4$ GeV.

10.4 Sample composition

A knowledge of the expected signal and background composition of the sample is required in order to construct pseudo-experiments from which the response curve is extracted. Given the response curve, the difference in the mean extracted mass of an ensemble of pseudo-experiments can be measured by varying the background composition within the quoted uncertainties. Note that the uncertainty in the number of expected $t\bar{t}$ events includes, and is dominated by, the theoretical uncertainty in the cross-section of 10%.

Varied Sample	$+\sigma$	$-\sigma$	Δ
$t\bar{t}$	178.1	178.4	0.3
$Fakes$	178.0	177.2	0.4
Z	177.3	177.9	0.3
WW	177.5	178.1	0.3
WZ	178.1	177.9	0.2
$Z \to \tau\tau$	178.1	177.6	0.3

These results indicate that we are not strongly sensitive to the background composition. The size of the $t\bar{t}$ uncertainty is taken as a systematic error, $\Delta_{Sample} = 0.3$ GeV.

10.5 PDF uncertainties and α_s

To estimate the error due to the uncertainties in the Parton Distribution Functions (PDFs), we use an event reweighting procedure described in [31]. The uncertainties in global PDF fit parameters produce an uncertainty in the measured quantities and a proper propagation prescription is presented in [32]. The eigenvectors in the space of the PDF fit parameters are obtained by diagonalization of the PDF fit χ^2 Hessian matrix in the neighborhood of the global minimum. The main idea of the reweighting prescription is to avoid generating disjoint Monte Carlo samples for different sets of eigenvectors in question, but rather compute the corresponding event weights and build the pseudo-experiments appropriately, with sampling based on these weights. The Pythia sample was reweighted according to 20 sets of positive and negative eigenvectors and pseudo-experiments were drawn such that events with higher weight were more likely to be chosen for a given pseudo-experiment. Figure 10.1 shows half the difference between the positive and negative eigenvectors. The total error added

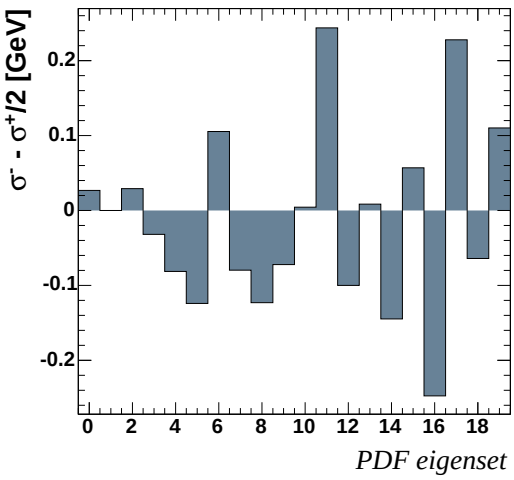

Figure 10.1: Difference in extracted mass between the positive and negative PDF eigenvectors for a Pythia sample.

in quadrature is $\Delta_{PDF} = 0.53$ GeV.

In addition, we compare samples with different PDFs, CTEQ6L and MRST72 and confirm that their central values agree well.

Sample	M_t
Pythia, CTEQ5L	178.5 ± 0.64 GeV
Pythia, MRST72	178.6 ± 0.59 GeV
Pythia, MRST75	178.3 ± 0.59 GeV

The two samples MRST72 and MRST75 use different values of α_s to calculate the PDFs. The difference in these two provides a measure of our sensitivity to the uncertainty in α_s. We estimate our systematic errors due to variation of α_s to be $\Delta_{\alpha_s} = 0.25 \pm 0.83$ GeV.

10.6 Radiation of additional gluons

Our model does not contain any description of initial (ISR) or final (FSR) state radiation of gluons, which may contribute significantly to the fraction of mismeasured events. The rate of initial state radiation can be well studied in Z+jet events, as there is no final state radiation. The radiation is found to depend smoothly on the energy transfer [33], and can be examined over a broad range of energies, extending up to the range of $t\bar{t}$ production. To measure the uncertainty due to imperfect knowledge of the rate of radiation, we examine the measured top mass in samples where the the simulation parameters are varied by very conservative amounts. Final state radiation can be probed in the same manner, as it is described by the same showering algorithm,

Sample	M_t
Pythia	178.1 ± 0.70 GeV
Pythia, ISR less	178.0 ± 0.74 GeV
Pythia, ISR more	178.5 ± 0.65 GeV
Pythia, FSR less	179.4 ± 0.86 GeV
Pythia, FSR more	178.0 ± 0.62 GeV

The entries in the table labeled *less* and *more* correspond to the simulation parameters with decreased and increased gluon radiation respectively. Therefore, the systematic error due to modeling of radiation is estimated to be $\Delta_{ISR} = 0.24 \pm 0.49$ GeV, and $\Delta_{FSR} = 0.66 \pm 0.53$ GeV.

10.7 Gluon fusion contribution to $t\bar{t}$ production

The matrix element quoted earlier describes the production of $t\bar{t}$ pairs via $q\bar{q}$ annihilation. At the TeVatron, up to 15% of the $t\bar{t}$ pairs may be produced from gg fusion.

Our leading-order generators, Pythia and Herwig, contain only $\approx 5\%$ gg events. To estimate our sensitivity to this fraction, we vary the composition from 0 to 15% in the Herwig sample and determine the effect on the extracted top mass.

gg Fraction	M_t
0%	177.45 ± 0.85 GeV
5%	177.43 ± 0.85 GeV
15%	177.73 ± 1.27 GeV

we take as a systematic error, $\Delta_{gg} = 0.30$ GeV.

10.8 Background statistics

To measure our dependence on the relatively small size of background samples, we split each background sample into twenty pairs of disjoint sets. We measure the mass in the $M_t = 178$ GeV sample for each of the disjoint sets and take the root mean square of the difference between them as an estimate of the error due to having samples of finite size. This is an estimate of the error due to having samples *twice* as small as the samples we use, and so we divide the error by $\sqrt{2}$.

Background	$RMS(\Delta M_t)/\sqrt(2.0)$
Z	0.67 GeV
Fakes	0.95 GeV
WW	0.35 GeV
WZ	0.11 GeV
$Z \rightarrow \tau\tau$	0.22 GeV

We take the sum in quadrature, $\Delta_{BGstat} = 1.24$ GeV.

10.9 Background modeling

The modeling of the two largest backgrounds may be imperfect. We estimate the sensitivity of the method to possible imperfections in these background models.

10.9.1 Drell-Yan

Drell-Yan production is difficult to model well, as it has a large cross-section and a small acceptance. Since there is no real missing energy due to escaping neutrinos, the probability to pass the missing energy requirement is small. One might be concerned whether the modeling of large missing energy on the tail of the distribution is accurate. Figures 10.3-10.5 show the distribution of missing energy in data and in simulation for events with two leptons in the Z window[3]. In each case, the simulation describes the shape of the events seen in data over a range of missing energy. One would be particularly concerned if there were a considerable number of data events on the tails. No such effect is apparent.

Prescription I

To gauge our sensitivity to events on the tails of the $\not\!\!E_T$ distribution, we vary the composition of our pseudo-experiments by both enhancing and suppressing the contribution of events on the tails by giving them different sampling probabilities. We assign a weight to each event as

$$w_+ = 1 + \frac{1}{\sqrt{n_+}}$$

$$w_0 = 1$$

[3]with invariant mass of two leptons, $M_{\ell\ell}$, having a value close to M_Z.

$$w_- = 1 - \frac{1}{\sqrt{n_+}}$$

where n_+ represents the number of events further out on the tail of the missing energy distribution than the given event. The event with the largest missing energy will receive weights ($w_+ = 2, w_0 = 1, w_- = 0$). Thus three samples of pseudo-experiments are constructed, two of which have enhanced or suppressed tails of the missing transverse energy distribution, and the extracted masses are:

Weights	M_t
w_+	177.8 ± 0.4 GeV
w_0	178.1 ± 0.4 GeV
w_-	177.7 ± 0.4 GeV

Prescription II

Another prescription to enhance and suppress events with large missing energy assigns weights to the events proportional to the measured missing energy, and to the inverse of the measured missing energy:

$$w_+ \propto \not{E}_T$$

$$w_0 = 1$$

$$w_- \propto \not{E}_T{}^{-1}$$

The event with the largest missing energy will receive large weights for w_+ and small weights for w_-. This enhances or suppresses the contribution of events on the tail as well. Note that the overall normalization of the weights is arbitrary, as the relative weights are used to form pseudo-experiments. The relative weight between

two events for the w_+ case is the ratio of their measured missing energy; for the w_- case, it is the inverse.

Weights	M_t
w_+	177.8 ± 0.4 GeV
w_0	178.1 ± 0.4 GeV
w_-	177.7 ± 0.4 GeV

The net effect is nearly identical for both prescriptions, and within the statistical error. As demonstrated by the calibration of the response, the mass measurement suppresses a good portion of contribution of Zjj events to the extracted mass. This fact makes the result less sensitive to variations in the background shape.

We take as the error due to the shape of this background $\Delta^Z_{Shape} = 0.4 \pm 0.6$ GeV.

10.9.2 Fake background

The fake background is very difficult to model well in the simulation, as it is sensitive to the smallest details of the detector performance. To avoid issues of modeling, the events which imitate this background are drawn from the data itself. The events are selected with a looser requirement on one of the leptons in order to accumulate a sample of fake candidates, and then weighted by the probability that the loose lepton would pass lepton identification requirements. These weights are calculated as a function of the P_T and isolation of the fake candidate, and each candidate has its own weight (w) and error (Δw).

To gauge our sensitivity to the calculation of the fake rates, we vary the fake rates in two ways. First (a), we enhance those events with large fake probability, to exaggerate their effect; second (b), we enhance events with small fake probability:

Mode	$w > \overline{w}$	$w < \overline{w}$
a	$w \rightarrow w + \Delta w$	$w \rightarrow w - \Delta w$
b	$w \rightarrow w - \Delta w$	$w \rightarrow w + \Delta w$

We study the effect of this weighting on fully realistic[4] pseudo-experiments:

Weights	M_t
w_a	178.2 ± 0.4 GeV
default	178.1 ± 0.4 GeV
w_b	177.6 ± 0.4 GeV

As argued above, the mass measurement is reasonably successful in reducing the effect of these background events, which makes the extracted mass less sensitive to their shapes.

We take the difference as our systematic error, $\Delta^{fakes}_{Shape} = 0.6 \pm 0.6$ GeV, and the total shape error to be Δ^{fakes}_{Shape} and Δ^{Z}_{Shape} added in quadrature:

$$\Delta_{Shape} = 0.7 \pm 0.8 GeV.$$

10.10 Summary

The systematic errors measured in the previous sections are summarized in Table 10.10. Our total systematic uncertainty is 3.37 GeV.

Two significant digits are only kept in order to ease the combination of this top quark measurement with other methods and with measurements in other channels which have both the same sources of systematic uncertainties and the sources unique

[4]proper expected sample composition, all backgrounds included

Source	Size
Jet Energy Scale	2.53 GeV
B-jet energy scale	0.48 GeV
Generator	0.24 ± 0.83 GeV
Response uncertainty	0.4 GeV
Sample composition uncertainty	0.3 GeV
Background MC	1.24 GeV
Background modeling	0.7 ± 0.8 GeV
ISR modeling	0.24 ± 0.49 GeV
FSR modeling	0.66 ± 0.53 GeV
PDFs	0.53 GeV
α_s	0.25 ± 0.83 GeV
Gluon fraction	0.3 GeV
Total	3.37 GeV

Table 10.1: Summary of systematic errors

to each method. Whenever the estimate of a systematic uncertainty is less than the associated uncertainty on that estimate the larger value is quoted.

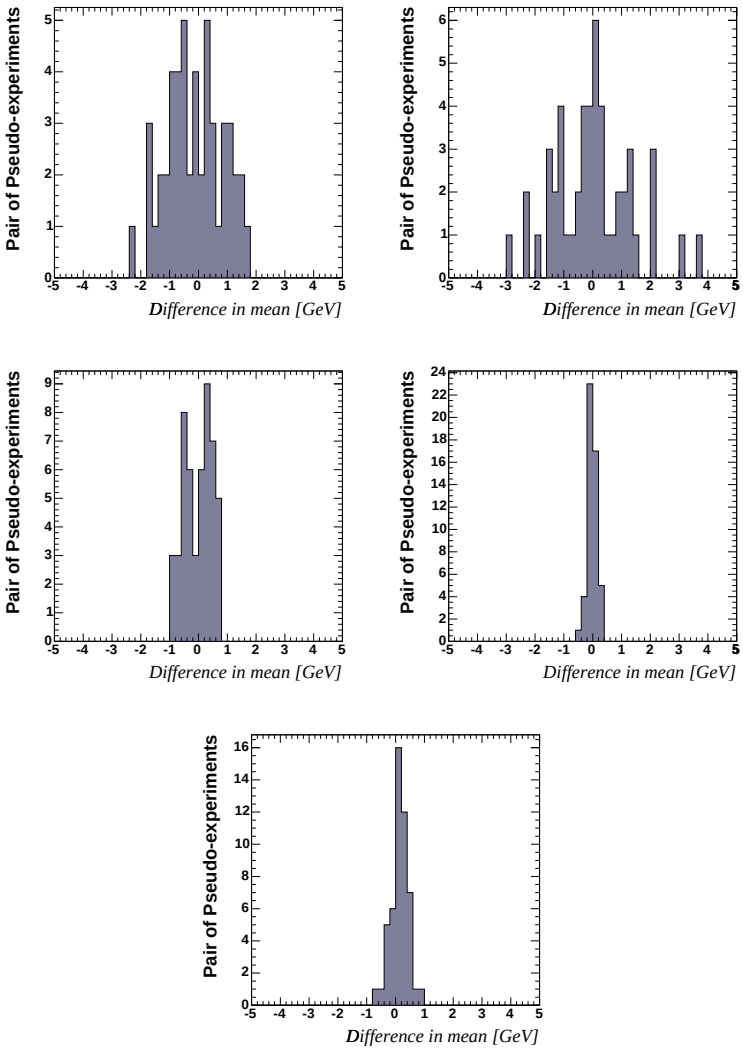

Figure 10.2: Variation in measured mass when background samples are split into disjoint sets. Top left, $Z \to e\bar{e}, \mu\bar{\mu}$; Top right, Fakes. Middle left, WW; Middle right, WZ. Bottom, $Z \to \tau\tau$.

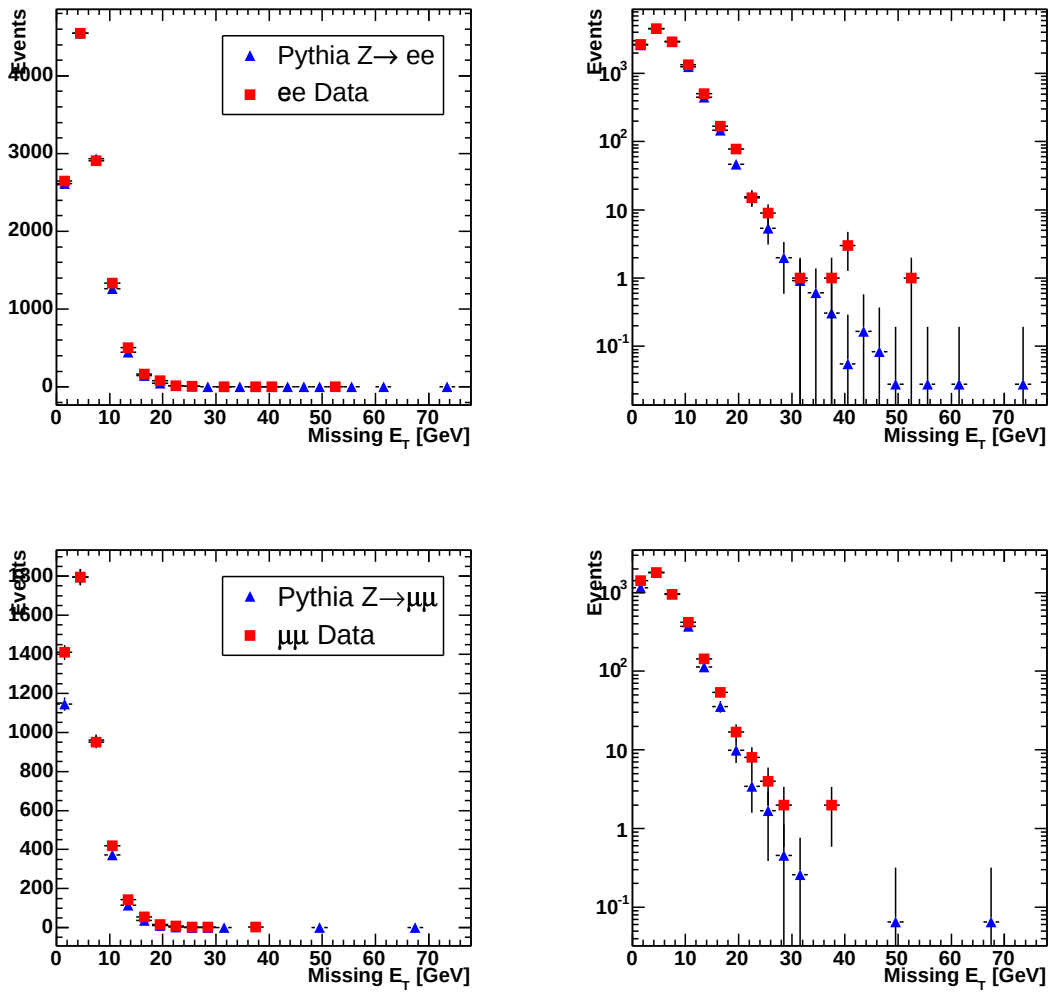

Figure 10.3: Missing transverse energy in Z+0jet events, where the Z decays to electrons (*top*) or muons (*bottom*).

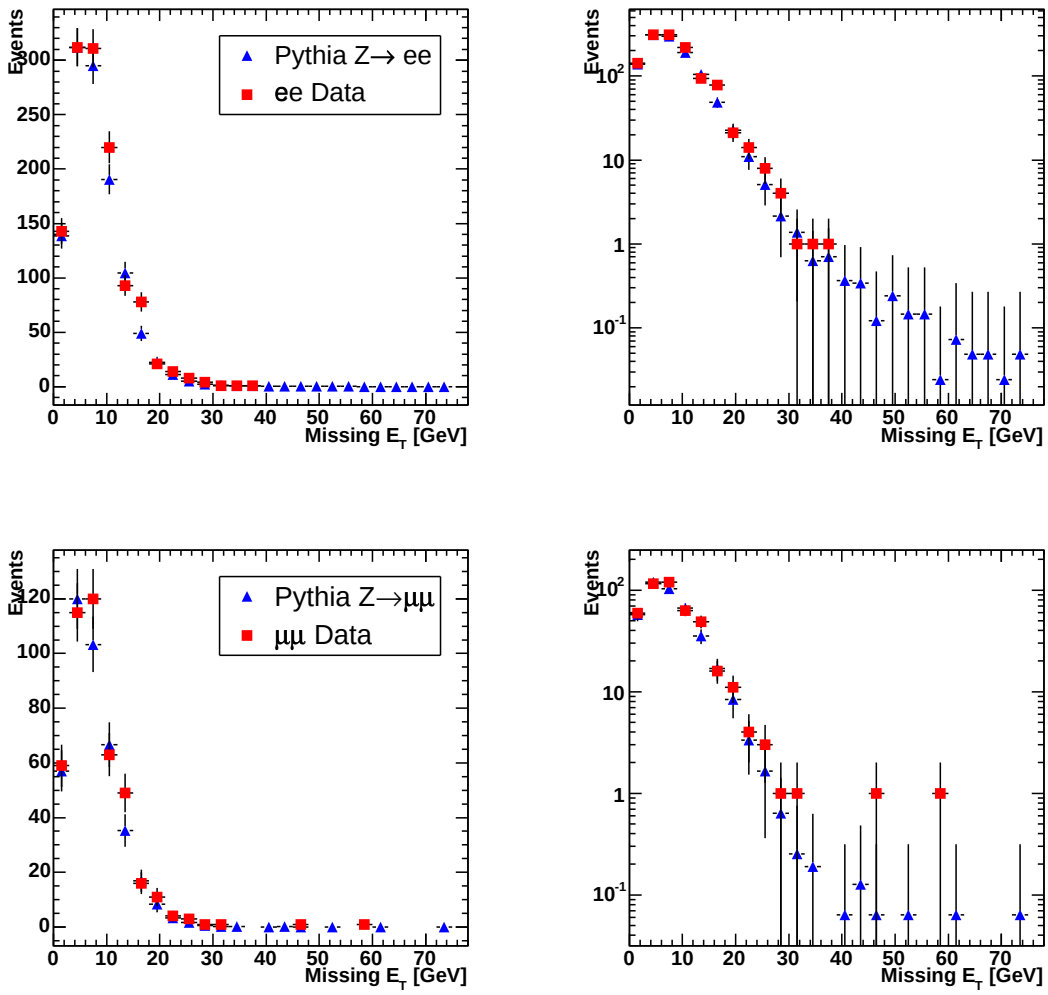

Figure 10.4: Missing transverse energy in Z+1jet events, where the Z decays to electrons (*top*) or muons (*bottom*).

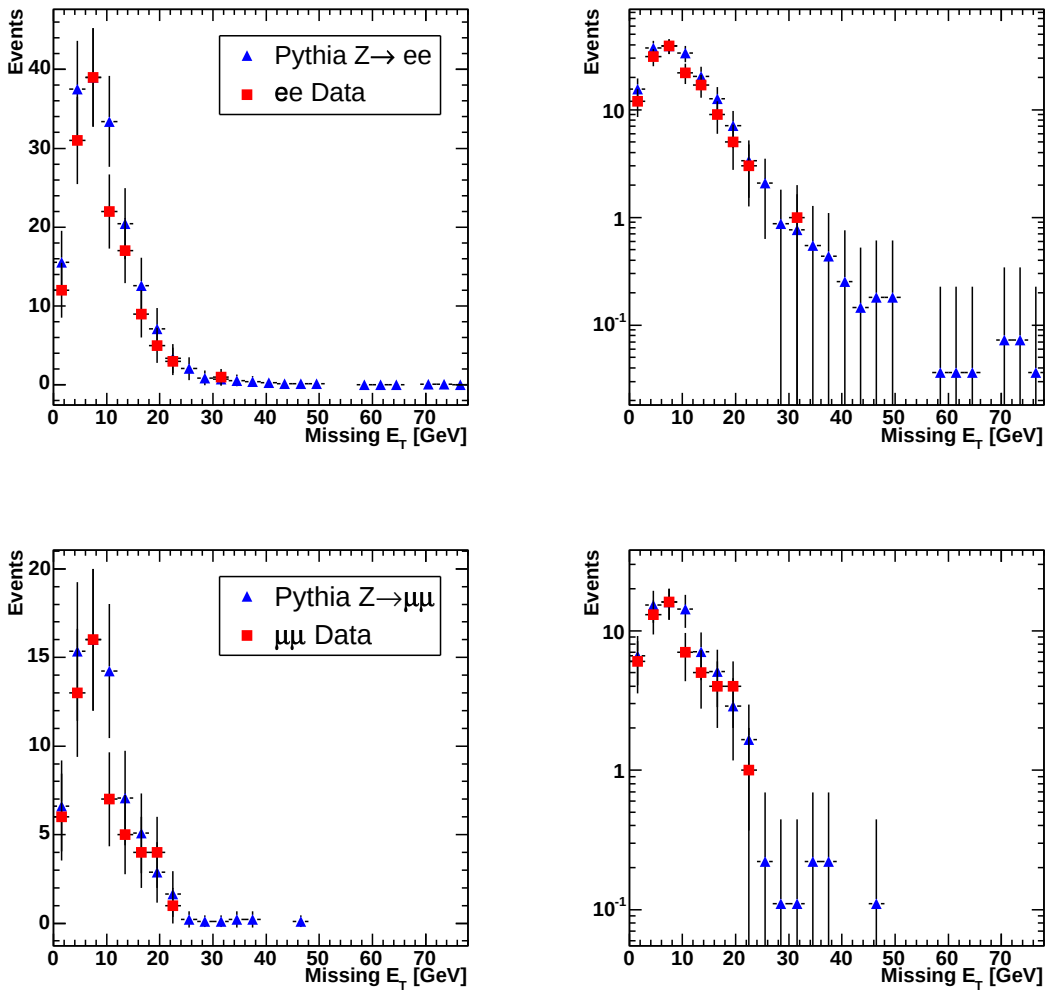

Figure 10.5: Missing transverse energy in Z+2jet events, where the Z decays to electrons (*top*) or muons (*bottom*).

Chapter 11

Data

The collected sample of events in $\int L = 340pb^{-1}$ contains 33 candidate dilepton events. A summary of their kinematic properties can be found in Appendix E, Table E.1.

11.1 Kinematic properties of observed events

We examine the events observed in the data and compare their kinematic properties to that predicted from the simulation; the latter is the sum of signal and background contributions. We note first that the number of observed events is slightly higher than expected, 33 observed to 29 expected. Given the relatively small statistics, this is not an unlikely Poisson fluctuation. Examining the kinematic distributions in Appendix E (see Figures E.1-E.9) does not reveal any dramatic variation in shape for any variable.

In addition, we compare the expected probability distributions of $t\bar{t}$, Zjj, "Fakes" and $WWjj$ probabilities to the observed events, see Figures 11.1-11.4. These quantities are sensitive to all of the kinematic information in the event, and show no significant shape discrepancies. They all appear consistent with a positive Poisson

fluctuation in the number of events.

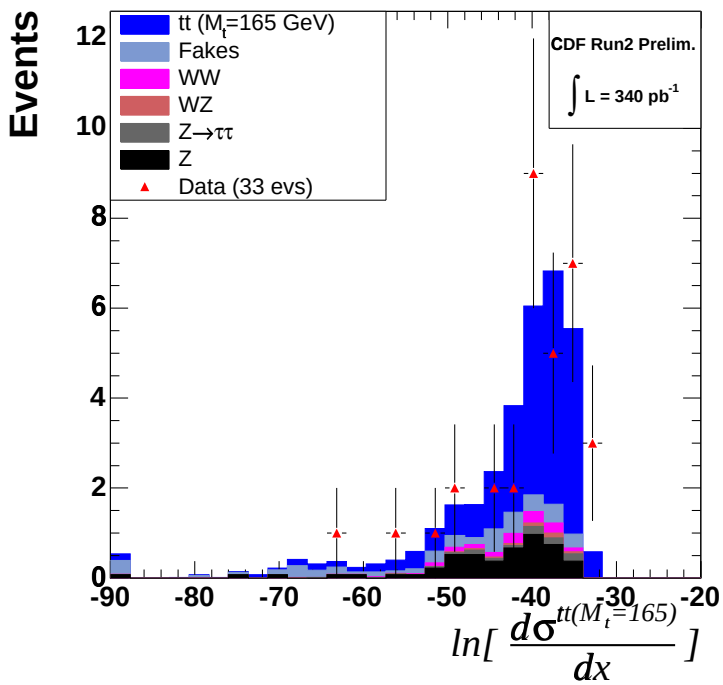

Figure 11.1: Comparison of the $t\bar{t}$ probability distribution for simulated events, scaled by expected contribution to the sample composition, to that for observed events.

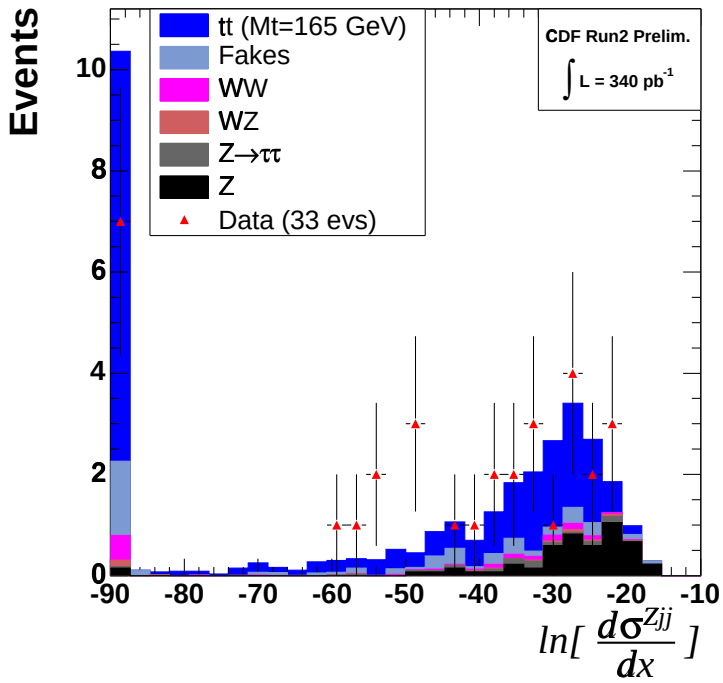

Figure 11.2: Comparison of the Zjj probability distribution for simulated events, scaled by expected contribution to the sample composition, to that for observed events.

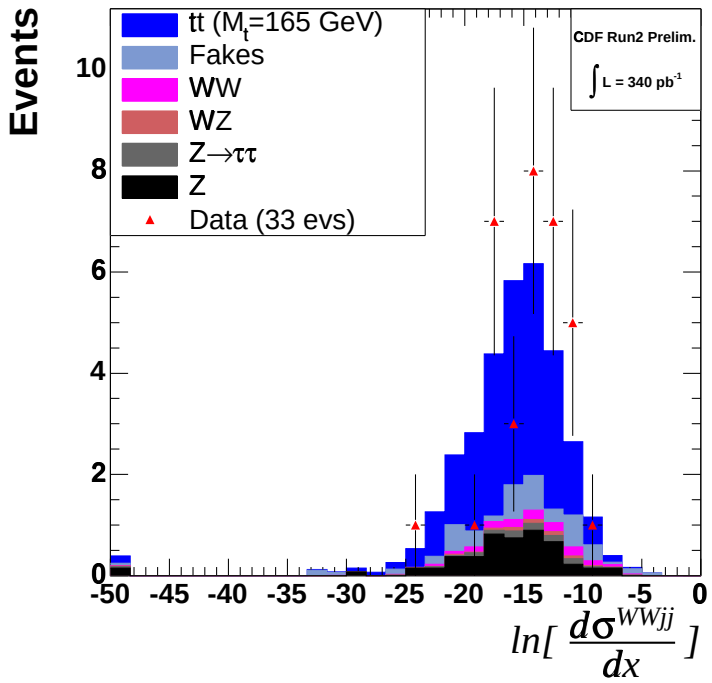

Figure 11.3: Comparison of the $WWjj$ probability distribution for simulated events, scaled by expected contribution to the sample composition, to that for observed events.

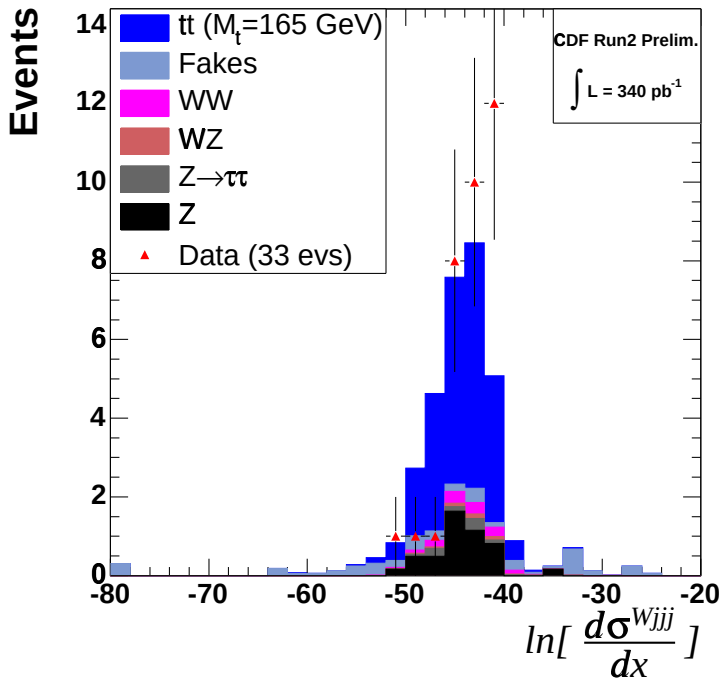

Figure 11.4: Comparison of the "Fakes" probability distribution for simulated events, scaled by expected contribution to the sample composition, to that for observed events.

11.2 Result

The 33 candidate events in the data have individual posterior probabilities as seen in Figure 11.5. From the joint probability we extract the uncorrected, unscaled mass,

$$M_t^{\text{raw}} = 166.42 \pm 3.41^{\text{raw, unscaled}} \text{ GeV}$$

After applying the response correction and the error scaling, the final result is:

$$M_t = 165.17 \pm 6.13 \text{ GeV}$$

The posterior probability curve can be seen in Figures 11.6 and 11.7. The error we measure is not unexpected when one considers the central value; in pseudo-experiments where $M_t = 165$ GeV, 17% of the errors are smaller than this value, see Figure 11.8.

Thus, in $\int L = 340pb^{-1}$ of CDF II data, we measure

$$\boxed{M_t = 165.17 \pm 6.13(\text{stat.}) \pm 3.37(\text{syst.})\text{GeV}}$$

Summary

The method based on the evaluation of the differential cross-section expressed in terms of the observed quantities was for the first time applied to the dilepton $t\bar{t}$ decay channel. The Leading Order matrix element was used in the computation. The measurement of the top quark mass presented in this dissertation, at the time of this writing, is the most precise in the aforementioned channel. Combined with other measurements of the top quark mass, both from different decay channels and

other experiments, this measurement has a non-negligible effect on the world's best estimate of the mass.

Several refinements are considered that will be able to improve the technique described herein. Among the few are: replacing the Leading Order matrix element evaluation with Next-to-Leading Order, re-optimization of the sample selection criteria specifically for mass measurement and various improvements to background modeling.

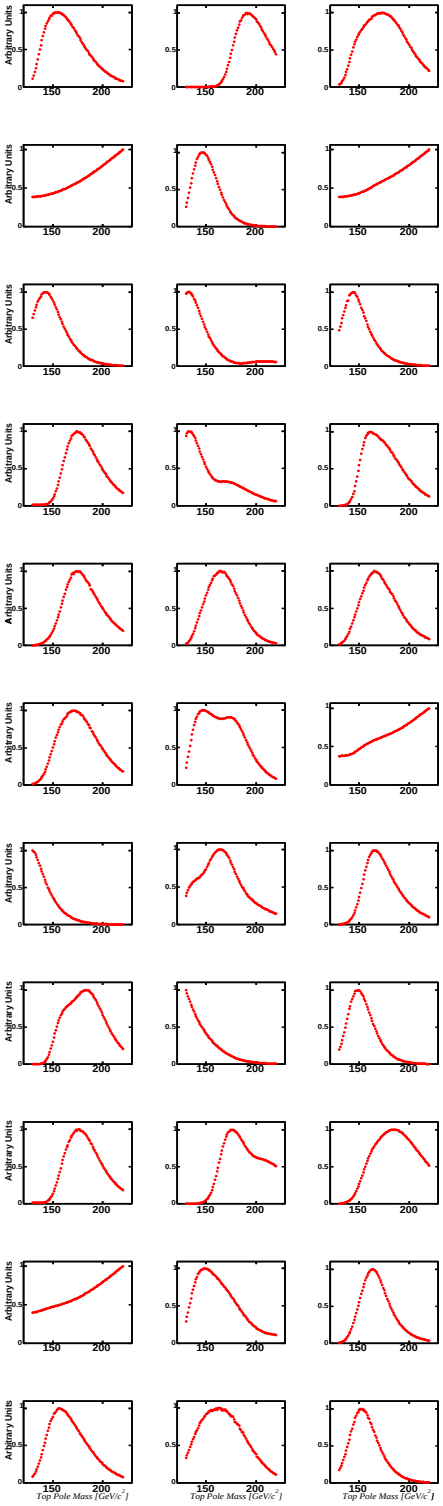

Figure 11.5: Posterior probabilities for each of the 33 candidate events. Each includes the normalized signal and background probabilities.

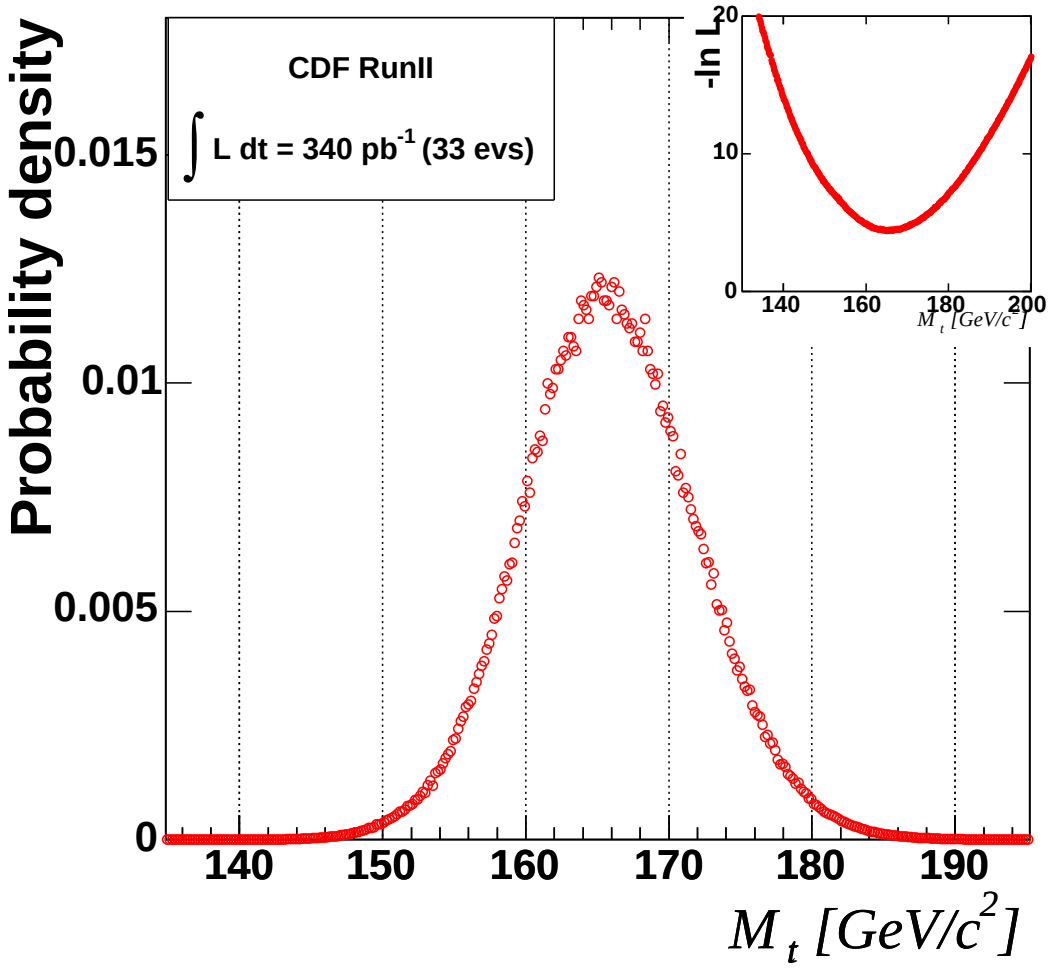

Figure 11.6: Posterior probability density as a function of the top pole mass, for the 33 candidate events, with additional granularity in the evaluation of the probability.

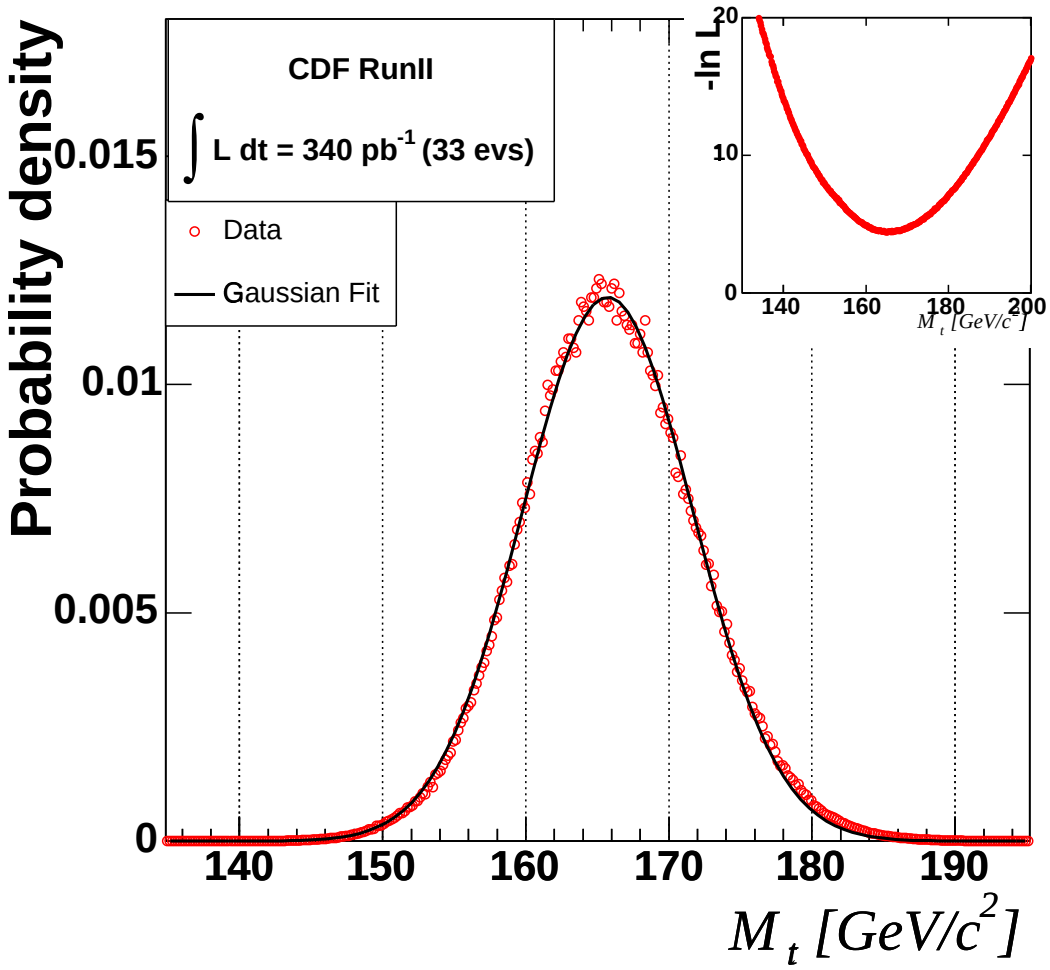

Figure 11.7: Posterior probability density as a function of the top pole mass with a Gaussian fit overlaid, for the 33 candidate events, with additional granularity in the evaluation of the probability.

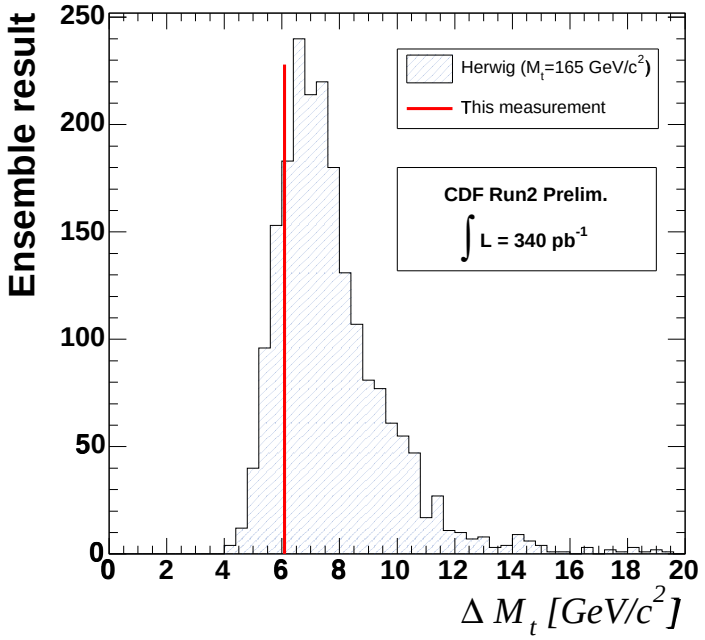

Figure 11.8: Distribution of expected errors for $M_t = 165$ GeV. The measured error is shows as the line; 17% of pseudo-experiments yield a smaller error.

Appendix A

Datasets

The primary datasets used in this analysis are Inclusive Electron Data, Inclusive Muon Data and Plug Data.

A.1 Inclusive electron sample

This dataset consists of events that are accepted via ELECTRON_CENTRAL_18 trigger path:

- Level 1 : CEM tower with $E_T^{\rm em} \geq 8$ GeV and XFT track pointing to it with $P_T \geq 8.34$ GeV and at least 10 hits. If $E_T^{\rm em} \geq 14$ GeV $E^{\rm had}/E^{\rm em} \leq 0.125$ is required.

- Level 2 : cluster $E_T^{\rm em} \geq 16$ GeV and $E^{\rm had}/E^{\rm em} \leq 0.125$ with XFT track of $P_T \geq 8.34$ GeV that matches seed tower

- Level 3 : reconstructed CEM cluster with $E_T \geq 18$ GeV and $E^{\rm had}/E^{\rm em} \leq 0.125$ with COT track of $P_T > 9$ GeV matching it. For data after January 2003, $L_{\rm shr} < 0.4$ and $|\Delta z_{\rm CES}| < 8$ cm are also required.

	for $E_T^{\rm em} < 70$ GeV	$E_T^{\rm em} > 70$ GeV
$E_T^{\rm em}$	> 18 GeV	> 18 GeV
$E^{\rm had}/E^{\rm em}$	< 0.125	
E/P	< 4.0 if $P_T \leq 9$ GeV	$P_T > 15$ GeV
$L_{\rm shr}$	< 0.3	
$\lvert\Delta x\rvert$	< 3.0 cm	< 3.0 cm
$\lvert\Delta z\rvert$	< 5.0 cm	< 5.0 cm

Table A.1: Additional electron cuts.

Further, at least one electron that satisfies relaxed electron cuts, shown in Table A.1, is required.

A.2 Inclusive muon sample

This dataset consists of the events that are accepted via either MUON_CMUP18 or MUON_CMX18. The CMUP path includes the following requirements:

- Level 1: XFT track match with both CMU and CMP hits. Track $P_T \geq 4$ GeV and at least 11 hits per axial super layer required
- Level 2: XFT track with $P_T \geq 8$ GeV
- Level 3: reconstructed COT muon track linked with CMU and CMP stubs. COT track $P_T \geq 18$ GeV, track match in the transverse plane within 10 cm for CMU and 30 cm for CMP.

The CMX trigger path is:

- Level 1: XFT track with $P_T \geq 8$ GeV and CMX hits on one of the two wire pair within the same CMX stack
- Level 2: auto-accepted

P_T	> 18 GeV
E_{em}	$< 3 + \max(0; 0.014 \times (P - 100))$ GeV
E_{had}	$< 9 + \max(0; 0.042 \times (P - 100))$ GeV
$\lvert\Delta x\rvert_{\mathrm{CMU}}$	< 5.0 cm
$\lvert\Delta x\rvert_{\mathrm{CMP}}$	< 10.0 cm
$\lvert\Delta x\rvert_{\mathrm{CMX}}$	< 20.0 cm

Table A.2: Additional muon identification requirements

- Level 3: reconstructed COT muon track with $P_T \geq 18$ GeV with CMX stub. Match withing 30 cm in transverse plane is required

The relaxed identification cuts which are also applied are presented in Table A.2

A.3 Plug data sample

The plug data sample consists of events that pass PEM_MET trigger path:

- Level 1: PEM tower with $E_T^{\mathrm{em}} \geq 8$ GeV and $E^{\mathrm{had}}/E^{\mathrm{em}} < 0.125$ and $\not\!\!E_T > 15$ GeV
- Level 2: PEM cluster with $E_T > 20$ GeV and $E^{\mathrm{had}}/E_{\mathrm{em}} < 0.125$ is required
- Level 3: plug cluster with $E_T^{\mathrm{em}} > 20$ GeV and $E^{\mathrm{had}}/E^{\mathrm{em}} \leq 0.125$, PEM 3×3 fit convergence and $\not\!\!E_T > 20$ GeV

No further selections are applied to the plug sample events.

A.4 Dilepton categories

For the purpose of this analysis a CEM or PHX electron as well as a CMUP or CMX muon are considered well-identified or "tight" if they satisfy all the selection requirements presented in the text. In order to increase the acceptance slightly less well iden-

ee	$\mu\mu$	$e\mu$
CEM-CEM	CMUP-CMUP	CEM-CMUP
CEM-NICEM	CMUP-NICMUP	CEM-NICMUP
PHX-CEM	CMUP-CMU	CEM-CMU
	CMUP-NICMU	CEM-NICMU
	CMUP-CMP	CEM-CMP
	CMUP-NICMP	CEM-NICMP
	CMUP-CMIO	CEM-CMIO
	CMUP-CMX	CEM-CMX
	CMUP-NICMX	CEM-NICMX
	CMX-NICMUP	CMUP-NICEM
	CMX-CMX	CMX-NICEM
	CMX-NICMX	PHX-CMUP
	CMX-CMU	PHX-NICMUP
	CMX-NICMU	PHX-CMU
	CMX-CMP	PHX-NICMU
	CMX-NICMP	PHX-CMP
	CMX-CMIO	PHX-NICMP
		PHX-CMIO
		PHX-CMX
		PHX-NICMX

Table A.3: The dilepton event categories

tified types of leptons are introduced, generally called loose, which are non-isolated central electrons (NICEM), non-isolated CMUP/CMX muons (NICMUP/NICMX), isolated or non-isolated CMU-only or CMP-only muons (CMU/CMP/NICMU/NICMP) and stubless muons (CMIO). A lepton type is denoted non-isolated if only the isolation requirement is removed while all the others are satisfied.

The events selected for this analysis are required to have two leptons with at least one of them to fall into the "tight" category. All the possible event categories that were included in the DIL dataset are shown in Table A.3

Appendix B

Invariant mass

When a process has an intermediate particle, the integration over the phase space of the event can be simplified by splitting the phase space and introducing the integration over invariant mass of the decay products. We start out with:

$$\delta^4(P - \sum_{i=1}^{n} p_i) \prod_{i=1}^{n} \frac{d^3 p_i}{(2\pi)^3 2E_i} \tag{B.1}$$

— the phase space for the process. The following identity is very useful in reducing number of integrations. For final state particles, all m_i are equal to their real masses.

$$\delta(p_i^2 - m_i^2) \frac{d^4 p_i}{(2\pi)^3} = \frac{d^3 p_i}{(2\pi)^3 2E_i} \tag{B.2}$$

We will try to split phase space by introducing intermediate particle with momentum

$$q = \sum_{i=1}^{j} p_i \tag{B.3}$$

The phase space then takes the form:

$$(2\pi)^3\delta^4(P-q-\sum_{i=j+1}^{n}p_i)\prod_{i=1}^{n}\frac{d^3p_i}{(2\pi)^3 2E_i}\,\delta^4(q-\sum_{i=1}^{j}p_i)\,\frac{d^4q}{(2\pi)^3} \tag{B.4}$$

Change from integration over q^0 to integration over M_q^2 is done by introducing

$$\delta(q^2-M_q^2)\,dM_q^2 \tag{B.5}$$

and integrating over q^0 using equation (B.2). The following equation:

$$\delta^4(P-q-\sum_{i=j+1}^{n}p_i)\,\delta^4(q-\sum_{i=1}^{j}p_i)\,\delta(q^2-M_q^2)\,\prod_{i=1}^{n}\frac{d^3p_i}{(2\pi)^3 2E_i}\,\frac{d^4q}{(2\pi)^3}\,(2\pi)^3 dM_q^2 \tag{B.6}$$

becomes:

$$\delta^4(P-q-\sum_{i=j+1}^{n}p_i)\,\delta^4(q-\sum_{i=1}^{j}p_i)\,\prod_{i=1}^{n}\frac{d^3p_i}{(2\pi)^3 2E_i}\,\frac{d^3q}{(2\pi)^3 2E_q}\,(2\pi)^3 dM_q^2 \tag{B.7}$$

or to make it look exactly as in [23]:

$$\left[\delta^4(P-q-\sum_{i=j+1}^{n}p_i)\prod_{i=j+1}^{n}\frac{d^3p_i}{(2\pi)^3 2E_i}\,\frac{d^3q}{(2\pi)^3 2E_q}\right]\left[\delta^4(q-\sum_{i=1}^{j}p_i)\prod_{i=j}^{n}\frac{d^3p_i}{(2\pi)^3 2E_i}\right]\times$$
$$\times(2\pi)^3 dM_q^2 \tag{B.8}$$

The point of the exercise in algebra of Dirac delta-functions and integration was to show that the cited formula from [23] makes sense, and to emphasize the following fact — *additional integration over q three-momentum has to be performed.* Which is natural since introduction of a four-dimensional delta-function results in necessary integrations over three momentum components and invariant mass.

Appendix C

Computation

The computer code that implements the analysis technique outlined in this note relies on numerical computation, namely Monte Carlo integration and finding roots of a polynomial. Monte Carlo integration was done using GNU Scientific Library [34]. Operations on Lorentz vectors were done using CLHEP library [35–37]. Polynomial root finder was implemented using code from [29].

The Monte Carlo integration algorithm VEGAS [38] is used to do the multi-dimensional integrals. Adaptive techniques employed by VEGAS adjust the integration grid using the histogram projections on the axes[1]. When doing Monte Carlo integration with VEGAS one has to be aware of the number of potential pitfalls

- certain choices of integration variables lead to hard to integrate functions.
- grid adjustment rate has to be reduced for "feature-rich" functions.
- integrals of the Breit-Wigner distributions depend on the choice of integration limits.

[1]detailed description of the algorithm is presented in [39]

Searching for solutions of the coupled system of quadratic equations or the equivalent fourth-order polynomial we found the following:

- although the analytic solution of the system can be obtained it was found to perform slower and be less forgiving with respect to roundoff errors.

Appendix D

Analytic neutrino solutions

Analytic solutions to the system of bi-quadratic equations (7.27) were found using Mathematica system.

$$\begin{aligned} p_1x^2 + p_2xy + p_3y^2 + p_4x + p_5y + p_6 &= 0 \\ q_1x^2 + q_2xy + q_3y^2 + q_4x + q_5y + q_6 &= 0 \end{aligned} \tag{D.1}$$

As a first step we find the most generic solution for $y(x)$ with y expressed in terms of x:

$$y = \frac{-(p_6q_3) + p_3q_6 - p_4q_3x + p_3q_4x - p_1q_3x^2}{p_5q_3 - p_3q_5 - p_3q_2x + p_2q_3x} \tag{D.2}$$

For this equation on y to be obtainable the 4-th order equation on x must be satisfied:

$$x^4 + \frac{k_3}{k_4}x^3 + \frac{k_2}{k_4}x^2 + \frac{k_1}{k_4}x + \frac{k_0}{k_4} = 0 \tag{D.3}$$

where:

$$
\begin{aligned}
k_0 &= (p_6^2 q_3^2 + q_6(p_5^2 q_3 - p_3 p_5 q_5 + p_3^2 q_6) + p_6(-(p_5 q_3 q_5) + p_3(q_5^2 - 2q_3 q_6)))/q_3^2 \\
k_1 &= (2p_4 p_6 q_3^2 + p_5^2 q_3 q_4 - 2p_3 p_6 q_3 q_4 + 2p_3 p_6 q_2 q_5 - p_2 p_6 q_3 q_5 + p_3 p_4 q_5^2 + \\
&\quad p_3(-2p_4 q_3 + 2p_3 q_4 - p_2 q_5) q_6 - p_5(p_6 q_2 q_3 + p_4 q_3 q_5 + p_3 q_4 q_5 + p_3 q_2 q_6 - 2p_2 q_3 q_6))/q_3^2 \\
k_2 &= (p_3^2 q_4^2 + q_3(-(p_2 p_6 q_2) + p_4^2 q_3 + 2p_1 p_6 q_3 + 2p_2 p_5 q_4 - \\
&\quad p_1 p_5 q_5 - p_4(p_5 q_2 + p_2 q_5) + p_2^2 q_6) + p_3(p_6 q_2^2 - p_5 q_2 q_4 - 2p_4 q_3 q_4 + 2p_4 q_2 q_5 - p_2 q_4 q_5 + \\
&\quad p_1 q_5^2 - p_2 q_2 q_6 - 2p_1 q_3 q_6))/q_3^2 \\
k_3 &= (p_3(p_4 q_2^2 - p_2 q_2 q_4 - 2p_1 q_3 q_4 + 2p_1 q_2 q_5) + q_3(-(p_1 p_5 q_2) + 2p_1 p_4 q_3 \\
&\quad + p_2^2 q_4 - p_2(p_4 q_2 + p_1 q_5)))/q_3^2 \\
k_4 &= (p_1(p_3 q_2^2 + q_3(-(p_2 q_2) + p_1 q_3)))/q_3^2
\end{aligned}
\tag{D.4}
$$

In terms of $a_0 = \frac{k_0}{k_4}$, $a_1 = \frac{k_1}{k_4}$, $a_2 = \frac{k_2}{k_4}$ and $a_3 = \frac{k_3}{k_4}$ the four solutions to the quartic equation in x are:

$$
x_{1,2,3,4} = \left(-\frac{a_3}{4} \mp \frac{A}{4\sqrt{3}} \mp \frac{\sqrt{\left(-8a_2 + 3a_3^2 - \frac{(2\sqrt[3]{2}B_1)}{\Gamma} - 2^{\frac{2}{3}}\Gamma + \frac{3\sqrt{3}(8a_1 - 4a_2 a_3 + a_3^3)}{A}\right)}}{2\sqrt{6}} \right)
\tag{D.5}
$$

with

$$
\begin{aligned}
\Gamma &= \sqrt[3]{B_2 + \sqrt{-4B_1^3 + B_2^2}} \\
A &= \sqrt{-8a_2 + 3a_3^2 + \frac{4\sqrt[3]{2}B_1}{\Gamma} + 2^{\frac{5}{3}}\Gamma} \\
B_1 &= (12a_0 + a_2^2 - 3a_1a_3) \\
B_2 &= (27a_1^2 - 72a_0a_2 + 2a_2^3 - 9a_1a_2a_3 + 27a_0a_3^2)
\end{aligned}
\tag{D.6}
$$

Appendix E

Kinematic details of data events

A summary of the kinematic properties of data events are presented in Table E.1. Distribution of kinematic variables are shown in Figures E.1-E.9.

		P_T [GeV]		E_T [GeV]		$\not{E}_T$
Run	Event	Lepton 1	Lepton 2	Jet 1	Jet 2	[GeV]
143257	760520	27.29	20.96	43.97	37.65	92.24
150418	960369	89.48	87.01	30.75	26.15	68.66
150431	368759	58.27	36.19	55.16	33.70	44.07
150435	2896171	45.37	42.88	88.61	44.66	64.71
151978	507773	35.89	34.72	47.59	46.48	91.35
153325	599511	37.11	25.23	50.90	34.56	46.47
153374	2276742	72.02	56.87	85.70	55.74	58.14
153447	2643751	87.45	26.30	107.2	21.10	35.52
154654	7344016	59.42	52.86	36.96	20.32	56.66
155114	478702	34.48	28.47	74.07	36.22	89.96
156484	3099305	35.17	34.31	67.29	34.65	75.91
160988	385505	26.05	21.02	87.42	57.05	32.19
161633	963604	40.24	26.49	62.71	36.43	60.52
162820	7050764	33.46	26.24	67.37	52.87	95.84
163012	1438203	119.1	98.54	103.4	74.19	80.55
165198	1827962	34.48	23.82	63.86	32.12	101.4
165364	592961	47.35	21.59	78.78	47.89	127.9
166063	2833132	41.36	38.04	49.80	49.74	64.97
167053	12011678	75.77	50.43	87.26	26.91	28.47
167629	180103	96.57	78.59	78.22	35.74	28.40
167631	2058969	33.97	31.34	38.49	37.88	61.32
168599	2964061	40.76	23.68	36.14	33.55	96.85
177491	3807306	25.94	21.03	67.55	42.98	79.22
178540	2208375	64.42	34.77	97.78	42.85	53.59
178738	10340757	50.05	21.39	76.26	36.51	88.40
178738	1660363	99.99	60.59	43.30	36.68	90.26
183963	1259645	84.72	27.04	142.5	29.64	63.14
184779	892809	51.10	44.26	46.33	20.07	48.86
185037	2287335	85.73	56.09	66.04	60.53	26.92
185377	103906	76.00	20.87	71.08	26.37	80.59
185594	3002817	80.50	26.08	143.8	22.47	199.2
186598	1618142	69.41	35.75	71.00	70.15	66.96
186598	4194951	54.50	36.05	90.70	58.81	42.65

Table E.1: Run and event numbers and selected kinematic quantities for candidate dilepton events.

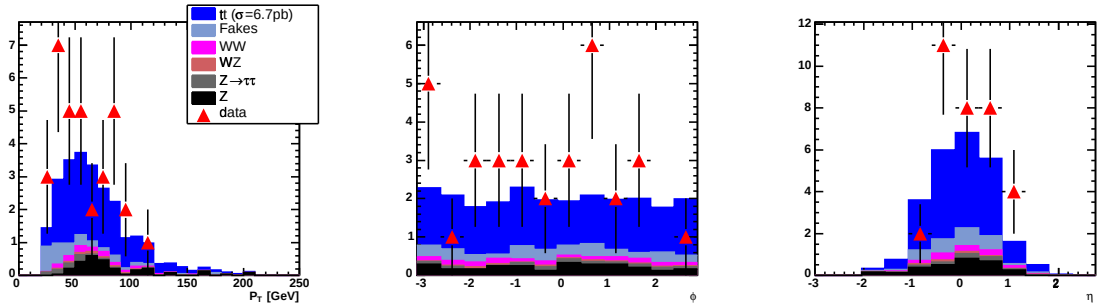

Figure E.1: Transverse momentum (P_T), azimuthal angle (ϕ) and pseudo-rapidity (η) of the leading jet.

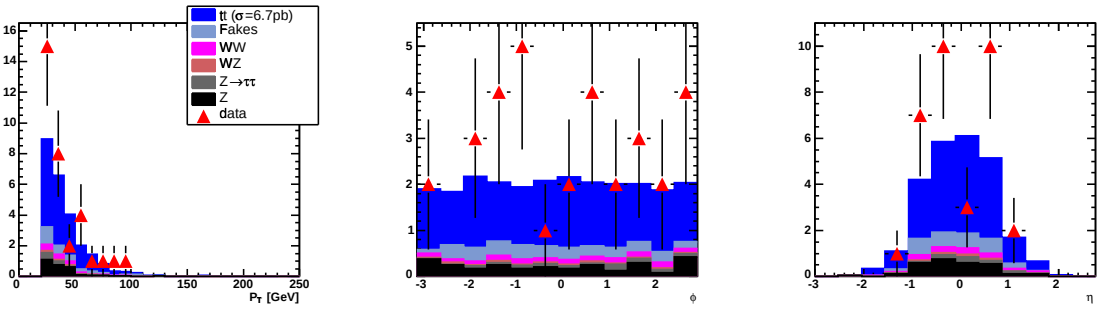

Figure E.2: Transverse momentum (P_T), azimuthal angle (ϕ) and pseudo-rapidity (η) of the second jet.

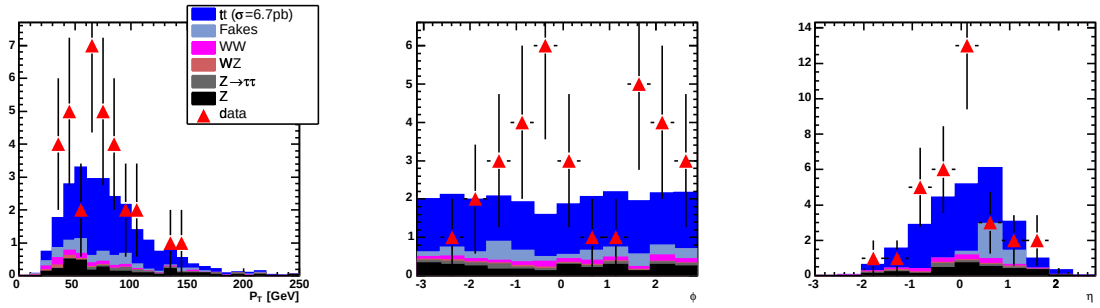

Figure E.3: Transverse momentum (P_T), azimuthal angle (ϕ) and pseudo-rapidity (η) of the leading lepton.

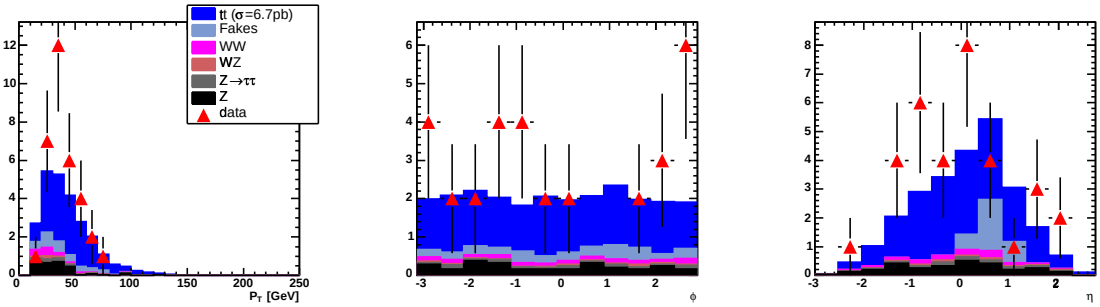

Figure E.4: Transverse momentum (P_T), azimuthal angle (ϕ) and pseudo-rapidity (η) of the second lepton.

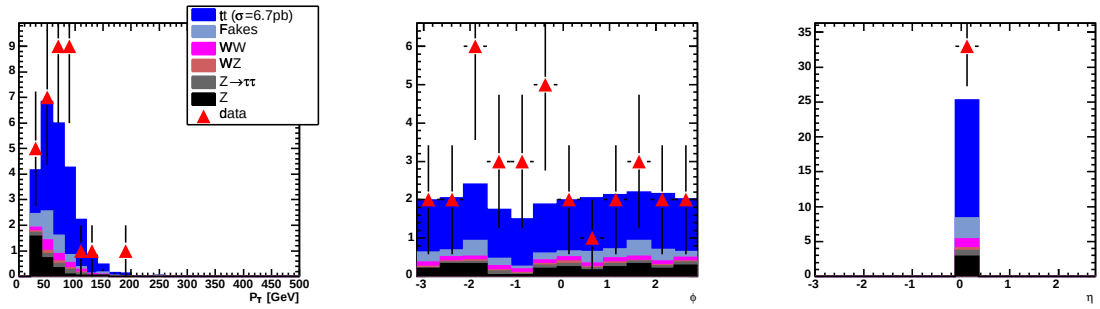

Figure E.5: Transverse momentum (P_T), azimuthal angle (ϕ) and pseudo-rapidity (η) of the missing transverse energy.

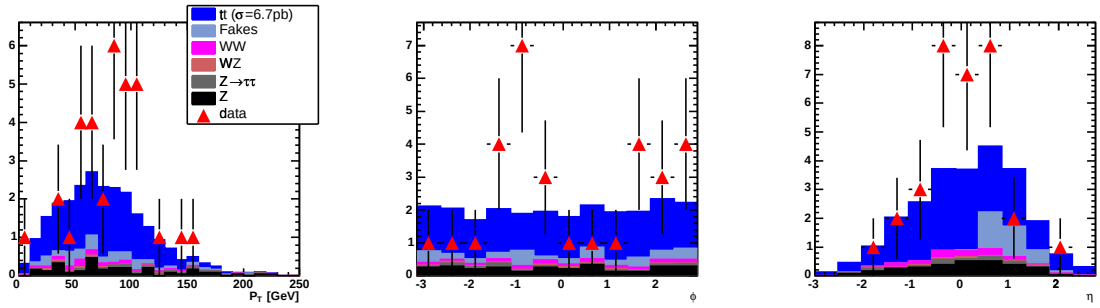

Figure E.6: Transverse momentum (P_T), azimuthal angle (ϕ) and pseudo-rapidity (η) of the vector sum of the leptons.

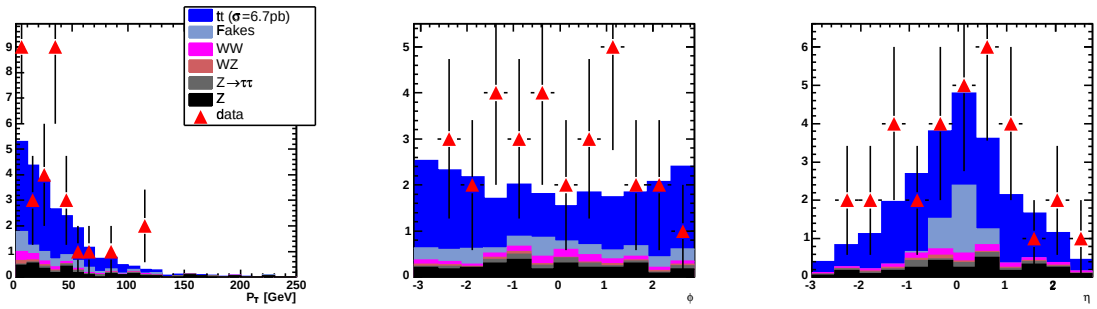

Figure E.7: Difference in transverse momentum (P_T), azimuthal angle (ϕ) and pseudo-rapidity (η) of the two leptons.

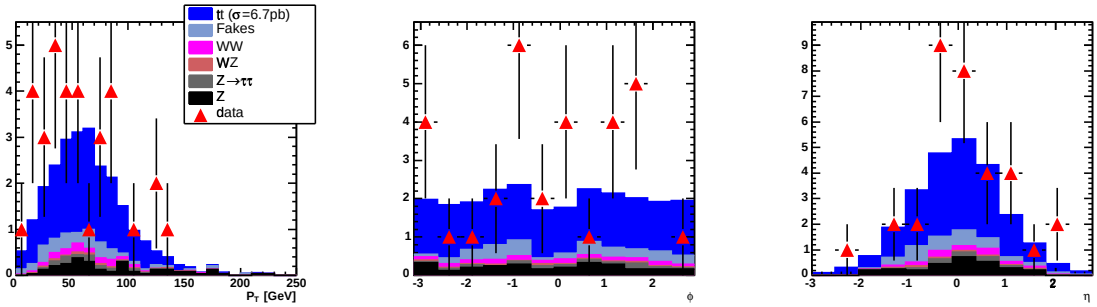

Figure E.8: Transverse momentum (P_T), azimuthal angle (ϕ) and pseudo-rapidity (η) of the vector sum of the jets.

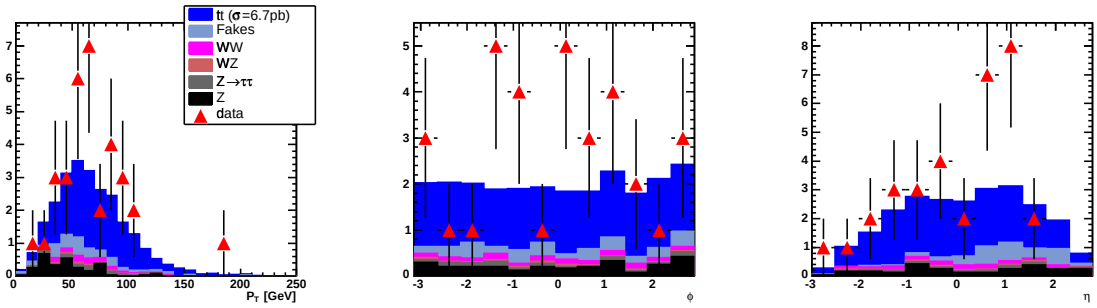

Figure E.9: Transverse momentum (P_T), azimuthal angle (ϕ) and pseudo-rapidity (η) of the vector sum of both jets and leptons.

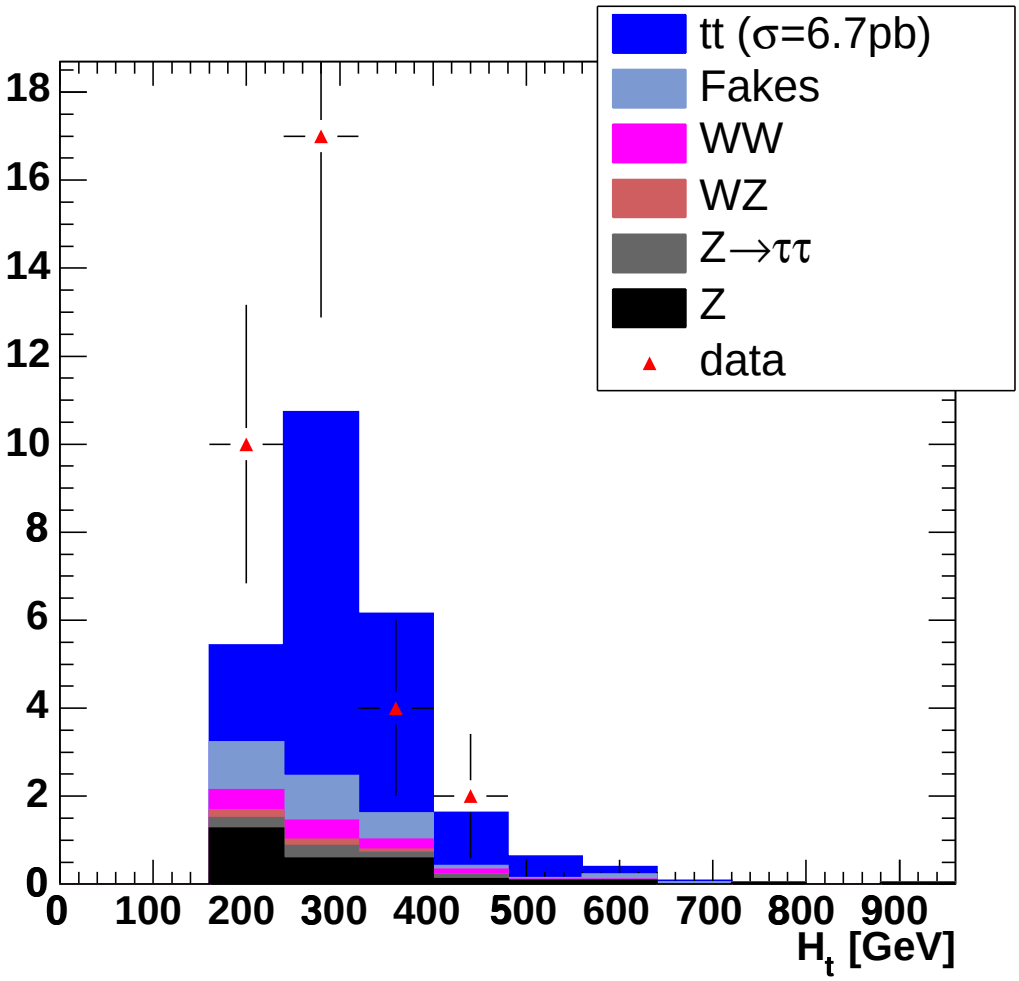

Figure E.10: Distribution of H_T.

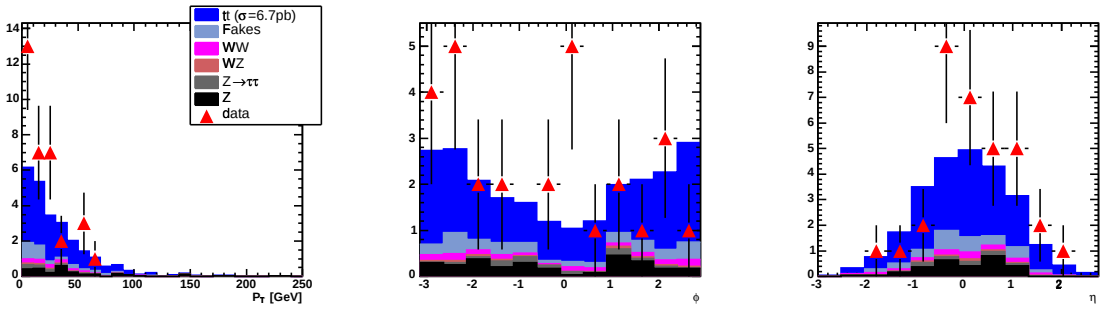

Figure E.11: Transverse momentum (P_T), azimuthal angle (ϕ) and pseudo-rapidity (η) of the difference between the leading jets.

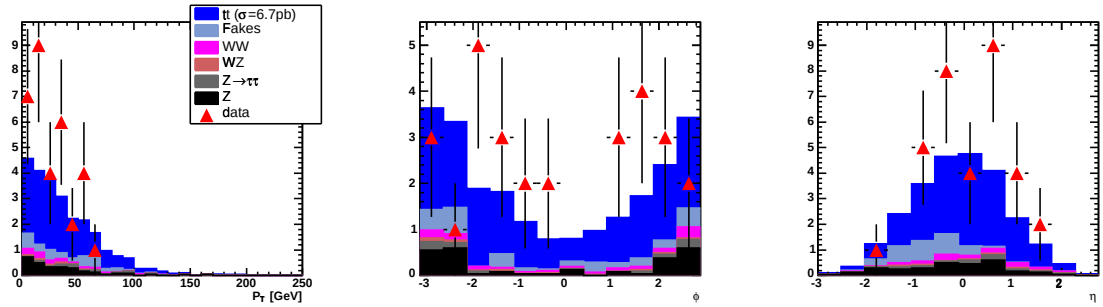

Figure E.12: Transverse momentum (P_T), azimuthal angle (ϕ) and pseudo-rapidity (η) of the difference between the leading lepton and the leading jet.

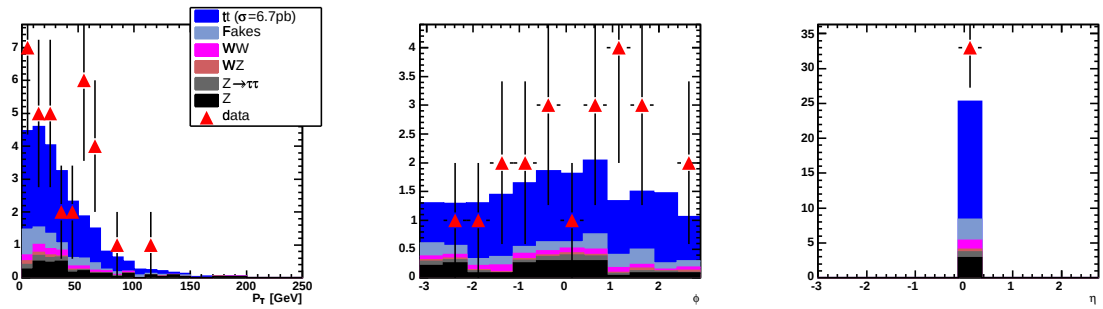

Figure E.13: Transverse momentum (P_T), azimuthal angle (ϕ) and pseudo-rapidity (η) of the difference between the missing energy and the leading jet.

Bibliography

[1] F. Abe *et al.* (CDF), Phys. Rev. Lett. **74**, 2626 (1995), hep-ex/9503002.

[2] S. Abachi *et al.* (D0), Phys. Rev. Lett. **74**, 2632 (1995), hep-ex/9503003.

[3] P. C. Bhat, H. Prosper, and S. S. Snyder, Int. J. Mod. Phys. **A13**, 5113 (1998), hep-ex/9809011.

[4] P. Langacker (1995), hep-ph/0304186.

[5] M. Beneke *et al.* (2000), hep-ph/0003033.

[6] S. Willenbrock (1996), hep-ph/9608418.

[7] D. Chakraborty, J. Konigsberg, and D. L. Rainwater, Ann. Rev. Nucl. Part. Sci. **53**, 301 (2003), hep-ph/0303092.

[8] E. H. Simmons (1999), hep-ph/9908488.

[9] E. H. Simmons (2000), hep-ph/0011244.

[10] N. Kidonakis and R. Vogt, Int. J. Mod. Phys. **A20**, 3171 (2005), hep-ph/0410367.

[11] T. Affolder *et al.* (CDF), Phys. Rev. **D63**, 032003 (2001), hep-ex/0006028.

[12] F. Abe *et al.* (CDF), Phys. Rev. Lett. **82**, 271 (1999), hep-ex/9810029.

[13] F. Abe *et al.* (CDF), Phys. Rev. Lett. **80**, 2767 (1998), `hep-ex/9801014`.

[14] B. Abbott *et al.* (D0), Phys. Rev. **D60**, 052001 (1999), `hep-ex/9808029`.

[15] B. Abbott *et al.* (D0), Phys. Rev. **D58**, 052001 (1998), `hep-ex/9801025`.

[16] V. M. Abazov *et al.* (D0), Nature **429**, 638 (2004), `hep-ex/0406031`.

[17] D. Acosta *et al.* (CDF), Phys. Rev. Lett. **93**, 142001 (2004), `hep-ex/0404036`.

[18] M. Tecchio *et al.*, *Top Dilepton Cross Section Measurement using the GEN5 DIL Selection*, CDF Internal Note CDF/DOC/TOP/CDFR/7851 (2005).

[19] M. F. Canelli UMI-31-14921.

[20] J. C. Estrada Vigil FERMILAB-THESIS-2001-07.

[21] G. Mahlon and S. J. Parke, Phys. Rev. **D53**, 4886 (1996), `hep-ph/9512264`.

[22] G. Mahlon and S. J. Parke, Phys. Lett. **B411**, 173 (1997), `hep-ph/9706304`.

[23] S. Eidelman *et al.* (Particle Data Group), Phys. Lett. **B592**, 1 (2004).

[24] D. Whiteson, *Muon Momentum Resolution in 5.3.1 Data and Simulation*, CDF Internal Note CDF/DOC/MUON/CDFR/7254 (2004).

[25] M. L. Mangano, M. Moretti, F. Piccinini, R. Pittau, and A. D. Polosa, JHEP **07**, 001 (2003), `hep-ph/0206293`.

[26] F. Caravaglios and M. Moretti, Phys. Lett. **B358**, 332 (1995), `hep-ph/9507237`.

[27] M. L. Mangano, M. Moretti, and R. Pittau, Nucl. Phys. **B632**, 343 (2002), `hep-ph/0108069`.

[28] F. Caravaglios, M. L. Mangano, M. Moretti, and R. Pittau, Nucl. Phys. **B539**, 215 (1999), `hep-ph/9807570`.

[29] A. Glassner, ed., *Graphics gems* (Academic Press Professional, Inc., San Diego, CA, USA, 1990).

[30] J.-F. Arguin and P. K. Sinervo, *b-jets Energy Scale Uncertainty From Existing Experimental Constraints*, CDF Internal Note CDF/ANAL/TOP/CDFR/7252 (2004).

[31] O. Gonzalez and C. Rott, *Uncertainties due to the PDFs for the gluino-sbottom search*, CDF Internal Note CDF/PHYS/EXOTIC/CDFR/7051 (2004).

[32] J. Pumplin *et al.*, JHEP **07**, 012 (2002), `hep-ph/0201195`.

[33] Y.-K. Kim and U.-K. Yang, *Initial state gluon radiation studies on Drell-Yan data for top-pair production in hadron collider*, CDF Internal Note CDF/PHYS/TOP/CDFR/6804 (2004).

[34] M. Galassi *et al.*, *GNU Scientific Library Reference Manual - Revised Second Edition* (Network Theory Ltd., 2003).

[35] L. Lonnblad, Comput. Phys. Commun. **84**, 307 (1994).

[36] M. S. Fischler and A. Pfeiffer To be published in the proceedings of International Conference on Computing in High Energy Physics and Nuclear Physics (CHEP 2000), Padova, Italy, 7-11 Feb 2000.

[37] L. Garren Prepared for Computing in High-Energy Physics (CHEP '04), Interlaken, Switzerland, 27 Sep - 1 Oct 2004.

[38] G. P. Lepage CLNS-80/447.

[39] G. P. Lepage, J. Comput. Phys. **27**, 192 (1978).